Inclusive production of hadrons in neutral and charged current deep inelastic scattering

Dissertation
zur Erlangung des Doktorgrades
des Departament Physik
der Universität Hamburg

vorgelegt von

Carlos Sandoval
aus Bogotá, Kolumbien

Hamburg
2009

Erstgutachter der Dissertation:	Prof. Dr. B. A. Kniehl
Zweitgutachter der Dissertation:	Prof. Dr. J. Bartels

Erstgutachter der Disputation:	Prof. Dr. B. A. Kniehl
Zweitgutachter der Disputation:	Prof. Dr. G. Kramer

Datum der Disputation	6. November 2009

Vorsitzender des Prüfungsausschusses:	Prof. Dr. G. Sigl
Vorsitzender des Promotionsausschusses:	Prof. Dr. R. Klanner
Dekan der MIN-Fakultät	Prof. Dr. H. Graener

Abstract

We have calculated the inclusive single production of hadrons in neutral and charged current deep-inelastic scattering at next-to-leading order using perturbative QCD to first and second order in α_s. Virtual and real corrections were calculated, and a Monte Carlo program was implemented to obtain cross sections at NLO in the $\overline{\mathrm{MS}}$ scheme using the dipole subtraction method. Our results to first order in α_s were compared to charged hadron production data from the H1 and ZEUS collaborations. A comparison was also made to second order in α_s with π^0 and $D^{*\pm}$ production data from the H1 collaboration. We have also studied the effect of the Z boson contribution in these processes and calculated the cross sections for charged-current single hadron production in deep inelastic scattering.

Zusammenfassung

Die inklusive Einfachproduktion von Hadronen in Tiefinelastischer Streuung bei Austausch neutraler und geladener Bosonen wurde zur nächstführenden Ordnung mittels perturbativer QCD in erster und zweiter Ordnung in α_s berechnet. Es wurden virtuelle und reelle Korrekturen bestimmt und ein Monte Carlo-Programm implementiert, um Wirkungsquerschnitte zu nächstführender Ordnung im $\overline{\mathrm{MS}}$-Schema mit der Dipolsubtraktionsmethode zu erhalten. Die Resultate wurden verglichen mit Messungen der H1 und ZEUS Kollaborationen von der Produktion von geladenen Hadronen im Fall der Berechnungen zur ersten Ordnung in α_s, sowie mit π^0- und $D^{*\pm}$-Produktionsmessungen der H1 Kollaboration für die Berechnungen zur zweiten Ordnung in α_s. Dazu wurden Effekte des Z-Boson-Beitrags in diesen Prozessen studiert und für den Austausch geladener Bosonen der Wirkungsquerschnitt für Einfachproduktion von Hadronen in Tiefinelastischer Streuung berechnet.

Contents

List of Figures

List of Tables

Chapter 1

Introduction

The standard model of elementary particles [1, 2] provides the most accurate description of the interactions that occur between particles and it is the best tested theory we currently have. The model consists of two main parts: the spontaneously broken $SU(2) \times U(1)$ electroweak sector and the unbroken $SU(3)$ colour gauge sector, which is known as Quantum Chromodynamics (QCD). Although the standard model has some problems, and there are still missing pieces such as the Higgs boson, which has not yet been found experimentally, QCD has been extremely succesfull in describing strong interactions.

One of its major achievements is the description of *asymptotic freedom* [3, 4] and *confinement*. We know that all particles which are subject to the strong force, *hadrons*, consist at an elementary level of quarks and gluons. The gluons are the propagators of the strong interaction, with no charge but having colour. However, quarks have never been found in isolation. Any effort to produce single quarks in scattering experiments leads only to the production of mesons and baryons [5]. On the other hand, the *parton model* [6, 7], describes successfully certain high energy cross sections. Asymptotic freedom refers to the weakness of the short-distance interaction, while the confinement of quarks follows from its strength at long distances. The former is a perturbative prediction but the latter is not. This makes QCD a theory with no single approximation method applicable to all length scales. However, the justification for the use of perturbative QCD lies largely with experiment. Over time, it has become clear that perturbative QCD describes a large set of high energy, large momentum-transfer cross sections. It is in this area that its formalism has been developed, and in which it has proved an invaluable tool in the study of the strong interaction.

1.1 The electroweak standard model

This sector of the model is constructed by choosing the gauge group $SU(2)_L \otimes U(1)_Y$, and introducing a gauge boson for each generator of the group:

$$\begin{aligned} SU(2)_L &\longrightarrow W^1_\mu, W^2_\mu, W^3_\mu, \\ U(1)_Y &\longrightarrow B_\mu. \end{aligned} \tag{1.1}$$

This allows us to write the free Lagrangian for the gauge fields as

$$\mathcal{L}_{gauge} = -\frac{1}{4} W^i_{\mu\nu} W^{i\mu\nu} - \frac{1}{4} B_{\mu\nu} B^{\mu\nu}, \tag{1.2}$$

where

$$W^i_{\mu\nu} = \partial_\nu W^i_\mu - \partial_\mu W^i_\nu + g\epsilon_{ijk} W^j_\mu W^k_\nu, \tag{1.3}$$

$$B_{\mu\nu} = \partial_\nu B_\mu - \partial_\mu B_\nu. \tag{1.4}$$

To introduce fermions in the model, we write first the free massless Lagrangian. For leptons we have

$$\begin{aligned} \mathcal{L}_l &= \bar{R} i \not{\partial} R + \bar{L} i \not{\partial} L \\ &= \bar{l} i \not{\partial} l + \bar{\nu} i \not{\partial} \nu, \end{aligned} \tag{1.5}$$

and for quarks

$$\mathcal{L}_q = \bar{L}_U i \not{\partial} L_U + \bar{L}_C i \not{\partial} L_C + \bar{R}_U i \not{\partial} R_U + \bar{R}_D i \not{\partial} R_D + \bar{R}_C i \not{\partial} R_C + \bar{R}_S i \not{\partial} R_S, \tag{1.6}$$

where L denotes left doublets and R right singlets. If we want the theory to be locally invariant, we must introduce a covariant derivative:

$$\begin{aligned} \mathcal{D}_L &: \partial_\mu + ig\tau^i W^i_\mu + i\frac{g'}{2} Y B_\mu, \\ \mathcal{D}_R &: \partial_\mu + i\frac{g'}{2} Y B_\mu, \end{aligned} \tag{1.7}$$

that will lead to the interactions between the gauge fields and the fermions. We see that using this, the Lagrangians for leptons and quarks can be written as

$$\mathcal{L}^\pm_l = -\frac{g}{2\sqrt{2}} (\bar{\nu}\gamma_\mu(1-\gamma_5) l W^+_\mu + \bar{l}\gamma_\mu(1-\gamma_5)\nu W^-_\mu), \tag{1.8}$$

$$\mathcal{L}^0_l = -g \sin\theta_W (\bar{l}\gamma_\mu l) A_\mu - \frac{g}{2\cos\theta_W} \sum_{i=l,\nu} \bar{\Psi}_i \gamma_\mu (g^i_V - g^i_A \gamma_5) \Psi_i Z_\mu, \tag{1.9}$$

$$\mathcal{L}^\pm_q = -\frac{g}{2\sqrt{2}} (\bar{u}\gamma_\mu(1-\gamma_5) d' + \bar{c}\gamma_\mu(1-\gamma_5) s') W^+_\mu + h.c, \tag{1.10}$$

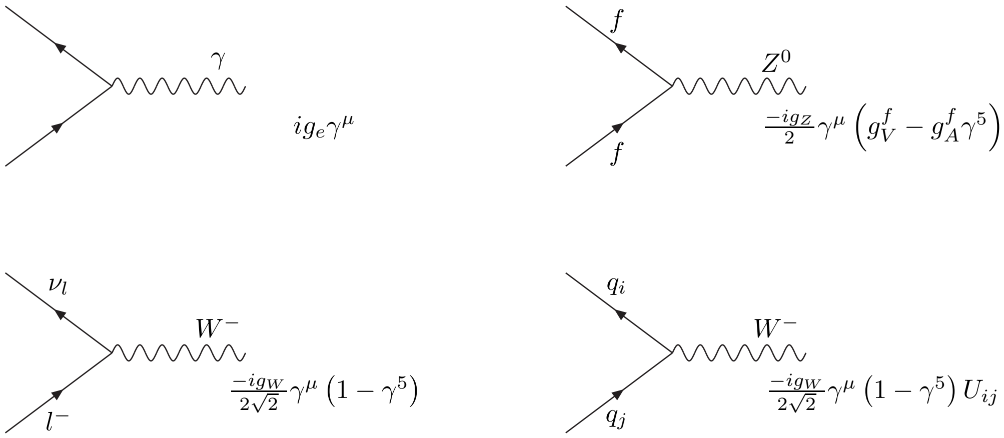

Figure 1.1: Feynman rules for the electroweak sector of the Standard Model.

$$\begin{aligned}\mathcal{L}_q^0 &= g\sin\theta_W\left(-\frac{2}{3}\sum_{\Psi_q=u,c}\bar{\Psi}_q\gamma_\mu\Psi_q+\frac{1}{3}\sum_{\Psi_q=d',s'}\bar{\Psi}_q\gamma_\mu\Psi_q\right)A_\mu \\ &- \frac{g}{2\cos\theta_W}\left(\sum_{\Psi_q=u,\ldots,c}\bar{\Psi}_q\gamma_\mu(g_V^q-g_A^q\gamma_5)\Psi_q\right)Z_\mu, \qquad (1.11)\end{aligned}$$

where we have separated them into charged and neutral components. Here we see the vector nature of the QED couplings and the vector-axial nature of the weak currents. From this Lagrangian we can obtain the feynman rules for the electroweak sector of the standard model as shown in figure 1.1, where we have the coupling constants:

$$g_e = \sqrt{4\pi\alpha}, \qquad (1.12)$$

$$g_W = \frac{g_e}{\sin\theta_W}, \qquad (1.13)$$

$$g_Z = \frac{g_e}{\sin\theta_W\cos\theta_W}, \qquad (1.14)$$

$$g_V^f = T_f^3 - 2e_f\sin^2\theta_W, \qquad (1.15)$$

$$g_A^f = T_f^3, \qquad (1.16)$$

with $T^3_{\nu,u}=\frac{1}{2}$, $T^3_{e,d}=-\frac{1}{2}$. On the other hand, the propagators for fermions and bosons are

$$\text{Spin }\frac{1}{2} \quad : \quad \frac{i(\not{q}+m)}{q^2-m^2}, \qquad (1.17)$$

$$\text{Spin 1} \quad : \quad \frac{-i(g_{\mu\nu}-q_\mu q_\nu/m^2)}{q^2-m^2}. \qquad (1.18)$$

At this point in the model it is not possible to introduce a term with the masses of the particles, since such a term would break the gauge symmetry. It is for this reason that the standard model resorts to the mechanism of spontaneous symmetry breaking to give mass to the particles, introducing a new particle in the model: the Higgs boson. We will not go into the details of that, since it is not necessary for the purposes of this work, and will now concentrate on the structure of QCD.

1.2 Quantum Chromodynamics

The Lagrangian of QCD can be written as [8, 9]

$$\mathcal{L}_{\text{eff}}^{QCD} = \mathcal{L}_{\text{invariant}} + \mathcal{L}_{\text{gauge}} + \mathcal{L}_{\text{ghost}}, \tag{1.19}$$

which is a function of the fermion fields, gluon fields and the ghosts fields. The invariant Lagrangian is the classical density, invariant under local $SU(N_c)$ gauge transformations, with $N_c = 3$ for QCD. It is of the form that was originally written down by Yang and Mills [10],

$$\begin{aligned} \mathcal{L}_{\text{invariant}} &= \sum_f \bar{\Psi}_f \left(i \not{\mathcal{D}}[A] - m_f\right) \Psi_f - \frac{1}{4} F^2[A] \\ &= \sum_{f=1}^{n_f} \sum_{\alpha,\beta=1}^{4} \sum_{i,j=1}^{N_c} \bar{\Psi}_{f,\beta,j} \left(i\gamma^\mu_{\alpha\beta} \mathcal{D}_{mu,ij}[A] - m_f \delta_{\beta\alpha}\delta_{ij}\right) \Psi_{f,\alpha,i} \\ &\quad -\frac{1}{4} \sum_{\mu,\nu=0}^{3} \sum_{a=1}^{N_c^2-1} F_{\mu\nu,a}[A] F_a^{\mu\nu}[A], \end{aligned} \tag{1.20}$$

where

$$\mathcal{D}_{\mu,ij}[A] = \partial_\mu \delta_{ij} + igA_{\mu a} \left(T_a^{(F)}\right)_{ij}, \tag{1.21}$$

is the covariant derivative in the N_c-dimensional representation of $SU(N_c)$, which acts on the spinor quark fields with colour indices $i = 1, ..., N_c$. There are n_f independent quark fields ($n_f = 6$ in the standard model), labelled by flavour $f = u, d, c, s, t, b$. In the QCD Lagrangian they are only distinguished by their masses. We also have

$$F_{\mu\nu,a}[A] = \partial_\mu A_{\nu a} - \partial_\nu A_{\mu a} - g_s C_{abc} A_{\mu b} A_{\nu c}, \tag{1.22}$$

which is the non-abelian field strength defined in terms of the gluon vector field A_b^μ, with $N_c^2 - 1$ group components b. The QCD (strong) coupling is given by g_s and the C_{abc} with $a, b, c = 1...N_c^2 - 1$ are real numbers called the structure constants of $SU(N_c)$, which define its Lie algebra. As mentioned before, for QCD [11, 12], $N_c = 3$. The Lie algebra is determined by the commutation relations of the $N_c^2 - 1$, $N_c \times N_c$ matrices $\left(T_a^{(F)}\right)_{ij}$ that appear in the definition of the covariant derivative,

$$[T_a^{(F)}, T_b^{(F)}] = iC_{abc} T_c^{(F)}. \tag{1.23}$$

It can be shown that $\mathcal{L}_{\text{invariant}}$ is gauge invariant, which actually makes it difficult to quantize. This problem is solved by adding gauge fixing and ghost densities [13–16], $\mathcal{L}_{\text{gauge}} + \mathcal{L}_{\text{ghost}}$. In the

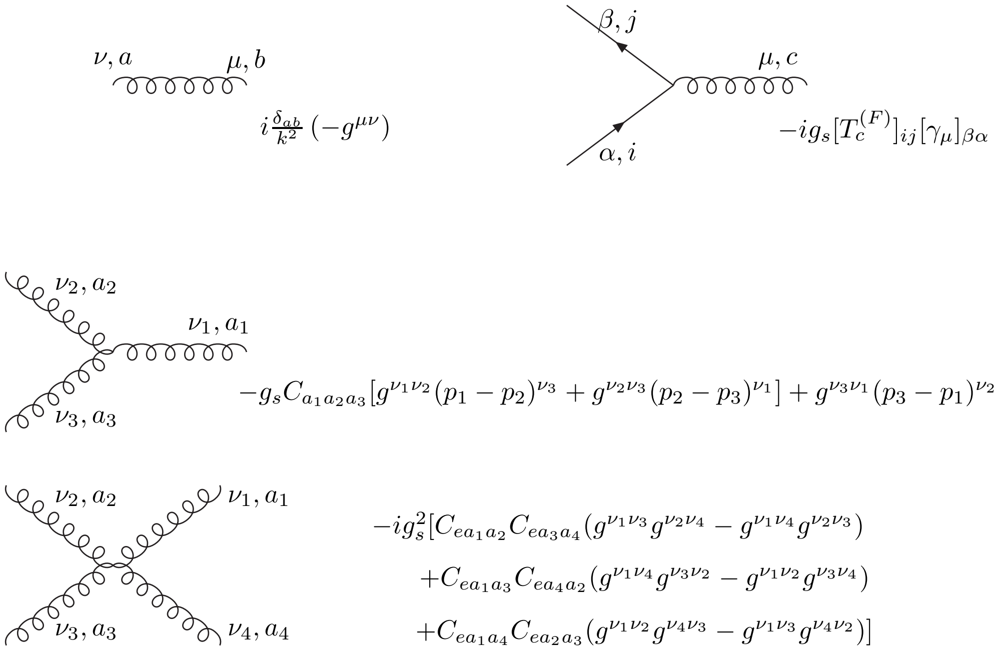

Figure 1.2: Feynman rules for QCD.

covariant gauges, their form is given by

$$\begin{aligned}\mathcal{L}_{\text{gauge}} &= -\frac{\lambda}{2}\sum_{a=1}^{N_c^2-1}(\partial_\mu A_a^\mu)^2 \quad 1<\lambda<\infty, && (1.24)\\ \mathcal{L}_{\text{ghost}} &= (\partial_\mu \bar{c}_a)(\partial^\mu \delta_{ad} - g_s C_{abd} A_b^\mu)c_d, && (1.25)\end{aligned}$$

where $c_a(x)$ and $\bar{c}_a(x)$ are scalar ghost and anti-ghost fields. In the quantization procedure, ghost fields anticommute, despite their spin. In an $SU(N_c)$ theory, the ghost fields ensure that the gauge fixing does not spoil the unitarity of the physical S-matrix that governs the scattering of quarks and gluons in perturbation theory. The ghost fields are of course not physical, and contribution of all unphysical polarizations to the sum of squared matrix element over polarizations equals zero. As a result [17]

$$\sum_{i\in S_{phys}} A_i A_i^* = \sum_{i\in S_{all}} \sigma(i) A_i A_i^*, \tag{1.26}$$

where i is a multi-index for polarization states, A_i is an amplitude of the process, S_{phys} is a set of physical polarization states, S_{all} is a full set of polarizations including unphysical ones and $\sigma(i) = \pm 1$ depending on a signature of the Hilbert space norm of the polarization state i.

Finally, we present in figure 1.2, the feynman rules for QCD.

Chapter 2

Perturbative QCD and ep scattering

2.1 The parton model

The perturbative QCD approach for computing hadronic cross sections is based on the parton model picture, in which the cross section for any hard scattering process can be written as a convolution of structure ($f_a(x, Q^2)$) and fragmentation ($D_a(x, Q^2)$) functions of partons (quarks and gluons) and a hard cross-section factor [18]. The structure and fragmentation functions are non-perturbative, universal quantities, that is, they do not depend on the process used to obtain them. On the other hand, the hard-cross section can be calculated within perturbative QCD to the lowest order in the running coupling $\alpha_s(Q)$ as long as $Q \gg \Lambda$, where Λ is the QCD scale.
This naïve parton model corresponds to the leading order (LO) approximation. However, due to the perturbative nature of α_s, the running of the coupling constant could be hidden in higher order corrections and therefore the LO calculation can only predict the order of magnitude of a given cross section. The accuracy of the perturbative QCD expansion is then controlled by the size of the higher-order contributions. Any perturbative QCD prediction needs then, next-to-leading (NLO) corrections and NLO definitions of the running coupling constant, and the structure and fragmentation functions.

We are interested in deep inelastic scattering (DIS) processes, of the form

$$l(k) + p(P) \to l'(k') + X, \tag{2.1}$$

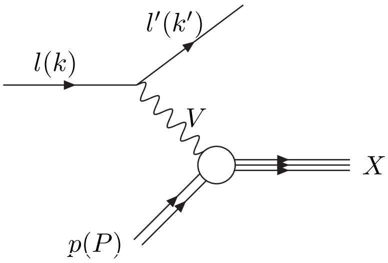

Figure 2.1: Deep inelastic scattering.

mediated by a vector boson, where $l(k)$ and $l'(k)$ represent an incoming and outgoing lepton of momentum k^μ and k'^μ respectively, $p(P)$ a hadron of momentum P^μ and X an arbitrary hadronic state. The process is illustrated in figure 2.1.

We define the momentum transfer in DIS as

$$\begin{aligned} q^\mu &= k^\mu - k'^\mu, \\ -q^2 &= Q^2, \end{aligned} \tag{2.2}$$

and introduce the Bjorken scaling variable x,

$$x = \frac{Q^2}{2P \cdot q}. \tag{2.3}$$

Furthermore, we will need the dimensionless variable y,

$$y = \frac{P \cdot q}{P \cdot k}, \tag{2.4}$$

that measures the ratio of energy transferred to the hadronic system and the total leptonic energy available in the target rest frame [5].

At lowest order in electroweak interactions, the cross section may be split into leptonic and hadronic parts,

$$\frac{d\sigma}{dxdy} = \frac{2\pi y \alpha^2}{Q^4} \sum_n \lambda_n l_n^{\mu\nu} W_{\mu\nu}^n. \tag{2.5}$$

In the case of neutral current exchange, the index n runs over $n = \gamma, Z$ and γZ, and represents pure photon, Z exchange and the interference between them, respectively. For charged current interactions there is only W exchange, $n = W$. $l_{\mu\nu}$ is the lepton tensor associated with the coupling of the exchange boson to the leptons:

$$l_\gamma^{\mu\nu} = 2\left(k^\mu k'^\nu + k^\nu k'^\mu - k \cdot k' g^{\mu\nu}\right), \tag{2.6}$$

$$l_{\gamma Z}^{\mu\nu} = 2 g_V^e \left(k^\mu k'^\nu + k^\nu k'^\mu - k \cdot k' g^{\mu\nu}\right) - 2 i g_A^e \epsilon^{\mu\nu\alpha\beta} k_\alpha k'_\beta, \tag{2.7}$$

$$l_Z^{\mu\nu} = 2\left({g_V^e}^2 + {g_A^e}^2\right)\left(k^\mu k'^\nu + k^\nu k'^\mu - k \cdot k' g^{\mu\nu}\right) - 4 i g_V^e g_A^e \epsilon^{\mu\nu\alpha\beta} k_\alpha k'_\beta, \tag{2.8}$$

$$l_W^{\mu\nu} = 4\left(k^\mu k'^\nu + k^\nu k'^\mu - k \cdot k' g^{\mu\nu} - i \epsilon^{\mu\nu\alpha\beta} k_\alpha k'_\beta\right), \tag{2.9}$$

where $g_V^e = -\frac{1}{2} + 2\sin^2\theta_W$, $g_A^e = -\frac{1}{2}$, and we have introduced the total antisymmetric tensor ε:

$$\mathrm{Tr}(\gamma_5\gamma_\alpha\gamma_\beta\gamma_\gamma\gamma_\delta) = 4i\varepsilon_{\alpha\beta\gamma\delta}. \tag{2.10}$$

The factors λ_n denote the ratios of the corresponding propagators and couplings to the photon propagator and coupling squared [19]:

$$\lambda_\gamma = 1 \quad ; \quad \lambda_{\gamma Z} = \left(\frac{G_F M_Z^2}{2\sqrt{2}\pi\alpha}\right)\left(\frac{Q^2}{Q^2+M_Z^2}\right); \tag{2.11}$$

$$\lambda_Z = \lambda_{\gamma Z}^2 \quad ; \quad \lambda_W = \frac{1}{2}\left(\frac{G_F M_W^2}{4\pi\alpha}\frac{Q^2}{Q^2+M_W^2}\right)^2. \tag{2.12}$$

On the other hand, the hadron tensor is defined to all orders in the strong interaction in terms of the matrix elements

$$W^p_{\mu\nu}(P,q) = \frac{1}{8\pi}\sum_{\text{spin}}\int d^4x e^{iqx} < P|J^+_\mu(x)J_\nu(0)|P > . \tag{2.13}$$

Symmetry properties impose restrictions on the form the hadron tensor can take, which can be summarized by expanding the tensor in terms of scalar structure functions F_i:

$$\begin{aligned} W^p_{\mu\nu}(P,q) &= \left(-g_{\mu\nu} + \frac{q_\mu q_\nu}{q^2}\right)F_1^p(x,Q^2) + \left(P_\mu - \frac{P\cdot q}{q2}q_\mu\right)\left(P_\nu - \frac{P\cdot q}{q2}q_\nu\right)\frac{1}{P\cdot q}F_2^p(x,Q^2) \\ &- \frac{i}{2}\varepsilon_{\mu\nu\alpha\beta}\frac{P^\alpha q^\beta}{P\cdot q}F_3^p(x,Q^2). \end{aligned} \tag{2.14}$$

The cross sections for neutral current (NC) and charged current (CC) deep inelastic scattering can be written in terms of the structure functions in the generic form,

$$\frac{d\sigma^i}{dxdy} = \frac{4\pi\alpha^2}{xyQ^2}\lambda_i\left(y^2xF_1^i + (1-y)F_2^i \mp \left(y - \frac{y^2}{2}\right)xF_3^i\right), \tag{2.15}$$

where $i = \mathrm{NC}, \mathrm{CC}$. The CC structure functions are

$$F_1^{\mathrm{CC}} = F_1^W, F_2^{\mathrm{CC}} = F_2^W, xF_3^{\mathrm{CC}} = xF_3^W. \tag{2.16}$$

For NC, they are given by [20]:

$$F_2^{\mathrm{NC}} = F_2^\gamma - g_V^e\lambda_{\gamma Z}F_2^{\gamma Z} + \left({g_V^e}^2 + {g_A^e}^2\right)\lambda_Z F_2^Z, \tag{2.17}$$

and similarly for F_1^{NC}. We also get

$$xF_3^{\mathrm{NC}} = -g_A^e\lambda_{\gamma Z}xF_3^{\gamma Z} + 2g_V^e g_A^e\lambda_Z xF_3^Z. \tag{2.18}$$

In the quark parton model, the proton is assumed to be composed of point-like free objects called partons. In this way inelastic electron-proton scattering can be described in terms of the elastic scattering of the electron with a parton $q = u, d, ...$ and the probability $q(x,Q^2)$ of finding this parton with momentum x inside the proton, known as Parton Distribution Function (PDF). Contributions to the structure functions can be expressed in terms of the parton distribution functions. For the neutral current processes $ep \rightarrow eX$,

$$
\begin{aligned}
F_2^{\gamma} &= x \sum_q e_q^2 \left(q + \bar{q}\right), && (2.19)\\
F_2^{\gamma Z} &= x \sum_q 2 e_q g_V^q \left(q + \bar{q}\right), && (2.20)\\
F_2^{Z} &= x \sum_q \left({g_V^q}^2 + {g_A^q}^2\right) \left(q + \bar{q}\right), && (2.21)\\
F_3^{\gamma} &= 0, && (2.22)\\
F_3^{\gamma Z} &= \sum_q 2 e_q g_A^q \left(q - \bar{q}\right), && (2.23)\\
F_3^{Z} &= \sum_q 2 g_V^q g_A^q \left(q - \bar{q}\right), && (2.24)
\end{aligned}
$$

where $g_V^q = \pm\frac{1}{2} - 2e_q \sin^2\theta_W$ and $g_A^q = \pm\frac{1}{2}$, with ± according to whether q is a u or d type quark respectively. For the charged current processes $e^- p \rightarrow \nu X$ and $\bar{\nu} p \rightarrow e^+ X$, the structure functions are:

$$
\begin{aligned}
F_2^{W^-} &= 2x \left(u + \bar{d} + c + \bar{s} + ...\right), && (2.25)\\
F_3^{W^-} &= 2 \left(u - \bar{d} + c - \bar{+} ...\right), && (2.26)\\
& && (2.27)
\end{aligned}
$$

where only the active flavours are to be kept and where CKM mixing has been neglected. In the case of $F_2^{W^+}$ and $F_3^{W^+}$, the result is obtained by interchanging $d \leftrightarrow u$ type quarks.

One of the features of structure functions in the quark parton model is that they scale, that is, $F_i(x, Q^2) \rightarrow F_i(x)$ in the limit that $Q^2 \rightarrow \infty$ and with x fixed [21]. This prediction is known as Bjorken scaling and was verified experimentally at SLAC [22] confirming the presence of charged constituents in the proton. This property is related to the assumption that the transverse momentum of the partons in the infinite-momentum frame of the proton is small. However, if the proton were only composed of charged particles, the sum of their momenta should equal the proton momentum, i.e. the sum of their fractional momenta would be unity:

$$\sum \int_0^1 dx q(x) x = 1. \qquad (2.28)$$

This is not what is observed experimentally, where it was found that quarks constitute only $\sim 50\%$ of the proton's momentum [23], suggesting that neutral particles also existed in the proton. These were identified as gluons and direct evidence of their existence was observed in e^+e^- collisions in the form of 3-jet events [24]. The modification of the quark parton model to include gluons formed what became QCD.

In QCD, the proton can be described as a dynamical system of quarks and gluons. Gluons can be emitted and absorbed by the quarks and can split to produce pairs of quarks or gluons. In this way it is possible for a parton to gain transverse momentum relative to the proton direction leading to logarithmic scaling violations, which are particularly large at small x [19]. The radiation of gluons produces the evolution of the structure functions. As Q^2 increases, more and more gluons are radiated, which then split into $q\bar{q}$ pairs. This leads to the softening of the initial quark momentum distributions and to the growth of the gluon density and the $q\bar{q}$ sea as x decreases. In QCD, this process is described in terms of scale dependent parton distributions $f_a(x, \mu^2)$, where a is now either a quark or a gluon.

Because of this gluon radiation, the structure function F_2 has a dependence on Q^2 as well as on x as shown in Fig. 2.2. In low Q^2 events the photon can resolve the valence quark substructure of the proton whereas in high Q^2 events more and more partons can be resolved. As Q^2 increases there is a decreased probability of finding a quark at large x values because high-momentum quarks would lose momentum by radiating gluons. So for large values of x the value of F_2 decreases as a function of Q^2. Consequently there is an increased probability of finding a quark at low x and so here F_2 rises as a function of Q^2. This behaviour of the structure function is known as scaling violation and can be clearly seen in figure 2.2 [25, 26].

2.2 Evolution of parton densities

Although the precise mathematical form of PDFs cannot be calculated from first principles, a functional form can be postulated and then used to fit experimental data. A functional form of the dependence of the structure functions on $\log Q^2$ can be found by incorporating a term due to gluon emission into equation 2.19:

$$\frac{F_2(Q^2, x)}{x} = \sum_i e_i^2 \left(q_i(x) + \frac{\alpha_s}{2\pi} \log \frac{Q^2}{\mu^2} \int_x^1 \frac{dy}{y} q_i(y) P_{qq}\left(\frac{x}{y}\right) \right), \tag{2.29}$$

where $q_i = f_i$, the quark structure function and μ is an appropriate scale, typically chosen to avoid singularities when transverse momentum squared tends to zero. $P_{qq}\left(\frac{x}{y}\right)$ is known as the splitting function which is the probability of a quark with momentum y emitting a gluon and emerging with momentum x. Predictions of the structure function which have been measured at one experiment can be used at another, as long as it is evolved to the correct scale. Given some reference value of the quark density, the evolution of q_i with $\log Q^2$ can be calculated as:

$$\frac{dq_i(x, Q^2)}{d \log Q^2} = \frac{\alpha_s}{2\pi} \int_x^1 \frac{dy}{y} q_i(y, Q^2) P_{qq}\left(\frac{x}{y}\right). \tag{2.30}$$

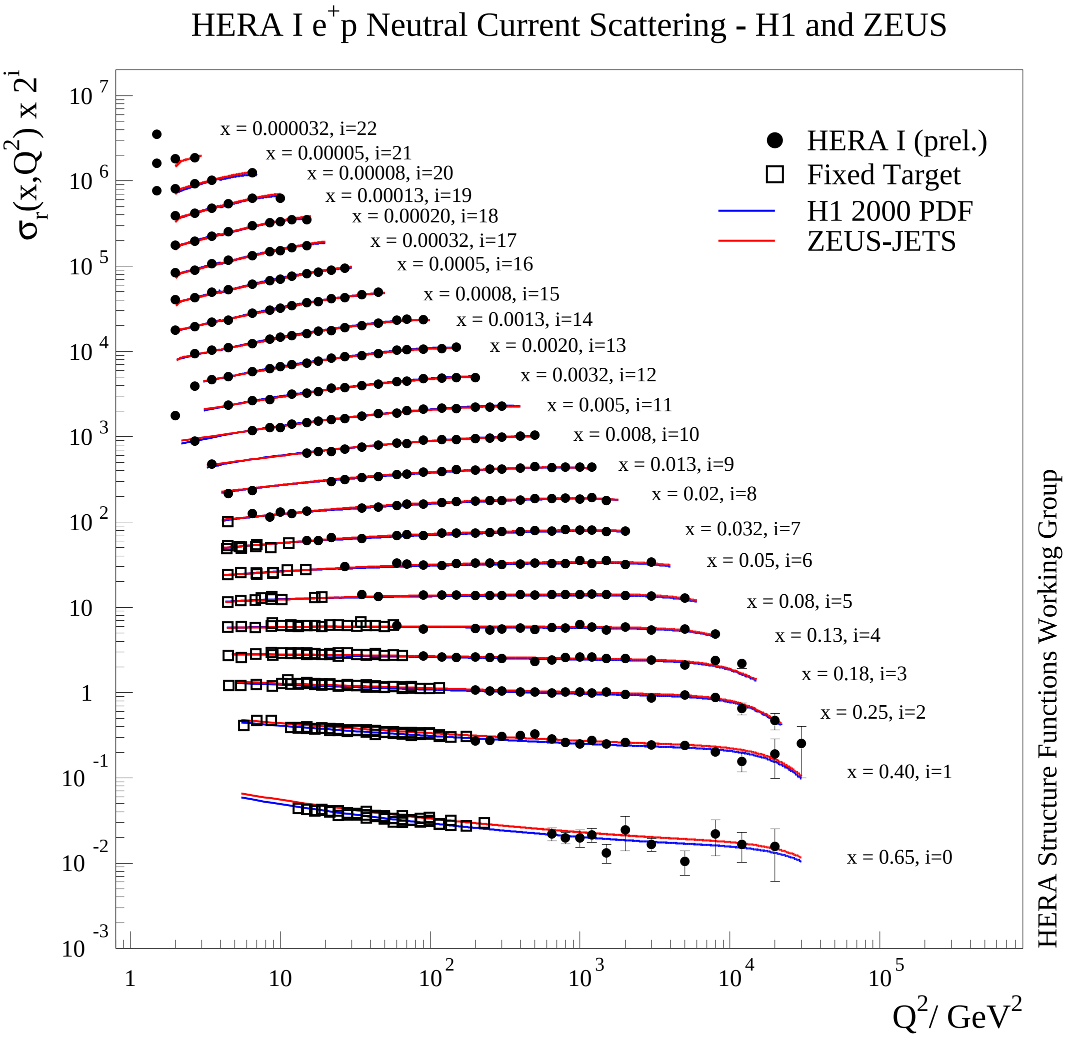

Figure 2.2: The reduced cross section $\sigma_r(x, Q^2)$ as a function of Q^2 for fixed values of x. Results from fixed target experiments and the combined ZEUS-H1 HERA I measurements are compared to an NLO QCD fit from each of the experiments, H12000PDF and ZEUS-JETS.

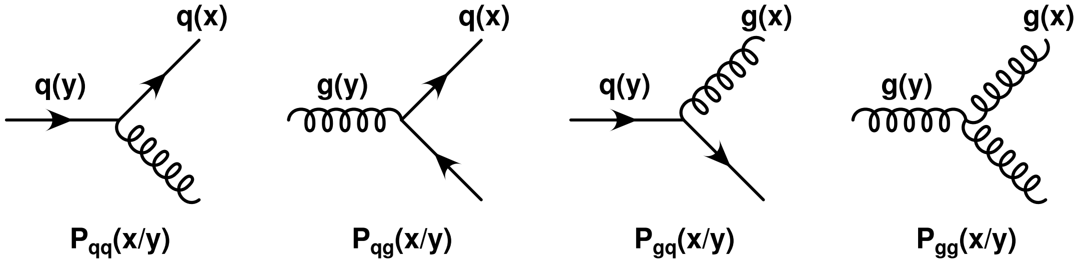

Figure 2.3: The first order splitting functions P_{ij} used in the DGLAP equations.

In addition, there can be a contribution to the quark density from quarks produced in a pair originating from a gluon, modifying equation 2.30 to give:

$$\frac{dq_i(x,Q^2)}{d\log Q^2} = \frac{\alpha_s}{2\pi}\int_x^1 \frac{dy}{y}\left[q_i(y,Q^2)P_{qq}\left(\frac{x}{y}\right) + g(y,Q^2)P_{qg}\left(\frac{x}{y}\right)\right], \tag{2.31}$$

where $g(y,Q^2)$ is the gluon density function. Similarly, the gluon density evolution equations can be found using the same procedure:

$$\frac{dg(x,Q^2)}{d\log Q^2} = \frac{\alpha_s}{2\pi}\int_x^1 \frac{dy}{y}\left[\sum_i q_i(y,Q^2)P_{gq}\left(\frac{x}{y}\right) + g(y,Q^2)P_{gg}\left(\frac{x}{y}\right)\right]. \tag{2.32}$$

Equations 2.31 and 2.32 are called the DGLAP equations [27–30] and are used to describe the evolution of the parton densities. The terms P_{ij} are the splitting functions for the processes shown in Fig. 2.3 and can be interpreted as the probability of a parton j with momentum fraction y emitting a parton and emerging with momentum fraction x. To one loop, they are given by

$$P_{qq}^{(1)}(x) = C_f\left[(1+x^2)\left(\frac{1}{1-x}\right)_+ + \frac{3}{2}\delta(1-x)\right], \tag{2.33}$$

$$P_{qg}^{(1)}(x) = \frac{1}{2}\left[(1-x)^2 + x^2\right], \tag{2.34}$$

$$P_{gq}^{(1)}(x) = C_f\frac{(1-x)^2+1}{x}, \tag{2.35}$$

$$P_{gg}^{(1)}(x) = 2N_c\left[\frac{x}{(1-x)_+} + \frac{1-x}{x} + x(1-x)\right] + \left(\frac{11}{6}N_c - \frac{1}{3}n_f\right)\delta(1-x). \tag{2.36}$$

The DGLAP equations are valid at high Q^2 and high x but not at low x where $\log\left(\frac{1}{x}\right)$ terms become important.

2.3 Factorization theorem

The main goal of perturbative QCD is to find a justification for the parton model in field theory, and to improve the parton model's description of experimental data. The field theory realization of the parton model is the theorem of factorization of long-distance from short-distance dependence for deep inelastic scattering [31]. This theorem states that the sum of all the diagrammatic contributions to the structure functions is a direct generalization of the parton model results given by,

$$F_n^h(x,Q^2) = \sum_i \int_0^1 d\xi C_n^i \left(\frac{x}{\xi}, \frac{Q^2}{\mu^2}, \frac{\mu_f^2}{\mu^2}, \alpha_s(\mu^2) \right) f_i^h(\xi, \mu_f, \mu^2), \tag{2.37}$$

where i denotes all partons: quarks, antiquarks and gluons, h is the initial hadron and $n = 1, 2, 3$. Here we see the dependence of two scales, μ and μ_f. The first one is the renormalization scale, needed in any perturbative calculation. The second however, is specific to factorization calculations, and is called the factorization scale [5]. Its job is to separate short-distance from long-distance effects. In other words, any propagator that is off-shell by μ_f^2 or more will contribute to C_n^i, while below this scale, it will be grouped into f_i^p. The precise definition of the factorization scale is made when we give a formal definition of the parton distributions.

Each function C_n^i is infrared safe, calculable in perturbation theory. It depends on the parton i, the exchanged vector boson and on the renormalization and factorization scales but it is independent of long-distance effects. In particular, it is independent of the initial hadron. On the other hand, the parton distribution, f_i^h, contains all the infrared sensitivity of the original cross section. It is specific to the hadron h and depends on the factorization scale. However, it is universal, that is, it is independent of the particular process been studied.

The way in which the factorization theorem is used in practice becomes clear now. The coefficients, C_n^i, are to be computed in perturbation theory, and f_i^h are to be measured by comparing the structure functions in equation 2.37 with experiment, given a set of expressions for the C^i's. Once the parton distributions have been determined, they can be used in any other process to calculate a different cross section. Thanks to the evolution theorem, PDFs can be obtained for different scales through the DGLAP evolution quations. We will use here PDF sets from the CTEQ [32] and MSTW [33] collaborations.

In practice, to calculate the C_n^i, we use the fact that they are independent of the external hadron, so we can calculate them in perturbation theory, replacing the hadron with a parton.

It is also possible that partons in the final state could combine to form a final state hadron. This fragmentation process is described by non-perturbative *fragmentation functions* D_i^h, that have the same properties as the parton distribution functions. They are obtained from experimental data and since they are universal, it is possible to use them in any other process. In the same way as with the parton distribution functions, fragmentation functions can be evolved and obtained for different scales. We will use in this work several sets of fragmentation functions [34–36], depending on the comparison we want to make, i.e., the hadron we consider in the final state.

It is thanks to the factorization and evolution theorems that we are able to calculate using perturbative QCD to then compare our results with experimental data. In this thesis we will compare our results with data from the H1 and ZEUS collaborations at HERA. In the next section we will explain briefly the features of these experiments.

2.4 HERA

The Hadron-Elektron Ring Anlage (HERA), was a particle accelerator which collided electrons or positrons and protons. It was located 10-20 m underground beneath the Deutsches Elektronen-Synchrotron (DESY) site and the Hamburg Volkspark. During its history, HERA operated at four different proton beam energies. After an initial electron beam energy of 26.7 GeV, HERA ran at 27.5 GeV from 1995 until the end of running. Until the end of 1997, it collided the electron beam with a 820 GeV proton beam, yielding a centre-of-mass energy $\sqrt{s} = 300$ GeV. In 1997, the proton beam energy was increased to 920 GeV increasing the centre-of-mass energy to $\sqrt{s} = 318$ GeV. The final two running periods took place in 2007 are known as low-energy and high-energy running (LER and MER) when the proton beam energy was decreased to 460 GeV and 575 GeV respectively. The final collision in HERA took place on 30th June 2007.

The HERA tunnel was 6.3 km long and contained separate storage rings for the electrons and protons which were not circular but had four straight sections, each 360 m in length. The beams were brought to zero crossing-angle collisions in two of these straight sections. These interaction points (IPs) were in the north and south halls where the two multi-purpose detectors, H1 and ZEUS, were located. The other two experiments used fixed target collisions. HERMES, in the east hall, studied collisions of the electron beam with polarised gas to measure nucleon spin. HERA-B, in the west hall, was designed to study the interaction of the proton beam with fixed wire targets in order to investigate $\mathcal{CP}$ violation.

In 2000-2001, HERA was shut down in order to upgrade the machine with the aim of reaching a target integrated luminosity of 1 fb^{-1} by 2007. The hope was that with a higher luminosity being delivered to the experiments, new interesting measurements would be possible [37] such as an investigation into high-x, high-Q^2 events which had been observed by ZEUS and H1 during the HERA I running period. The increase in luminosity was achieved by installing superconducting magnets close to the interaction points in order to make the beam cross section smaller. The upgraded machine was known as HERA II. In this thesis we will compare results with measurements from both periods, HERA I and II, and from both the main experiments H1 and ZEUS.

Chapter 3

Inclusive production of hadrons in DIS at first order in α_s

3.1 Single production of hadrons in DIS

We will now show the basic formalism for single production of hadrons, which is the main focus of this work. The process is of the form

$$l(k) + p(P) \to l(k') + h(p_h) + X, \tag{3.1}$$

where the lepton is either an electron, muon or a (anti)neutrino, and the exchanged vector boson a photon, $W^{\pm}$ or Z (see figure 3.1). Using the factorization theorem, the cross section can be written as a convolution of the partonic cross section with the parton distribution functions and the fragmentation functions:

$$\frac{d\sigma^h}{dxdydzd\phi} = \int_x^1 \frac{d\bar{x}}{\bar{x}} \int_z^1 \frac{d\bar{z}}{\bar{z}} \sum_{ab} f_a^p\left(\frac{x}{\bar{x}}, \mu^2\right) \frac{d\sigma^{ab}}{d\bar{x}dyd\bar{z}d\phi} D_b^h\left(\frac{z}{\bar{z}}, \mu^2\right), \tag{3.2}$$

where we have used the kinematic variables

$$\begin{aligned} x = \frac{Q^2}{2P\cdot q}, \qquad y &= \frac{P\cdot q}{P\cdot k}, \qquad z = \frac{P\cdot p_h}{P\cdot q}, \\ \bar{x} = \frac{Q^2}{2p_a\cdot q}, \qquad \bar{y} &= y, \qquad \bar{z} = \frac{p_a\cdot p_b}{p_a\cdot q}. \end{aligned} \tag{3.3}$$

The partonic cross section may be split into leptonic and hadronic parts,

$$\frac{d^{ab}\sigma}{dxdydz} = \frac{2\pi y\alpha^2}{Q^4} \sum_n \lambda_n L_n^{\mu\nu} H_{\mu\nu}^n. \tag{3.4}$$

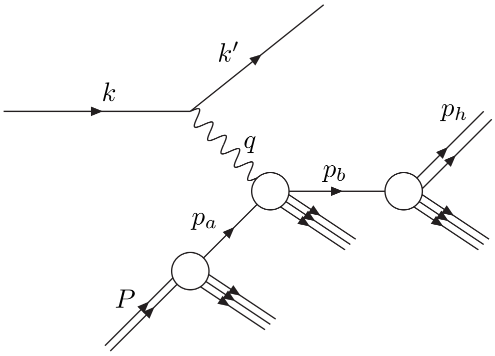

Figure 3.1: Single hadron production in DIS. Parallel trios of lines signify unobserved final states.

where

$$L^{\mu\nu} = \int \frac{d\phi}{(2\pi)^3} l^{\mu\nu}, \tag{3.5}$$

is the integrated lepton tensor and $l^{\mu\nu}$ are the lepton tensors as in equation 2.6. We can write a general ansatz for the integrated lepton tensor as [38]:

$$L^{\mu\nu} = a_1 g^{\mu\nu} + a_2 p_a^\mu p_a^\nu + a_3 q^\mu q^\nu + a_4(p_a^\mu q^\nu + p_a^\nu q^\mu) + a_5(p_a^\mu q^\nu - p_a^\nu q^\mu) + a_6 \epsilon^{\mu\nu\alpha\beta} p_{a\alpha} q_\beta. \tag{3.6}$$

The contraction of both sides of equation 3.6 with each of the six basis tensors on the right hand side yields to six equations for the determination of the unknown coefficients a_i. Our lepton tensor then reads

$$L^{\mu\nu} = \frac{Q^2}{2y}\left(\frac{2-2y+y^2}{y}\right)(-g^{\mu\nu}) + \frac{2Q^4}{s_h^2}\left(\frac{y^2-6y+6}{y^4}\right) p_a^\mu p_a^\nu \pm i\frac{Q^2}{s_h}\left(\frac{y-2}{y^2}\right)\varepsilon^{\mu\nu\alpha\beta} p_{a\alpha} q_\beta \tag{3.7}$$

with $s_h = \frac{Q^2}{\bar{x}y}$. The last term is positive if the lepton interacting with the vector boson is an electron, and negative if it is a positron. This way, the hadronic tensor can be split into metric, longitudinal and axial components:

$$H_M^{ab} = -g^{\mu\nu} H_{\mu\nu}^{ab}, \tag{3.8}$$

$$H_L^{ab} = p_a^\mu p_a^\nu H_{\mu\nu}^{ab}, \tag{3.9}$$

$$H_A^{ab} = \pm i\varepsilon^{\mu\nu\alpha\beta} p_{a\alpha} q_\beta H_{\mu\nu}^{ab}, \tag{3.10}$$

$$\tag{3.11}$$

where

$$H_{\mu\nu}^{ab} = \sum_{\text{spins}} \mathcal{M}_\mu^\dagger \mathcal{M}_\nu \tag{3.12}$$

is the squared amplitude that we calculate analytically. In the same way, the coefficients λ can be written as

$$\lambda_{NC}^{M,L} = e_q^2 - 2e_q v_q^Z v_e^Z \chi_Z(Q^2) + \left(a_q^{Z^2} + v_q^{Z^2}\right)\left(a_e^{Z^2} + v_e^{Z^2}\right)\chi_Z^2(Q^2), \tag{3.13}$$

$$\lambda_{NC}^{A} = -2e_q a_q^Z a_e^Z \chi_Z(Q^2) + 4a_q^Z a_e^Z v_q^Z v_e^Z \chi_Z^2(Q^2), \tag{3.14}$$

where

$$a_{e,q}^Z = T_{e,q}^3, \tag{3.15}$$

$$v_{e,q}^Z = T_{e,q}^3 - 2e_{e,q}\sin^2\theta_W, \tag{3.16}$$

$$\chi_Z(Q^2) = \frac{1}{4\sin^2\theta_W\cos^2\theta_W}\frac{Q^2}{Q^2+M_Z^2}, \tag{3.17}$$

and $T_{\nu,u}^3 = \frac{1}{2}$, $T_{e,d}^3 = -\frac{1}{2}$, for neutral-current exchange. For charged-current exchange we have

$$\lambda_{CC}^{M,L} = \left(a_q^{W^2} + v_q^{W^2}\right)\left(a_e^{W^2} + v_e^{W^2}\right)\chi_W^2(Q^2), \tag{3.18}$$

$$\lambda_{CC}^{A} = 4a_q^W a_e^W v_q^W v_e^W \chi_W^2(Q^2), \tag{3.19}$$

with

$$a_e^W = v_e^W = \frac{1}{2\sqrt{2}}, \tag{3.20}$$

$$a_q^W = v_q^W = \frac{\text{CKM}[q,q']}{2\sqrt{2}}, \tag{3.21}$$

$$\chi_W(Q^2) = \frac{1}{\sin^2\theta_W}\frac{1}{Q^2+M_W^2}, \tag{3.22}$$

where CKM$[q,q']$ denotes the CKM matrix element corresponding to the coupling of the respective quarks.

3.2 Treatment of γ_5

When calculating the squared amplitude at next-to-leading order, we have to include virtual and real corrections to the born level diagrams. Singularities will then appear and they have to be regularised and renormalized in the standard way. However, here we find a problem. In dimensional regularisation, amplitudes are calculated in n dimensions, which requires the definition of the γ matrices involved in n dimensions. In our case, when we want to include electroweak currents in the DIS process, parity violating γ_5 matrices appear that are not defined in n dimensions. This problem is well known and has been discussed in several papers [39–42]. To illustrate the situation, let us show that an anticommuting γ_5,

$$\{\gamma_\mu, \gamma_5\} = 0, \tag{3.23}$$

is not compatible with an n-dimensional Dirac algebra [43],

$$\gamma_\mu \gamma^\mu = g^\mu_\mu = n. \tag{3.24}$$

If we consider the trace $\mathrm{Tr}(\gamma_5 \gamma_\alpha \gamma_{\mu_1} \gamma_{\mu_2} \gamma_{\mu_3} \gamma_{\mu_4} \gamma_{\mu_5})$ and anticommute γ_α once around the trace, we can see that this leads to

$$\varepsilon_{\mu_1 \mu_2 \mu_3 \mu_4} g_{\mu_5 \alpha} + \mathrm{cycl.}(\mu_1 ... \mu_5) = 0, \tag{3.25}$$

where the antisymmetric tensor ε is the one defined in equation 2.10. Contracting this last expression with $g^{\alpha \mu_5}$ gives

$$(n-4) \varepsilon_{\mu_1 \mu_2 \mu_3 \mu_4}, \tag{3.26}$$

which shows that equations 3.23 and 3.24 prevent one from analytically continuing $\mathrm{Tr}(\gamma_5 \gamma_\alpha \gamma_\beta \gamma_\gamma \gamma_\delta)$ or $\varepsilon_{\alpha\beta\gamma\delta}$ from 4 to $n \neq 4$ [43]. In the past, several approaches have been used to avoid this problem. In reference [41], the authors worked with an anticommuting γ_5 matrix but dropped equation 3.24. However, this prescription can not be applied in general, for higher-order infra-red calculations with multiple γ contractions inside parity-odd traces. The author in [40], chose also to anticommute γ_5 but to keep the Dirac algebra in four dimensons. It can be shown that this is not a consistent procedure [43]. The third possibility is the one proposed by 'tHooft and Veltman [42], and later systematized by Breitenlohner and Maison (BM) [39]. We will use the third scheme in this work for our calculations. In the BM scheme, a n-dimensional a_μ can be split up into its 4-dimensional component $\hat{\hat{a}}_\mu$ and the remaining component $\hat{a}_\mu$. Therefore, we can write $\gamma_\mu = \hat{\hat{\gamma}}_\mu + \hat{\gamma}_\mu$ and a consistent γ_5 scheme is obtained by postulating

$$\begin{aligned} \hat{\hat{\gamma}}_\mu \gamma_5 + \gamma_5 \hat{\hat{\gamma}}_\mu &= 0, \qquad (3.27) \\ \hat{\gamma}_\mu \gamma_5 - \gamma_5 \hat{\gamma}_\mu &= 0. \qquad (3.28) \end{aligned}$$

The correct version of equation 3.25 can now be obtained by considering the trace $\mathrm{Tr}(\gamma_5 \hat{\hat{\gamma}}_\alpha \gamma_{\mu_1} \gamma_{\mu_2} \gamma_{\mu_3} \gamma_{\mu_4} \gamma_{\mu_5})$:

$$\varepsilon_{\mu_1 \mu_2 \mu_3 \mu_4} \hat{\hat{g}}_{\mu_5 \alpha} + \mathrm{cycl.}(\mu_1 ... \mu_5) = 0, \tag{3.29}$$

where we have used $\hat{\hat{\gamma}}_\mu \gamma_\nu + \gamma_\nu \hat{\hat{\gamma}}_\mu = 2 \hat{\hat{g}}_{\mu\nu}$ and $\hat{\hat{g}}_{\mu\nu}$ is the 4-dimensional metric tensor. A suitable representation for γ_5 is [39, 42, 44–46]

$$\gamma_5 = \frac{1}{4!} \varepsilon_{\alpha\beta\gamma\delta} \gamma_\alpha \gamma_\beta \gamma_\gamma \gamma_\delta. \tag{3.30}$$

Using the identity

$$\varepsilon_{\mu_1 \mu_2 \mu_3 \mu_4} \varepsilon_{\nu_1 \nu_2 \nu_3 \nu_4} = -\det(\hat{\hat{g}}_{\alpha\beta}), \tag{3.31}$$

where $\alpha = \mu_1 ... \mu_4$ and $\beta = \nu_1 ... \nu_4$, it can be shown that

$$\varepsilon_{\alpha\beta\gamma\delta} \hat{g}^{\delta\rho} = 0, \tag{3.32}$$

and that

$$g^{\beta}_{\alpha}\hat{\hat{g}}_{\beta\gamma} = \hat{\hat{g}}_{\alpha\gamma}. \tag{3.33}$$

Equation 3.32 shows that the ε-tensor projects out the 4-dimensional components of any n-dimensional tensor it acts on. From equation 3.32 it is clear that the identity in equation 3.29 must involve the 4-dimensional metric tensor when comparing the different tensor components in equation 3.29.

In practice, the BM scheme can be implemented by observing two simple rules [44]: 1) Do not commute by γ_5, 2) The trace $-i/4\mathrm{Tr}(\gamma_5\gamma_\alpha\gamma_\beta\gamma_\gamma\gamma_\delta)$ equals the conventional antisymmetric tensor $\varepsilon_{\alpha\beta\gamma\delta}$ in four dimensions if the tensor indices $\alpha, \beta, \gamma, \delta$ are 4-dimensional and equals zero otherwise. Furthermore, the renormalization of the 1-loop axial vector current contribution must include appropriate counter terms to cancel spurious ultraviolet anomalies such that

$$\begin{aligned} &\left\langle J^V_\mu(\text{Born})J^{A*}_\nu(\text{1-loop})\right\rangle + \left\langle J^A_\mu(\text{1-loop})J^{V*}_\nu(\text{Born})\right\rangle = \\ &\left\langle J^A_\mu(\text{Born})J^{V*}_\nu(\text{1-loop})\right\rangle + \left\langle J^V_\mu(\text{1-loop})J^{VA*}_\nu(\text{Born})\right\rangle . \end{aligned} \tag{3.34}$$

The calculation of these counter terms can be found in [45, 46], where γ_5 was taken as in equation 3.30. Equivalently, the axial current can be defined as

$$A_\mu = \bar{\psi}\gamma_\mu\gamma_5\psi = \frac{1}{6}\varepsilon_{\mu\alpha\beta\gamma}\bar{\psi}\gamma_\alpha\gamma_\beta\gamma_\gamma\psi. \tag{3.35}$$

However, both definitions violate the Ward identity. To restore it, a finite renormalization of the axial current must be performed, where a finite axial charge $Z_5(\alpha_s)$ is introduced:

$$A_\mu \to Z_5 A_\mu. \tag{3.36}$$

This charge Z_5 that we will use in our calculations was found to be [45, 46]

$$Z_5 = 1 - \frac{\alpha_s}{\pi}C_F + \left(\frac{\alpha_s}{\pi}\right)^2\left(\frac{11}{8}C_F^2 - \frac{107}{144}C_F C_A + \frac{1}{72}C_F n_f\right) + O(\alpha^3). \tag{3.37}$$

In all our calculations of virtual corrections where this approach was needed, we always checked that introducing this counter term leads to expressions that respect equation 3.34.

3.3 Calculations to $O(\alpha_s)$

To zeroth order in α_s, the process $V + q \to q$ is the only contribution to single hadron production. In order to obtain the NLO prediction, we need to include virtual and real corrections to this process to first order in α_s. Figures 3.2 and 3.3 show the relevant feynman diagrams. At the Born level, the hadron tensor is simply

$$\begin{aligned} H^{\text{PC}}_{\mu\nu,\text{Born}} &= 4\left(p_{a\mu}p_{b\nu} + p_{b\mu}p_{a\nu} - \frac{q^2}{2}g_{\mu\nu}\right) && (3.38)\\ H^{\text{PV}}_{\mu\nu,\text{Born}} &= 4i\varepsilon_{\mu\nu q p_a}, && (3.39) \end{aligned}$$

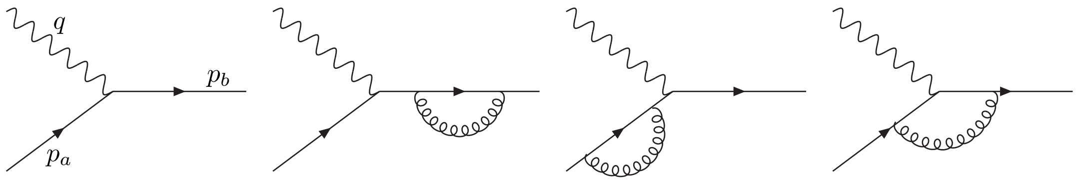

Figure 3.2: Born process and virtual corrections to first order in α_s.

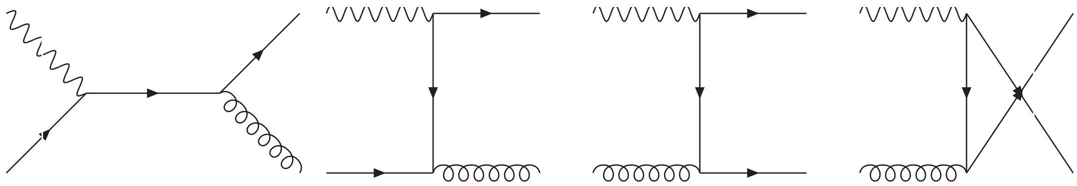

Figure 3.3: Real corrections to first order in α_s.

where $\varepsilon^{\mu\nu\alpha\beta}$ is the Levi-Civita tensor and the momenta are as indicated on the diagrams. The notation PC and PV stands for parity-conserving part and parity-violating part respectively.

3.4 Virtual and real corrections

As we mentioned before, our cross section is given by equation 3.2, and we need to calculate the partonic cross section to first order in α_s using equation 3.4. To calculate the virtual corrections we use standard regularization and renormalization techniques to express all singularities in terms of ϵ terms, where $\epsilon = (4 - D)/2$. These singularities will then cancel against collinear and infrared singularities coming from the real corrections. The result is well known [44, 47]:

$$H^{\mathrm{PC,PV}}_{\mu\nu,\mathrm{virt}} = \frac{\alpha_s}{2\pi} C_F \left(\frac{4\pi\mu^2}{Q^2}\right)^{\epsilon} \frac{\Gamma(1+\epsilon)\Gamma^2(1-\epsilon)}{\Gamma(1-2\epsilon)} \left(-\frac{2}{\epsilon^2} - \frac{3}{\epsilon} - 8 + \mathcal{O}(\epsilon)\right) H^{\mathrm{PC,PV}}_{\mu\nu,\mathrm{Born}}. \quad (3.40)$$

The real corrections can be calculated from the diagrams shown in figure 3.3. In terms of our kinematic variables, defined in 3.3, we get:

$$
\begin{aligned}
H^{qq}_{M,\mathrm{real}} &= 16\alpha_s C_F \frac{1+(1-x-z)^2}{(1-x)(1-z)}, \\
H^{qq}_{L,\mathrm{real}} &= 8\alpha_s C_F Q^2 \frac{z}{x}, \\
H^{qq}_{A,\mathrm{real}} &= 8\alpha_s C_F \frac{Q^2}{x}\left(\frac{(1-2z)x^2-2(1-z)^2x+(2-z)z}{(1-x)(1-z)}\right), \\
H^{qg}_{M,\mathrm{real}} &= 16\alpha_s C_F \frac{1+(x-z)^2}{(1-x)z}, \\
H^{qg}_{L,\mathrm{real}} &= 8\alpha_s C_F Q^2 \frac{1-z}{x}, \\
H^{qg}_{A,\mathrm{real}} &= 8\alpha_s C_F \frac{Q^2}{x}\left(\frac{2zx^2-x^2-(2x-1)z^2-1}{(1-x)z}\right), \\
H^{gq}_{M,\mathrm{real}} &= \frac{16\alpha_s N_c C_F}{N_c^2-1}\frac{1-2x(1-x)-2z(1-z)}{z(1-z)}, \\
H^{gq}_{L,\mathrm{real}} &= \frac{16\alpha_s N_c C_F Q^2}{N_c^2-1}\frac{1-x}{x}, \\
H^{gq}_{A,\mathrm{real}} &= \frac{8\alpha_s N_c C_F Q^2}{N_c^2-1}\frac{(1-2z)(2(x-1)x+1)}{xz(1-z)},
\end{aligned}
\tag{3.41}
$$

which is in agreement with the literature [44,48,49]. Using these results we can now calculate cross sections and compare with different sets of data.

Chapter 4

Inclusive production of hadrons in DIS to second order in α_s

To second order in α_s, the LO contribution comes from the diagrams in figure 3.3 and in the same way as before, we need to calculate virtual and real corrections for these diagrams.

In this case however, the cancellation of singularities is not straightforward and we make use of the *subtraction method* [18], to cancel all divergences at NLO.

4.1 The subtraction method

Our NLO cross section could be written as

$$\sigma = \sigma^{LO} + \sigma^{NLO}, \tag{4.1}$$

where the LO cross section is obtained by integrating the Born cross section over the corresponding phase space:

$$\sigma^{LO} = \int_m d\sigma^B. \tag{4.2}$$

Here m is the number of partons in the final state and all quantities are calculated in $d = 4 - 2\epsilon$ dimensions. However, at this level the phase space integration in equation 4.2 is finite and the calculation can be carried out in four dimensions.

On the other hand, in the NLO cross section we have to consider real and virtual contributions with $m + 1$ and m partons in the final state respectively:

$$\sigma^{NLO} = \int_{m+1} d\sigma^R + \int_m d\sigma^V. \tag{4.3}$$

Both integrals on the right hand side are divergent for $d = 4$, but their sum should of course be finite. For this reason, before any numerical calculation can be carried out, the separate pieces have to be regularized. Using dimensional regularization, the divergences are replaced by double (soft and collinear) and single (soft, collinear and ultraviolet) poles. After carrying out the renormalization procedure for the virtual corrections, all the ultraviolet singularities should cancel and we have only soft and collinear divergences left.

The idea of the subtraction method is to use the identity

$$d\sigma^{NLO} = d\sigma^R - d\sigma^A + d\sigma^A + d\sigma^V\,, \tag{4.4}$$

where the approximated cross section $d\sigma^A$ is such that is has the same singular behaviour in d dimensions as $d\sigma^R$. In this way, $d\sigma^A$ acts effectively as a counter term for $d\sigma^R$ and introducing the phase space integration,

$$\sigma^{NLO} = \int_{m+1} (d\sigma^R - d\sigma^A) + \int_{m+1} d\sigma^A + \int_m d\sigma^V\,, \tag{4.5}$$

we can safely perform the limit $\epsilon \longrightarrow 0$ under the integral sign in the first term on the right-hand side of equation 4.5 and therefore, perform the integral in four dimensions. All the remaining singularities are at this point associated with the last two terms in equation 4.5. If we could integrate $d\sigma^A$ analytically over the one parton subspace leading to the ϵ poles, we could combine these poles with the ones coming from the virtual corrections and in this way, cancel all the singularities. Then we could perform the limit $\epsilon \longrightarrow 0$ and integrate numerically the rest over the m-parton phase space. The final structure of the calculation would be

$$\sigma^{NLO} = \int_{m+1} \left[\left(d\sigma^R\right)_{\epsilon=0} - \left(d\sigma^A\right)_{\epsilon=0} \right] + \int_m \left[d\sigma^V + \int_1 d\sigma^A \right]_{\epsilon=0}\,, \tag{4.6}$$

and could be easily implemented in a Monte Carlo program, which generates appropriately weighted partonic events with $m+1$ final state partons and events with m partons. This is then, the main idea behind the subtraction method and as can be seen from the equations mentioned above, the calculation of $d\sigma^A$ is the key ingredient to this method. Here we will use the formalism developed in [18], in which $d\sigma^A$ is calculated independently of the process in which one is interested.

In the case of single hadron production in DIS, one has to deal with identified hadrons in the initial and final states, which introduces a few complications in the calculation of $d\sigma^A$. In the case of no identified hadrons, the real cross section is singular whenever a pair of the $m+1$ final state partons become collinear. In the case we are interested in, this remains true but additionally, the cross section will be singular in the region where one of the partons becomes collinear to an identified parton. The approximate cross section $d\sigma^A$ should then, act as a local counter term also in these new regions and its integral $\int_1 d\sigma^A$ should still be computable analytically. With this in mind, the approximated cross section is written as

$$d\sigma^A = \sum_{\text{dipoles}} d\sigma^B \times \left(dV_{\text{dipole}} + dV'_{\text{dipole}} \right)\,, \tag{4.7}$$

where $d\sigma^B$ denotes the Born level cross section and the dipole factors dV_{dipole} that match the singular behaviour of $d\sigma^R$, are universal. The dipoles dV' match the singularities of $d\sigma^R$ coming from the region collinear to the momenta of the identified partons.

There are many dipole terms on the right-hand side of equation 4.7. Each of them corresponds to a different kinematic configuration of $m+1$ partons. Each configuration can be thought as obtained by an effective two-step process: an m parton configuration is first produced and then one of these partons decays into two partons [18]. It is this two-step pseudo-process that leads to the factorized structure on the right-hand side of equation 4.7. Furthermore, the product structure in $d\sigma^A$ allows a factorizable mapping from the $m+1$-parton phase space to an m-parton subspace times a single-parton phase-space, the one identified by the dipole partonic variables in dV_{dipole}. This mapping makes dV_{dipole} fully integrable analytically. We have then:

$$\int_{m+1} d\sigma^A = \sum_{dipoles} \int_m d\sigma^B \times \int_1 dV_{\text{dipole}} = \int_m d\sigma^B \times \mathbf{I}, \tag{4.8}$$

where the universal factor $\mathbf{I}$ is defined by

$$\mathbf{I} = \sum_{\text{dipole}} \int_1 dV_{\text{dipole}}, \tag{4.9}$$

and contains all the ϵ poles that are necessary to cancel the poles in $d\sigma^V$. Additionally, we obtain terms coming from the integration of dV'_{dipole}. The singularities coming from this are reabsorbed into the non-perturbative distribution functions and we are left with finite terms proportional to $d\sigma^B$, similar to the factor $\mathbf{I}$ but finite for $\epsilon \to 0$. In this way, our NLO cross section takes the form

$$\begin{aligned}\sigma^{NLO} &= \int_{m+1} \left[\left(d\sigma^R\right)_{\epsilon=0} - \left(\sum_{dipoles} d\sigma^B \times \left(dV_{\text{dipole}} + dV'_{\text{dipole}}\right)_{\epsilon=0} \right) \right] \\ &+ \int_m \left[d\sigma^V + d\sigma^B \times \mathbf{I}\right]_{\epsilon=0} + \int_0^1 dx \int_m \left[d\sigma^B(xp) \times (\mathbf{P}+\mathbf{K}+\mathbf{H})(x)\right]_{\epsilon=0}, \end{aligned} \tag{4.10}$$

where p denotes the functional dependence on the momenta of the identified partons. The last term on the right-hand side of equation 4.10 is the finite remainder left after the factorization of the initial- and final-state collinear singularities into parton densities and fragmentation functions. This term involves m-parton kinematics and an additional one-dimensional integration with respect to the longitudinal momentum fraction x. This integral arises from the convolution of the Born-type cross section with x dependent functions $\mathbf{P}$,$\mathbf{K}$ and $\mathbf{H}$, that are similar to the factor $\mathbf{I}$ but finite for $\epsilon = 0$. These functions are universal, and only depend on the number of identified partons. The functions $\mathbf{P}$ depend on the factorization scale for initial- and final-state partons, while the initial-state insertion operator $\mathbf{K}$ and the final-state insertion operator $\mathbf{H}$,depend on the factorization scheme. They will be discussed in detail in a later section of this chapter.

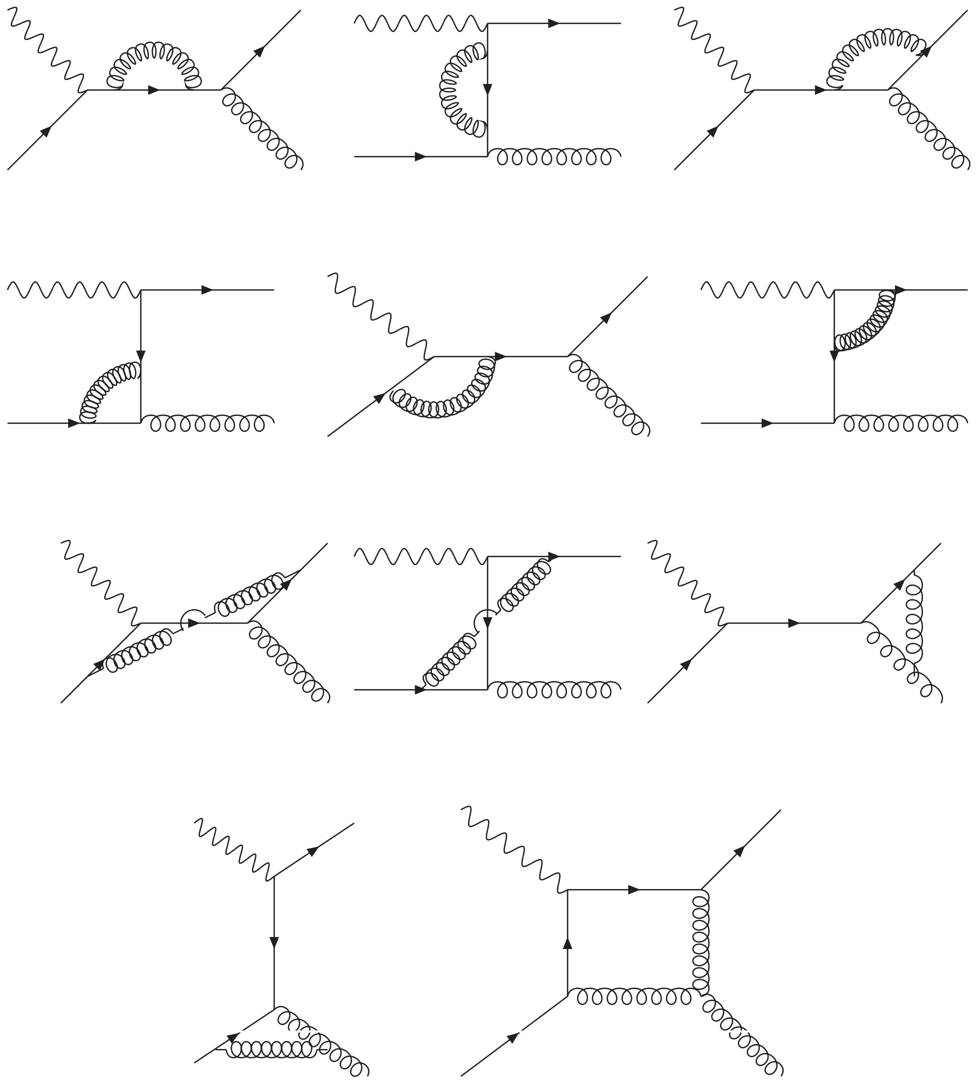

Figure 4.1: Virtual corrections to second order in α_s.

4.2 Virtual Corrections

Using the formalism described in the previous section, we can now proceed with the calculation. First, we calculate the virtual corrections from the diagrams showed in figure 4.1. Here we will encounter one loop integrals that have to be integrated in D dimensions to be regularized (dimensional regularization). The handling of these integrals was done following the formalism described in [50].

One loop integrals in D dimension are classified according to N, the number of propagators in the denominator and P, the number of integration momenta in the numerator. For $P + D - 2N \geq 0$ these integrals are UV-divergent. After dimensional regularization has been carried out, the UV-divergences drop out in renormalized quantities.

A general one-loop tensor integral can be defined as [50]

$$T^N_{\mu_1\ldots\mu_P}(p_1,\ldots,p_{N-1},m_0,\ldots,m_{N-1}) = \frac{(2\pi\mu)^{4-D}}{i\pi^2}\int d^Dq\frac{q_{\mu_1}\cdots q_{\mu_P}}{D_0D_1\cdots D_{N-1}}, \tag{4.11}$$

with the denominator factors,

$$D_0 = q^2 - m_0^2 + i\varepsilon, \qquad D_i = (q+p_i)^2 - m_i^2 + i\varepsilon, \qquad i = 1,\ldots,N-1, \tag{4.12}$$

originating from the propagators in the feynman diagram.

Usually, T^N is denoted by the Nth letter of the alphabet, i.e. $T^1 = A, T^2 = B, \ldots$, and the scalar integrals carry an index 0.

Since the integrals are Lorentz covariant, we can decompose them into tensors constructed from the external momenta p_i, and the metric tensor $g_{\mu\nu}$ with totally symmetric coefficient functions $T^N_{i_1\ldots i_P}$. We introduce an artificial momentum p_0 in order to write the terms containing $g_{\mu\nu}$ in a compact way

$$T^N_{\mu_1\ldots\mu_P}(p_1,\ldots,p_{N-1},m_0,\ldots,m_{N-1}) = \sum_{i_1,\ldots,i_P=0}^{N-1} T^N_{i_1\ldots i_P}p_{i_1\mu_1}\cdots p_{i_P\mu_P}. \tag{4.13}$$

From this expression we can recover the correct $g_{\mu\nu}$ terms by omitting all terms containing an odd number of p_0's and replacing products of even numbers of p_0's by the corresponding totally symmetric tensor constructed from the $g_{\mu\nu}$. The explicit Lorentz decompositions for the lowest order integrals read

$$\begin{aligned}
B_\mu &= p_{1\mu}B_1, && (4.14)\\
B_{\mu\nu} &= g_{\mu\nu}B_{00} + p_{1\mu}p_{1\nu}B_{11}, && (4.15)\\
C_\mu &= p_{1\mu}C_1 + p_{2\mu}C_2 = \sum_{i=1}^{2} p_{i\mu}C_i, && (4.16)\\
C_{\mu\nu} &= g_{\mu\nu}C_{00} + p_{1\mu}p_{1\nu}C_{11} + p_{2\mu}p_{2\nu}C_{22} + (p_{1\mu}p_{2\nu} + p_{2\mu}p_{1\nu})C_{12} &&\\
&= g_{\mu\nu}C_{00} + \sum_{i,j=1}^{2} p_{i\mu}p_{j\nu}C_{ij}, && (4.17)\\
C_{\mu\nu\rho} &= (g_{\mu\nu}p_{1\rho} + g_{\nu\rho}p_{1\mu} + g_{\mu\rho}p_{1\nu})C_{001} + (g_{\mu\nu}p_{2\rho} + g_{\nu\rho}p_{2\mu} + g_{\mu\rho}p_{2\nu})C_{002} &&\\
&\quad + p_{1\mu}p_{1\nu}p_{1\rho}C_{111} + p_{2\mu}p_{2\nu}p_{2\rho}C_{222} &&\\
&\quad + (p_{1\mu}p_{1\nu}p_{2\rho} + p_{1\mu}p_{2\nu}p_{1\rho} + p_{2\mu}p_{1\nu}p_{1\rho})C_{112} &&\\
&\quad + (p_{2\mu}p_{2\nu}p_{1\rho} + p_{2\mu}p_{1\nu}p_{2\rho} + p_{1\mu}p_{2\nu}p_{2\rho})C_{122} &&\\
&= \sum_{i=1}^{2}(g_{\mu\nu}p_{i\rho} + g_{\nu\rho}p_{i\mu} + g_{\mu\rho}p_{i\nu})C_{00i} + \sum_{i,j,k=1}^{2} p_{i\mu}p_{j\nu}p_{k\rho}C_{ijk}, && (4.18)
\end{aligned}$$

$$
\begin{aligned}
D_{\mu} &= \sum_{i=1}^{3} p_{i\mu} D_i, && (4.19)\\
D_{\mu\nu} &= g_{\mu\nu} D_{00} + \sum_{i,j=1}^{3} p_{i\mu} p_{j\nu} D_{ij}, && (4.20)\\
D_{\mu\nu\rho} &= \sum_{i=1}^{3} (g_{\mu\nu} p_{i\rho} + g_{\nu\rho} p_{i\mu} + g_{\mu\rho} p_{i\nu}) D_{00i} + \sum_{i,j,k=1}^{3} p_{i\mu} p_{j\nu} p_{k\rho} D_{ijk}, && (4.21)\\
D_{\mu\nu\rho\sigma} &= (g_{\mu\nu} g_{\rho\sigma} + g_{\mu\rho} g_{\nu\sigma} + g_{\mu\sigma} g_{\nu\rho}) D_{0000} \\
&\quad + \sum_{i,j=1}^{3} (g_{\mu\nu} p_{i\rho} p_{j\sigma} + g_{\nu\rho} p_{i\mu} p_{j\sigma} + g_{\mu\rho} p_{i\nu} p_{j\sigma} \\
&\qquad + g_{\mu\sigma} p_{i\nu} p_{j\rho} + g_{\nu\sigma} p_{i\mu} p_{j\rho} + g_{\rho\sigma} p_{i\mu} p_{j\nu}) D_{00ij} \\
&\quad + \sum_{i,j,k,l=1}^{3} p_{i\mu} p_{j\nu} p_{k\rho} p_{l\sigma} D_{ijkl}. && (4.22)
\end{aligned}
$$

Using the Lorentz decomposition of the tensor integrals (equation 4.13) the invariant functions $T^N_{i_1\ldots i_P}$ can be iteratively reduced to the scalar integrals T^N_0 [51]. The product of the integration momentum, q_μ, with an external momentum can be expressed in terms of the denominators,

$$
qp_k = \frac{1}{2}[D_k - D_0 - f_k], \qquad f_k = p_k^2 - m_k^2 + m_0^2. \tag{4.23}
$$

Multiplying (4.11) with p_k and substituting (4.23) yields

$$
\begin{aligned}
R^{N,k}_{\mu_1\ldots\mu_{P-1}} &= T^N_{\mu_1\ldots\mu_P} p_k^{\mu_P} \\
&= \frac{1}{2} \frac{(2\pi\mu)^{4-D}}{i\pi^2} \int d^D q \left[\frac{q_{\mu_1}\cdots q_{\mu_{P-1}}}{D_0 \ldots D_{k-1} D_{k+1} \ldots D_{N-1}} \right. \\
&\qquad \left. - \frac{q_{\mu_1}\cdots q_{\mu_{P-1}}}{D_1 \ldots D_{N-1}} - f_k \frac{q_{\mu_1}\cdots q_{\mu_{P-1}}}{D_0 \ldots D_{N-1}} \right] \\
&= \frac{1}{2} \left[T^{N-1}_{\mu_1\ldots\mu_{P-1}}(k) - T^{N-1}_{\mu_1\ldots\mu_{P-1}}(0) - f_k T^N_{\mu_1\ldots\mu_{P-1}} \right], && (4.24)
\end{aligned}
$$

where the argument k of the tensor integrals in the last line denotes that the propagator D_k was cancelled. Here $T^{N-1}_{\mu_1\ldots\mu_{P-1}}(0)$ has an external momentum in its first propagator and a shift of the integration momentum has to be performed in this integral in order to bring it to the form of equation 4.11. All integrals on the right-hand side of equation 4.24 have one Lorentz index less than the original tensor integral and in two of them one propagator is also eliminated.

For $P \geq 2$ we obtain one more relation by contracting equation 4.11 with the metric tensor and using

$$
g^{\mu\nu} q_\mu q_\nu = q^2 = D_0 + m_0^2. \tag{4.25}
$$

This gives

$$\begin{aligned} R^{N,00}_{\mu_1\ldots\mu_{P-2}} &= T^{N}_{\mu_1\ldots\mu_P} g^{\mu_{P-1}\mu_P} \\ &= \frac{(2\pi\mu)^{4-D}}{i\pi^2}\int d^Dq \left[\frac{q_{\mu_1}\ldots q_{\mu_{P-2}}}{D_1\ldots D_N} + m_0^2\frac{q_{\mu_1}\ldots q_{\mu_{P-2}}}{D_0\ldots D_N}\right] \\ &= \left[T^{N-1}_{\mu_1\ldots\mu_{P-2}}(0) + m_0^2 T^{N}_{\mu_1\ldots\mu_{P-2}}\right]. \end{aligned} \tag{4.26}$$

Inserting the Lorentz decomposition (equation 4.13) for the tensor integrals, T, into equation 4.24 and equation 4.26, we obtain a set of linear equations for the corresponding coefficient functions. Using this recursive reduction we are able to express all our tensor integrals in terms of the well known scalar integrals:

$$B_0(p_1) = \int d^dq \frac{1}{q^2(q-p_1)^2}, \tag{4.27}$$

$$C_0(p_1,p_2) = \int d^dq \frac{1}{q^2(q-p_1)^2(q-p_2)^2}, \tag{4.28}$$

$$D_0(p_1,p_2,p_3) = \int d^dq \frac{1}{q^2(q-p_1)^2(q-p_2)^2(q-p_3)^2}. \tag{4.29}$$

In our calculation all partons are considered massless and therefore, we do not need to include the masses in the integrals. The expressions for the massless scalar integrals can be found in [52, 53], but here we will use the more convenient form:

$$B_0(0) = 0, \tag{4.30}$$

$$B_0(p_1) = \frac{1}{\epsilon} + 2 - \ln\left(\frac{p_1^2}{\mu^2}\right), \tag{4.31}$$

$$\begin{aligned} C_0(p_1,p_2,p_1^2=0) &= \frac{1}{\epsilon^2}\frac{1}{2p_1p_2} + \frac{1}{\epsilon}\left(-\frac{1}{2p_1p_2}\right)\ln\left(\frac{2p_1p_2}{\mu^2}\right) \\ &\quad + \frac{1}{2p_1p_2}\zeta(2) + \frac{1}{4p_1p_2}\ln^2\left(\frac{2p_1p_2}{\mu^2}\right), \end{aligned} \tag{4.32}$$

$$\begin{aligned} C_0(p_1,p_2,p_1^1\neq 0) &= \frac{1}{\epsilon}\left(-\frac{1}{2p_1p_2}\right)\left[\ln\left(\frac{p_1^2}{\mu^2}\right) - \ln\left(\frac{p_1^2-2p_1p_2}{\mu^2}\right)\right] \\ &\quad + \frac{1}{4p_1p_2}\left[\ln^2\left(\frac{p_1^2}{\mu^2}\right) - \ln^2\left(\frac{p_1^2-2p_1p_2}{\mu^2}\right)\right], \end{aligned} \tag{4.33}$$

$$\begin{aligned} D_0(p_1,p_2,p_3) &= \frac{1}{\epsilon^2}\frac{1}{2p_1\cdot p_2 p_1\cdot p_3} \\ &\quad + \frac{1}{\epsilon}\frac{1}{2p_1\cdot p_2 p_1\cdot p_3}\left[\ln\left(\frac{2p_1\cdot p_2}{\mu^2}\right) + \ln\left(\frac{2p_1\cdot p_3}{\mu^2}\right) - \ln\left(\frac{-q^2}{\mu^2}\right)\right] \\ &\quad + \frac{1}{2p_1\cdot p_2 p_1\cdot p_3}\Bigg[R\left(\frac{2p_1\cdot p_2}{q^2},\frac{2p_1\cdot p_3}{q^2}\right) + \zeta(2) \\ &\quad + \frac{1}{2}\left(\ln^2\left(\frac{2p_1\cdot p_2}{\mu^2}\right) + \ln^2\left(\frac{2p_1\cdot p_3}{\mu^2}\right) - \ln^2\left(\frac{-q^2}{\mu^2}\right)\right)\Bigg], \end{aligned} \tag{4.34}$$

where $q = p_1 + p_2 + p_3$ and the function R is given by

$$R(x,y) = l(x)l(y) - l(x)l(1-x) - l(y)l(1-y) - S(x) - S(y) + \zeta(2). \tag{4.35}$$

The term $l(x)$ is the natural logarithm with an additional prescription for arguments in the interval $[-\infty, 0]$

$$l(x) = \lim_{\eta \to 0} \ln(x + \text{sgn}(q^2)\text{sgn}(1-x)i\eta), \tag{4.36}$$

and S is defined by

$$S = \lim_{\eta \to 0} \text{Li}_2(x + \text{sgn}(q^2)\text{sgn}(1-x)i\eta), \tag{4.37}$$

where Li_2 is the complex dilogarithm

$$\text{Li}_2 = -\int_0^z du \frac{\ln(1-u)}{u}. \tag{4.38}$$

Once the integrals have been reduced using this formalism, we need to include appropriate counter terms in order to cancel UV singularities (renormalization). Here the counter-term in equation 3.37 must be included so that equation 3.34 holds. Some $1/\epsilon^2$ and $1/\epsilon$ poles remain which are due to the IR singularities of the loop corrections. These poles will cancel when we include the insertion operator as shown in equation 4.10. Our analytic expressions for the virtual amplitudes have been found to agree with the expressions in Ref. [53] and the ones used in Ref. [54] for the case of virtual photon exchange, and with the amplitudes in Ref. [43] for the axial part in the weak current exchange. These comparisons were done analytically, by matching terms in the relevant expressions with the ones obtained here. The manipulation of traces and integral reduction was done using FORM [55], while the algebraic manipulation was done using *Mathematica*.

We also need to compute the insertion operator, which has the general form

$$\mathbf{I}(\{p\};\epsilon) = -\frac{\alpha_s}{2\pi}\frac{1}{\Gamma(1-\epsilon)}\sum_I \frac{1}{\mathbf{T}_I^2}\upsilon_I(\epsilon)\sum_{J\neq I}\mathbf{T}_I\cdot\mathbf{T}_J\left(\frac{4\pi\mu^2}{2p_I\cdot p_J}\right)^{\epsilon}, \tag{4.39}$$

where we have denoted $\{p\}$ a set of parton momenta and I and J indices that run over all these momenta. The matrices, $\mathbf{T_I}$, are the generators of the non-abelian Lie algebra in QCD as defined in equation 1.23. The universal singular function $\upsilon_I(\epsilon)$ depends only on the parton flavour and is given by

$$\upsilon_I(\epsilon) = \mathbf{T}_I^2\left(\frac{1}{\epsilon^2} - \frac{\pi^2}{3}\right) + \gamma_I\frac{1}{\epsilon} + K_I + O(\epsilon), \tag{4.40}$$

where

$$\gamma_q = \gamma_{\bar{q}} = \frac{3}{2}C_F \quad , \quad \gamma_g = \frac{11}{6}C_A - \frac{2}{3}T_R N_f, \tag{4.41}$$

$$K_q = K_{\bar{q}} = \left(\frac{7}{2} - \frac{\pi^2}{6}\right)C_F \quad , \quad K_g = \left(\frac{67}{18} - \frac{\pi^2}{6}\right)C_A - \frac{10}{9}T_R N_f. \tag{4.42}$$

In our case, the explicit form of the insertion operator is

$$\begin{aligned} I \;=\;& \frac{1}{8\pi^2}\Big[\frac{1}{\epsilon^2}(2C_f+N_c) - \frac{1}{6\epsilon}\Big(- 18C_f - 11N_c + 2n_f + 6(2Cf - N_c)\ln\left(\frac{2p_0\cdot p_h}{\mu^2}\right) \\ & +6N_c\ln\left(\frac{2p_0\cdot p_x}{\mu^2}\right) + 6N_c\ln\left(\frac{2p_h\cdot p_x}{\mu^2}\right)\Big) + \frac{1}{18}\Big(9(2C_f-N_c)\ln^2\left(\frac{2p_0\cdot p_h}{\mu^2}\right) \\ & +27(N_c-2C_f)\ln\left(\frac{2p_0\cdot p_h}{\mu^2}\right) + 9N_c\ln^2\left(\frac{2p_0\cdot p_x}{\mu^2}\right) + 9N_c\ln^2\left(\frac{2p_h\cdot p_x}{\mu^2}\right) + 247C_f \\ & +33N_c - 16n_f + (3n_f - 30N_c)\ln\left(\frac{2p_0\cdot p_x}{\mu^2}\right) - 30N_c\ln\left(\frac{2p_h\cdot p_x}{\mu^2}\right) + 3n_f\left(\frac{2p_h\cdot p_x}{\mu^2}\right) \\ & -27C_f\pi^2 - 9N_c\pi^2\Big) + O(\epsilon). \end{aligned} \tag{4.43}$$

We have now all the ingredients to calculate σ^{virt}:

$$\sigma^{\text{virt}} = \int_m \left[d\sigma^V + d\sigma^B \times \mathbf{I}\right]_{\epsilon=0}. \tag{4.44}$$

Finally, let us show explicitly some analytical results obtained for the axial part. The born terms are given in equations 3.41, and the insertion operator as it was given previously. We calculated the virtual amplitude $d\sigma^V$, and checked that equation 3.34 is fulfilled after including the counter-term in equation 3.37. The divergent parts in these amplitudes are:

$$\begin{aligned} d\sigma_A^{V,qq} \;=\;& \frac{1}{\epsilon^2}\left((2C_f+N_c)Q^2\frac{(2z-1)x^2+2(z-1)^2x-(z-2)z}{\pi^2x(1-x)(1-z)}\right) \\ & +\frac{1}{\epsilon}\frac{Q^2}{6\pi^2x(1-x)(1-z)}\Big[(-4xn_f+2n_f+6C_f(6x-5)+N_c(22x-17))z^2 \\ & +2(-2n_f(1-x)^2+6C_f((x-2)x+3)+N_c(5(x-2)x+11))z \\ & -(6C_f+5N_c-2n_f)(x-2)x+6((2z-1)x^2+2(1-z)^2x-(z-2)z) \\ & \left((N_c-2C_f)\ln\left(\frac{Q^2z}{\mu^2x}\right) - N_c\left(\ln\left(\frac{Q^2(1-x)}{\mu^2x}\right)+\ln\left(\frac{Q^2(1-z)}{\mu^2x}\right)\right)\right)\Big], \end{aligned} \tag{4.45}$$

$$\begin{aligned} d\sigma_A^{V,qg} \;=\;& \frac{1}{\epsilon^2}\left((2C_f+N_c)Q^2\frac{(2z-1)x^2-2z^2x+z^2-1}{\pi^2x(x-1)z}\right) \\ & +\frac{1}{\epsilon}\frac{Q^2}{6\pi^2x(1-x)z}\Big[(-4xn_f+2n_f+6C_f(6x-5)+N_c(22x-17))z^2 \\ & +2(-2n_fx^2+N_c(x(5x+12)-6))z+5N_c-2n_f+x(N_c(5x+12)-2n_fx) \\ & +6C_f(-2x(x+4)z+4z+x(x+4)+1)+6((2z-1)x^2-2z^2x+z^2-1) \\ & \left(N_c\ln\left(\frac{Q^2(1-x)}{\mu^2x}\right)+(2C_f-N_c)\ln\left(\frac{Q^2(1-z)}{\mu^2x}\right)+N_c\ln\left(\frac{Q^2z}{\mu^2x}\right)\right)\Big], \end{aligned} \tag{4.46}$$

$$\begin{aligned} d\sigma_A^{V,gq} \;=\;& \frac{1}{\epsilon^2}\left((2C_f+N_c)Q^2\frac{(2(x-1)x+1)(2z-1)}{\pi^2 x(z-1)z}\right) \\ &+\frac{1}{\epsilon}\frac{Q^2(1-2z)}{6\pi^2 x(1-z)z}\Big[-5N_c+2n_f+2(11N_c-2n_f)(1-x)x-6C_f(1-2(1-x)x) \\ &+6(1-2(1-x)x)\Big(N_c\left(\ln\left(\frac{Q^2(1-z)}{\mu^2 x}\right)+\ln\left(\frac{Q^2 z}{\mu^2 x}\right)\right) \\ &+(2C_f-N_c)\ln\left(\frac{Q^2(1-x)}{\mu^2 x}\right)\Big)\Big], \end{aligned} \tag{4.47}$$

where it can be checked that these terms cancel against the terms coming from the product of the insertion operator and the respective born terms.

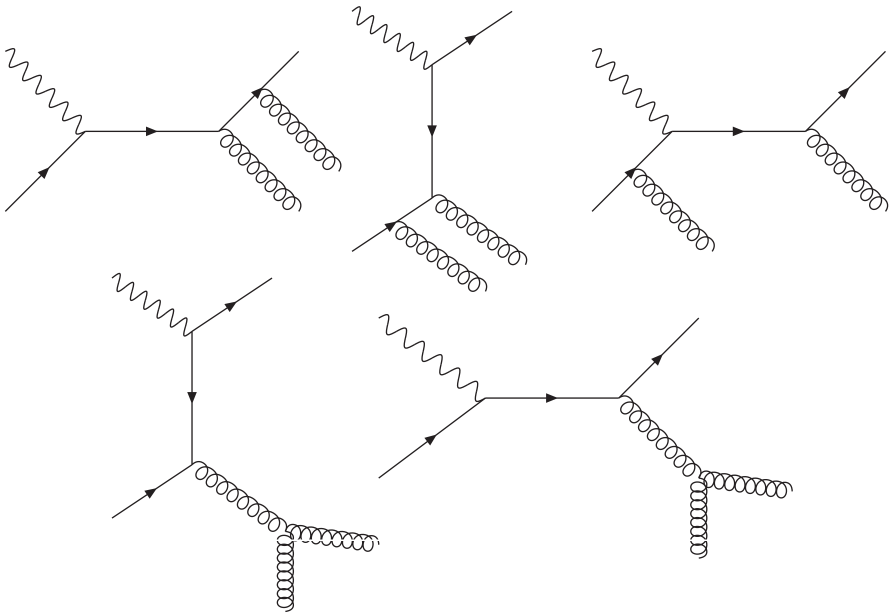

Figure 4.2: Real corrections with two radiated gluons in the final state.

4.3 Real Corrections

Next we have to calculate real corrections to the Born terms. We have 2 types of diagrams, those ones involving 2 quarks and 2 gluons, and those involving 4 quarks. In figure 4.2 we show the diagrams that contribute when we have an initial quark and 2 gluons radiated in the final state. The diagrams shown in figure 4.3 correspond to the case of an initial gluon and one gluon radiated in the final state. Here we also have to consider diagrams with crossed gluons, leading to 8 diagrams in each case. Amplitudes are the same for both types of diagram considering the different momenta involved. We also need to include the ghost diagrams shown in figure 4.4, which are included to facilitate the sum over polarizations.

In the diagrams in figure 4.5 we also have to consider the possible permutations corresponding to diagrams with crossed quarks, and also, the case in which all quarks are the same flavour, as well as the case when different flavours are allowed. In the case of charged current, we do not have the case of all quarks with the same flavour.

The calculation of these amplitudes can be carried out in 4-dimensions as was shown in equation 4.10. Our results have been compared analytically with the amplitudes used in [54] in the same way as we did for the virtual corrections, for the case of virtual photon exchange.

On the other hand, we need to calculate the approximated cross section $d\sigma^A$ as in equation 4.7. The starting point of the method described in [18] for constructing this counter-term is the observation that the singular behaviour of $|\mathcal{M}_{m+1}|^2$ is universal, it does not depend on the specific structure

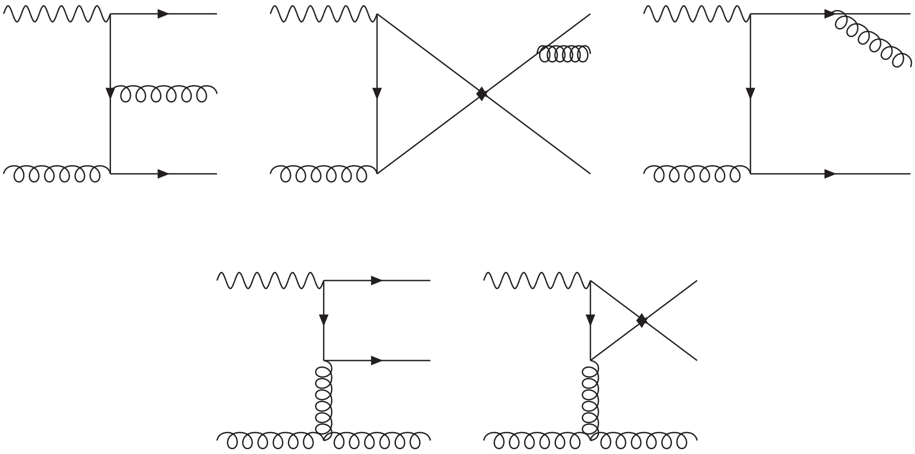

Figure 4.3: Real corrections with one initial gluon and one radiated gluon in the final state.

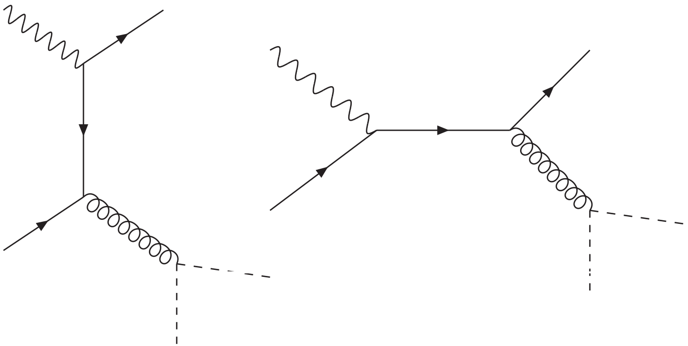

Figure 4.4: Ghost diagrams contributing to the real corrections in 4.2.

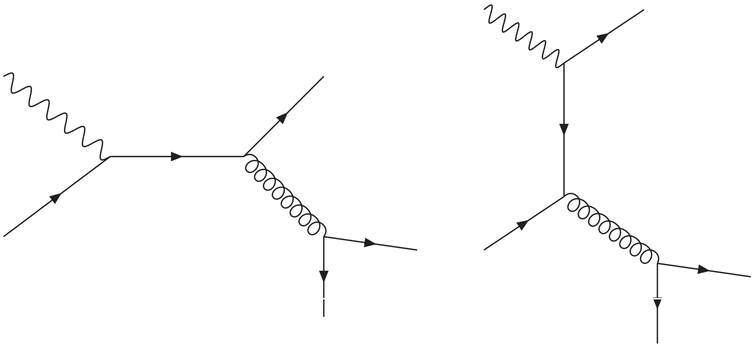

Figure 4.5: Real corrections involving 4 quarks.

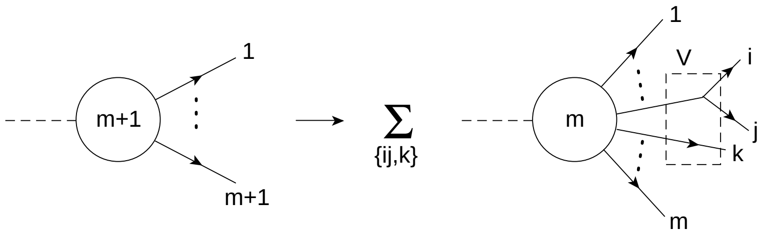

Figure 4.6: Pictorial representation of the dipole factorization procedure. When the partons i and j become soft and/or collinear, the singularities are factorized into the term $\mathbf{V}_{ij,k}$, which includes correlations with a single additional parton k.

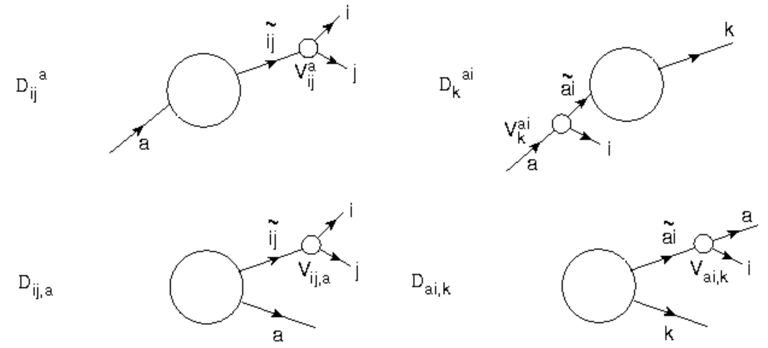

Figure 4.7: Effective diagrams for the different dipole formulae that we will need. The blobs represent the $m-$parton matrix element. Incoming and outgoing lines represent initial-state and final-state partons respectively.

of the amplitude itself. The origin of this is the fact that for its singular terms with respect to the momentum p_j, the tree amplitude $|\mathcal{M}_{m+1}|^2$ can always be considered as being obtained by the insertion of the parton j over all the possible external legs of a tree-level amplitude $|\mathcal{M}_m|^2$ with m QCD partons. Therefore, the singular behaviour of $|\mathcal{M}_{m+1}|^2$ is essentially factorizable with respect to $|\mathcal{M}_m|^2$ and the singular factor only depends on the momenta and quantum numbers of the QCD partons in $|\mathcal{M}_m|^2$. The factorization formulae have the symbolic structure

$$|\mathcal{M}_{m+1}|^2 \rightarrow |\mathcal{M}_m|^2 \otimes \mathbf{V}_{ij,k}, \tag{4.48}$$

where $\mathbf{V}_{ij,k}$ is the singular factor, which depends on the momenta and quantum numbers of the three partons i, j, k. Two of these partons (i and j) will play the role of *emitter* and the third parton k the role of *spectator*. Because of this structure the factorization formulae we use are called *dipole factorization formulae*. A pictorial representation of the factorization formulae is shown in figure 4.6.

The dipole factorization formulae have the property of avoiding double counting of overlapping soft and collinear singularities, which is possible because the dipole formulae fulfill exact momentum conservation. In [18], several versions of the factorization formulae are presented, that differ from one another in the implementation of momentum conservation away from the soft and collinear limits. Here we will only present the relevant formulae for our case. We will need 6 dipole contributions $\mathcal{D}$. In figure 4.7 we show the effective diagrams of the dipoles that we will need.

In the presence of initial state partons $a, ...$, the $m+1$-parton matrix element has both final-state ($p_i \cdot p_j \to 0$) and initial-state ($p_a \cdot p_j \to 0$) singularities. Let us consider first the case of final-state singularities. In this case, the final-state parton $\tilde{ij}$ is the emitter and the spectators are the initial-state partons $\tilde{a}, ...$ This contribution is given by

$$\mathcal{D}1^a_{ij} = -\frac{1}{2p_i \cdot p_j} \frac{1}{x_{ij,a}} \frac{\mathbf{T}_a \cdot \mathbf{T}_{ij}}{\mathbf{T}^2_{ij}} \mathbf{V}^a_{ij}, \tag{4.49}$$

where the momenta of the spectator $\tilde{a}$ and the emitter $\tilde{ij}$ are defined as

$$\tilde{p}^\mu_a = x_{ij,a} p^\mu_a, \qquad \tilde{p}^\mu_{ij} = p^\mu_i + p^\mu_j - (1 - x_{ij,a}) p^\mu_a, \tag{4.50}$$

$$x_{ij,a} = \frac{p_i p_a + p_j p_a - p_i p_j}{(p_i + p_j) p_a}. \tag{4.51}$$

The corresponding singular factors are:

$$\mathbf{V}^a_{q_i g_j} = 8\pi\alpha_s C_f \left[\frac{2}{1 - \tilde{z}_i + (1 - x_{ij,a})} - (1 - \tilde{z}_i) - \epsilon(1 - \tilde{z}_i) \right], \tag{4.52}$$

$$\begin{aligned} \mathbf{V}^a_{g_i g_j} = {} & 16\pi\alpha_s N_c \Big[-g^{\mu\nu} \left(\frac{1}{1 - \tilde{z}_i + (1 - x_{ij,a})} + \frac{1}{1 - \tilde{z}_j + (1 - x_{ij,a})} - 2 \right) \\ & + (1 - \epsilon) \frac{1}{p_i p_j} (\tilde{z}_i p^\mu_i - \tilde{z}_j p^\mu_j)(\tilde{z}_i p^\nu_i - \tilde{z}_j p^\nu_j) \Big], \end{aligned} \tag{4.53}$$

$$\mathbf{V}^a_{q_i \bar{q}_j} = 8\pi\alpha_s \frac{1}{2} \left[-g^{\mu\nu} - \frac{2}{p_i p_j} (\tilde{z}_i p^\mu_i - \tilde{z}_j p^\mu_j)(\tilde{z}_i p^\nu_i - \tilde{z}_j p^\nu_j) \right], \tag{4.54}$$

where

$$\tilde{z}_i = \frac{p_a p_i}{p_a p_i + p_a p_j}, \qquad \tilde{z}_j = \frac{p_a p_j}{p_a p_j + p_a p_i} = 1 - \tilde{z}_i. \tag{4.55}$$

In the case of initial-state singularities ($p_a \cdot p_i \to 0$), the emitter is the initial-state parton $\tilde{ai}$ and the spectator is the final-state parton k. These dipoles are given by

$$\mathcal{D}2^{ai}_k = -\frac{1}{2p_a \cdot p_i} \frac{1}{x_{ik,a}} \frac{\mathbf{T}_k \cdot \mathbf{T}_{ai}}{\mathbf{T}^2_{ai}} \mathbf{V}^{ai}_k. \tag{4.56}$$

The momenta of the spectator and the emitter are:

$$\tilde{p}^\mu_{ai} = x_{ik,a} p^\mu_a, \qquad \tilde{p}^\mu_k = p^\mu_k + p^\mu_i - (1 - x_{ik,a}) p^\mu_a, \tag{4.57}$$

$$x_{ik,a} = \frac{p_k p_a + p_i p_a - p_i p_k}{(p_k + p_i) p_a}. \tag{4.58}$$

The corresponding singular factors are:

$$\begin{aligned}
\mathbf{V}_k^{q_a g_i} &= 8\pi\alpha_s C_f \left[\frac{2}{1-x_{ik,a}+u_i)} - (1+x_{ik,a}) - \epsilon(1-x_{ik,a})\right], && (4.59)\\
\mathbf{V}_k^{g_a g_i} &= 16\pi\alpha_s N_c \Big[-g^{\mu\nu}\left(\frac{1}{1-x_{ik,a}+u_i} - 1 + x_{ik,a}(1-x_{ik,a})\right) \\
&\quad +(1-\epsilon)\frac{1-x_{ik,a}}{x_{ik,a}}\frac{u_i(1-u_i)}{p_i p_k}\left(\frac{p_i^\mu}{u_i} - \frac{p_k^\mu}{1-u_i}\right)\left(\frac{p_i^\nu}{u_i} - \frac{p_k^\nu}{1-u_i}\right)\Big], && (4.60)\\
\mathbf{V}_k^{q_a \bar{q}_i} &= 8\pi\alpha_s \frac{1}{2}\left[1-\epsilon-2x_{ik,a}(1-x_{ik,a})\right], && (4.61)\\
\mathbf{V}_k^{q_a q_i} &= 8\pi\alpha_s C_f \Big[-g^{\mu\nu}x_{ik,a} + \frac{1-x_{ik,a}}{x_{ik,a}}\frac{2u_i(1-u_i)}{p_i p_k}\left(\frac{p_i^\mu}{u_i} - \frac{p_k^\mu}{1-u_i}\right)\left(\frac{p_i^\nu}{u_i} - \frac{p_k^\nu}{1-u_i}\right)\Big], \\
& && (4.62)
\end{aligned}$$

where

$$u_i = \frac{p_a p_i}{p_a p_i + p_a p_k}. \tag{4.63}$$

Next, let us consider the case with identified partons in the final state. In the same way as before, we denote with a the parton with momentum p_a which is identified in the final state. In this case we can get singularities from the regions where $p_i \cdot p_j \to 0$ or $p_i \cdot p_a \to 0$. In the first region we have the dipoles:

$$\mathcal{D}3_{ij,a} = -\frac{1}{2p_i \cdot p_j}\frac{\mathbf{T}_a \cdot \mathbf{T}_{ij}}{\mathbf{T}_{ij}^2}\mathbf{V}_{ij,a}. \tag{4.64}$$

The dipole momenta are:

$$\tilde{p}_a^\mu = \frac{1}{z_{ij,a}}p_a^\mu, \qquad \tilde{p}_{ij}^\mu = p_i^\mu + p_j^\mu - \frac{1-z_{ij,a}}{z_{ij,a}}p_a^\mu, \tag{4.65}$$

$$z_{ij,a} = \frac{(p_i+p_j)p_a}{p_i p_a + p_j p_a + p_i p_j}. \tag{4.66}$$

The singular factors are in this case:

$$\begin{aligned}
\mathbf{V}_{q_i g_j,a} &= 8\pi\alpha_s C_f \left[\frac{2}{1-\tilde{z}_i z_{ij,a}} - (1+\tilde{z}_i) - \epsilon(1-\tilde{z}_i)\right], && (4.67)\\
\mathbf{V}_{g_i g_j,a} &= 16\pi\alpha_s N_c \Big[-g^{\mu\nu}\left(\frac{1}{1-\tilde{z}_i z_{ij,a}} + \frac{1}{1-\tilde{z}_j z_{ij,a}} - 2\right) \\
&\quad +(1-\epsilon)\frac{1}{p_i p_j}(\tilde{z}_i p_i^\mu - \tilde{z}_j p_j^\mu)(\tilde{z}_i p_i^\nu - \tilde{z}_j p_j^\nu)\Big], && (4.68)\\
\mathbf{V}_{q_i \bar{q}_j,a} &= 8\pi\alpha_s \frac{1}{2}\left[-g^{\mu\nu} - \frac{2}{p_i p_j}(\tilde{z}_i p_i^\mu - \tilde{z}_j p_j^\mu)(\tilde{z}_i p_i^\nu - \tilde{z}_j p_j^\nu)\right], && (4.69)
\end{aligned}$$

and $\tilde{z}_i$ is given by equation 4.55. In the region where $p_i \cdot p_a \to 0$ we have

$$\mathcal{D}4_{ai,k} = -\frac{1}{2p_a \cdot p_i}\frac{\mathbf{T}_k \cdot \mathbf{T}_{ai}}{\mathbf{T}_{ai}^2}\mathbf{V}_{ai,k}. \tag{4.70}$$

The parton momenta in the dipole are:

$$\tilde{p}_{ai}^\mu = \frac{1}{z_{ik,a}}p_a^\mu, \qquad \tilde{p}_k^\mu = p_i^\mu + p_k^\mu - \frac{1-z_{ik,a}}{z_{ik,a}}p_a^\mu, \tag{4.71}$$

$$z_{ik,a} = \frac{(p_k+p_i)p_a}{p_k p_a + p_i p_a + p_i p_k}. \tag{4.72}$$

The singular factors are given by:

$$\begin{aligned}
\mathbf{V}_{q_ag_i,k} &= 8\pi\alpha_s C_f\left[\frac{2}{1-z_{ik,a}(1-u_i)}-(1+z_{ik,a})-\epsilon(1-z_{ik,a})\right], && (4.73)\\
\mathbf{V}_{g_ag_i,k} &= 16\pi\alpha_s N_c\Big[-g^{\mu\nu}\left(\frac{1}{1-z_{ik,a}(1-u_i)}-2+\frac{1}{z_{ik,a}}\right)\\
&\quad +(1-\epsilon)(1-z_{ik,a})z_{ik,a}\frac{u_i(1-u_i)}{p_ip_k}\left(\frac{p_i^\mu}{u_i}-\frac{p_k^\mu}{1-u_i}\right)\left(\frac{p_i^\nu}{u_i}-\frac{p_k^\nu}{1-u_i}\right)\Big], && (4.74)\\
\mathbf{V}_{q_a\bar{q}_i,k} &= 8\pi\alpha_s\frac{1}{2}\left[-g^{\mu\nu}-2z_{ik,a}(1-z_{ik,a})\frac{u_i(1-u_i)}{p_ip_k}\left(\frac{p_i^\mu}{u_i}-\frac{p_k^\mu}{1-u_i}\right)\left(\frac{p_i^\nu}{u_i}-\frac{p_k^\nu}{1-u_i}\right)\right], && (4.75)\\
\mathbf{V}_{g_a\bar{q}_i,k} &= 8\pi\alpha_s C_f\left[\frac{1+(1-z_{ik,a})^2}{z_{ik,a}}-\epsilon z_{ik,a}\right], && (4.76)
\end{aligned}$$

where u_i is the same as in equation 4.63.

Finally, we consider the case of identified partons in both the initial and the final states. In this case, it is convenient to introduce new dipoles $\mathcal{D}_b^{(n)ai}$ and $\mathcal{D}_{ai,b}^{(n)}$ in which the momentum of the spectator is left unchanged. These objects are pseudo-dipoles rather than dipoles, in the sense that they depend on the momentum $\tilde{p}_{ai}$ of the emitter, on the momentum p_b of the spectator and on an additional momentum n:

$$n^\mu = p_{\text{in}}^\mu - \sum_{b\in\text{final-state}} p_b^\mu, \qquad (4.77)$$

where p_{in}^μ is the total incoming momentum and the second term on the right hand side is the sum of all momenta of the identified partons in the final state. Let us consider first the case of $p_i\cdot p_a\to 0$ when a is an initial-state parton. The dipole terms are in this case

$$\mathcal{D}5_b^{(n)ai} = -\frac{1}{2p_a\cdot p_i}\frac{1}{x_{ain}}\frac{\mathbf{T}_b\cdot\mathbf{T}_{ai}}{\mathbf{T}_{ai}^2}\mathbf{V}_b^{(n)ai}, \qquad (4.78)$$

with

$$\begin{aligned}
\tilde{p}_{ai}^\mu &= x_{ain}p_a^\mu, && (4.79)\\
x_{ain} &= \frac{(p_a-p_i)\cdot n}{p_a\cdot n}, && (4.80)
\end{aligned}$$

which corresponds to equation 5.159 in Ref. [18]. Here the singular factors are:

$$\begin{aligned}
\mathbf{V}_b^{(n)q_ag_i} &= 8\pi\alpha_s C_f\left[2v_{i,ab}-(1+x_{ain})-\epsilon(1-x_{ain})\right], && (4.81)\\
\mathbf{V}_b^{(n)g_agi} &= 16\pi\alpha_s N_c\Big[-g^{\mu\nu}\left(v_{i,ab}-1+x_{ain}(1-x_{ain})\right)\\
&\quad +(1-\epsilon)\frac{1-x_{ain}}{x_{ain}}\frac{2p_i\cdot p_a}{2(p_a\cdot n)(p_i\cdot n)-n^2p_i\cdot p_a}\left(\frac{np_a}{p_ip_a}p_i^\mu-n^\mu\right)\left(\frac{np_a}{p_ip_a}p_i^\nu-n^\nu\right)\Big], && (4.82)\\
\mathbf{V}_b^{g_a\bar{q}_i} &= 8\pi\alpha_s\frac{1}{2}\left[1-\epsilon-2x_{ain}(1-x_{ain})\right], && (4.83)\\
\mathbf{V}_b^{(n)q_aqi} &= 8\pi\alpha_s C_f\Big[-g^{\mu\nu}x_{ain}\\
&\quad +\frac{1-x_{ain}}{x_{ain}}\frac{4p_i\cdot p_a}{2(p_a\cdot n)(p_i\cdot n)-n^2p_i\cdot p_a}\left(\frac{np_a}{p_ip_a}p_i^\mu-n^\mu\right)\left(\frac{np_a}{p_ip_a}p_i^\nu-n^\nu\right)\Big], && (4.84)
\end{aligned}$$

with

$$v_{i,ab} = \frac{p_a p_b}{p_i(p_a + p_b)}. \tag{4.85}$$

Finally, when a is an identified parton in the final state, we have

$$\mathcal{D}6^{(n)}_{ai,b} = -\frac{1}{2p_a \cdot p_i} \frac{\mathbf{T}_b \cdot \mathbf{T}_{ai}}{\mathbf{T}^2_{ai}} \mathbf{V}^{(n)}_{ai,b}, \tag{4.86}$$

with

$$\begin{aligned} \tilde{p}^{\mu}_{ai} &= \frac{1}{z_{ain}} p^{\mu}_a, && (4.87) \\ z_{ain} &= \frac{p_a \cdot n}{(p_a + p_i) \cdot n}. && (4.88) \end{aligned}$$

This last dipole corresponds to equation 5.180 in Ref. [18]. Furthermore,

$$\begin{aligned} \mathbf{V}^{(n)}_{q_a g_i, b} &= 8\pi\alpha_s C_f \left[2\frac{v_{i,ab}}{z_{ain}} - (1 + z_{ain}) - \epsilon(1 - z_{ain}) \right], && (4.89) \\ \mathbf{V}^{(n)}_{g_a g_i, b} &= 16\pi\alpha_s N_c \Big[-g^{\mu\nu} \left(\frac{v_{i,ab}}{z_a in} - 1 + \frac{1 - z_{ain}}{z_{ain}} \right) \\ &\quad +2(1-\epsilon) z_{ain}(1 - z_{ain}) \frac{p_i \cdot p_a}{2(p_a \cdot n)(p_i \cdot n) - n^2 p_i \cdot p_a} \left(\frac{np_a}{p_i p_a} p^{\mu}_i - n^{\mu} \right) \left(\frac{np_a}{p_i p_a} p^{\nu}_i - n^{\nu} \right) \Big], \\ & && (4.90) \\ \mathbf{V}^{(n)}_{g_a \bar{q}_i, b} &= 8\pi\alpha_s C_f \left[\frac{1 + (1 - z_{ain})^2}{z_{ain}} - \epsilon z_{ain} \right], && (4.91) \\ \mathbf{V}^{(n)}_{q_a \bar{q}_i, b} &= 8\pi\alpha_s \frac{1}{2} \Big[-g^{\mu\nu} \\ &\quad -4 z_{ain}(1 - z_{ain}) \frac{p_i \cdot p_a}{2(p_a \cdot n)(p_i \cdot n) - n^2 p_i \cdot p_a} \left(\frac{np_a}{p_i p_a} p^{\mu}_i - n^{\mu} \right) \left(\frac{np_a}{p_i p_a} p^{\nu}_i - n^{\nu} \right) \Big]. && (4.92) \end{aligned}$$

In total, we have 18 processes that contribute to the real correction for neutral current DIS, coming from the different possibilities allowed by the diagrams in figures 4.2, 4.3 and 4.5. In the same way, we have 9 processes for the case of charged current DIS. In tables 4.1 and 4.2 we present a list of all these processes, together with their respective dipole contributions. There we denote up-type quarks by u and down-type quarks by d, and we present the relevant processes for the case where W^+ is the exchanged vector boson in the charged current table.

Diagram	Hadronization	Dipole Contributions
$q \to qgg$	1. $q \to q$	$\mathcal{D}1^{q}_{gg} + \mathcal{D}2^{qg}_{g} + \mathcal{D}3_{gg,q} + \mathcal{D}4_{qg,q} + \mathcal{D}5^{qg}_{q} + \mathcal{D}6_{qg,q}$
	2. $q \to g$	$\mathcal{D}1^{q}_{qg} + \mathcal{D}2^{qg}_{q} + \mathcal{D}3_{qg,g} + \mathcal{D}4_{gq,g} + \mathcal{D}4_{gg,q} + \mathcal{D}5^{qg}_{g} + \mathcal{D}6_{gq,q} + \mathcal{D}6_{gg,q}$
$g \to qg\bar{q}$	3. $g \to q$	$\mathcal{D}1^{g}_{qg} + \mathcal{D}2^{gq}_{g} + \mathcal{D}2^{gg}_{q} + \mathcal{D}3_{qg,q} + \mathcal{D}4_{qg,q} + \mathcal{D}5^{gq}_{q} + \mathcal{D}5^{gg}_{q} + \mathcal{D}6_{qg,g}$
	4. $g \to g$	$\mathcal{D}2^{gq}_{q} + \mathcal{D}4_{gq,q} + \mathcal{D}5^{gq}_{g} + \mathcal{D}6_{gq,g}$
$q \to qq\bar{q}$	5. $q \to q$	$\mathcal{D}1^{q}_{qq} + \mathcal{D}2^{qq}_{q} + \mathcal{D}3_{qq,q} + \mathcal{D}4_{qq,q} + \mathcal{D}5^{qq}_{q} + \mathcal{D}6_{qq,q}$
	6. $q \to \bar{q}$	$\mathcal{D}2^{qq}_{q} + \mathcal{D}4_{qq,q} + \mathcal{D}5^{qq}_{q} + \mathcal{D}6_{qq,q}$
$q \to qq'\bar{q}'$	7. $u \to uu'\bar{u}'$	$\mathcal{D}1^{q}_{qq} + \mathcal{D}3_{qq,q}$
	8. $u \to ud'\bar{d}'$	
	9. $d \to du'\bar{u}'$	
	10. $d \to dd'\bar{d}'$	
$q \to \bar{q}'qq'$	11. $u \to \bar{d}'ud'$	$\mathcal{D}2^{qq}_{q} + \mathcal{D}4_{qq,q} + \mathcal{D}5^{qq}_{q} + \mathcal{D}6_{qq,q}$
	12. $d \to \bar{u}'du'$	
	13. $u \to \bar{u}'uu'$	
	14. $d \to \bar{d}'dd'$	
$q \to q'q\bar{q}'$	15. $u \to d'u\bar{d}'$	$\mathcal{D}2^{qq}_{q} + \mathcal{D}4_{qq,q} + \mathcal{D}5^{qq}_{q} + \mathcal{D}6_{qq,q}$
	16. $d \to u'd\bar{u}'$	
	17. $u \to u'u\bar{u}'$	
	18. $d \to d'd\bar{d}'$	

Table 4.1: List of processes that contribute to the real corrections for neutral current DIS at $O(\alpha^2)$.

Diagram	Hadronization	Dipole Contributions
$d \to ugg$	1. $d \to u$	$\mathcal{D}1^{q}_{gg} + \mathcal{D}2^{qg}_{g} + \mathcal{D}3_{gg,q} + \mathcal{D}4_{qg,q} + \mathcal{D}5^{qg}_{q} + \mathcal{D}6_{qg,q}$
	2. $d \to g$	$\mathcal{D}1^{q}_{qg} + \mathcal{D}2^{qg}_{q} + \mathcal{D}3_{qg,g} + \mathcal{D}4_{gq,g} + \mathcal{D}4_{gg,q} + \mathcal{D}5^{qg}_{g} + \mathcal{D}6_{gq,q} + \mathcal{D}6_{gg,q}$
$g \to qg\bar{q}$	3. $g \to q$	$\mathcal{D}1^{g}_{qg} + \mathcal{D}2^{gq}_{g} + \mathcal{D}2^{gg}_{q} + \mathcal{D}3_{qg,q} + \mathcal{D}4_{qg,q} + \mathcal{D}5^{gq}_{q} + \mathcal{D}5^{gg}_{q} + \mathcal{D}6_{qg,g}$
	4. $g \to g$	$\mathcal{D}2^{gq}_{q} + \mathcal{D}4_{gq,q} + \mathcal{D}5^{gq}_{g} + \mathcal{D}6_{gq,g}$
$d \to uu\bar{u}$	5. $d \to u$	$\mathcal{D}3_{qq,q} + \mathcal{D}4_{qq,q}$
	6. $d \to \bar{u}$	$\mathcal{D}1^{q}_{qq} + \mathcal{D}2^{qq}_{q} + \mathcal{D}5^{qq}_{q} + \mathcal{D}6_{qq,q}$
$d \to ud\bar{d}$	7. $d \to u$	$\mathcal{D}3_{qq,q} + \mathcal{D}4_{qq,q}$
	8. $d \to \bar{d}$	$\mathcal{D}1^{q}_{qq} + \mathcal{D}2^{qq}_{q} + \mathcal{D}5^{qq}_{q} + \mathcal{D}6_{qq,q}$
	9. $d \to d$	$\mathcal{D}1^{q}_{qq} + \mathcal{D}2^{qq}_{q} + \mathcal{D}5^{qq}_{q} + \mathcal{D}6_{qq,q}$

Table 4.2: List of processes that contribute to the real corrections for charged current DIS at $O(\alpha^2)$.

4.4 Splitting Functions

The last element of the calculation is to compute the splitting functions $\mathbf{P}, \mathbf{K}, \mathbf{H}$. As mentioned in section 4.1, they are universal and only depend on the number of identified partons. For initial state partons we have:

$$\mathbf{P}^{a,b}(\{p\}; xp_a, x; \mu_F^2) = \frac{\alpha_s}{2\pi} P^{ab}(x) \frac{1}{\mathbf{T}_b^2} \sum_{I \neq b} \mathbf{T}_I \cdot \mathbf{T}_b \ln \frac{\mu_F}{2xp_a \cdot p_I}, \tag{4.93}$$

and for final state partons:

$$\mathbf{P}_{b,a}(\{p\}; p_a/z, z; \mu_F^2) = \frac{\alpha_s}{2\pi} P_{ba}(z) \frac{1}{\mathbf{T}_b^2} \sum_{I \neq b} \mathbf{T}_I \cdot \mathbf{T}_b \ln \frac{z\mu_F}{2p_a \cdot p_I}. \tag{4.94}$$

Here $P^{ab} = P_{ab}$ are the Altarelli-Parisi splitting functions in equations 2.33. Furthermore, we have the functions $\mathbf{K}$ and $\mathbf{H}$. In the general case of multi-parton interactions, they are given by

$$\begin{aligned}
\mathbf{K}^{a,a'}(x) &= \frac{\alpha_s}{2\pi} \Big\{ \bar{K}^{aa'}(x) - K^{aa'}_{\mathrm{F.S.}}(x) \\
&+ \delta^{aa'} \sum_i \mathbf{T}_i \cdot \mathbf{T}_a \frac{\gamma_i}{\mathbf{T}_i^2} \left[\left(\frac{1}{1-x} \right)_+ + \delta(1-x) \right] - \frac{1}{\mathbf{T}_{a'}^2} \left(\sum_{l=1}^{n} \mathbf{T}_{a_l} \cdot \mathbf{T}_{a'} + \mathbf{T}_b \cdot \mathbf{T}_{a'} \right) \tilde{K}^{aa'}(x) \\
&- \frac{1}{\mathbf{T}_{a'}^2} \left[\sum_{l=1}^{n} \mathbf{T}_{a_l} \cdot \mathbf{T}_{a'} \mathcal{L}^{a,a'}(x; p, q_l, n) + \mathbf{T}_b \cdot \mathbf{T}_{a'} \mathcal{L}^{a,a'}(x; p, \bar{p}, n) \right] \Big\},
\end{aligned} \tag{4.95}$$

$$\begin{aligned}
\mathbf{H}_{a'_l,a_l}(z) &= \frac{\alpha_s}{2\pi} \Big\{ \bar{K}^{a'_l a_l}(z) + 3P_{a'_l a_l} \ln z - H^{\mathrm{F.S.}}_{a'_l a_l}(z) + \delta_{a'_l a_l} \sum_i \mathbf{T}_i \cdot \mathbf{T}_{a'_l} \frac{\gamma_i}{\mathbf{T}_i^2} \left[\left(\frac{1}{1-z} \right)_+ + \delta(1-z) - 1 \right] \\
&+ \frac{1}{\mathbf{T}_{a'_l}^2} \left(\sum_{r=1, r\neq l}^{n} \mathbf{T}_{a_r} \cdot \mathbf{T}_{a'_l} + \mathbf{T}_a \cdot \mathbf{T}_{a'_l} + \mathbf{T}_b \cdot \mathbf{T}_{a'_l} \right) \left[P_{a'_l a_l}(z) \ln z - \tilde{K}^{a'_l a_l}(z) \right] \\
&- \frac{1}{\mathbf{T}_{a'_l}^2} \Big[\sum_{r=1, r\neq l}^{n} \mathbf{T}_{a_r} \cdot \mathbf{T}_{a'_l, a_l} \mathcal{L}^{a'_l, a_l}(z; q_l, q_r, n) + \mathbf{T}_a \cdot \mathbf{T}_{a'_l} \mathcal{L}^{a'_l, a_l}(z; q_l, p, n) \\
&+ \mathbf{T}_b \cdot \mathbf{T}_{a'_l} \mathcal{L}^{a'_l, a_l}(z; q_l, \bar{p}, n) \Big] \Big\},
\end{aligned} \tag{4.96}$$

where

$$\bar{K}^{ab} = P'_{ab}(x) + P^{ab}(x) \ln \frac{1-x}{x} + \delta^{ab} \left[\mathbf{T}_a^2 \left[\frac{2}{1-x} \ln \frac{1-x}{x} \right]_+ - \delta(1-x) \left(\gamma_a + K_a - \frac{5}{6} \pi^2 \mathbf{T}_a^2 \right) \right]. \tag{4.97}$$

The functions P'_{ab} denote the part of the splitting functions proportional to ϵ and the functions K_a and γ_a are the same as in equations 4.41 and 4.42. Furthermore, the expressions above depend on the scheme dependent flavour functions $K^{ab}_{\mathrm{F.S.}}(x)$ and $H^{\mathrm{F.S.}}_{ba}(x)$, that are zero in the $\overline{\mathrm{MS}}$ scheme that we are using. Finally, the functions $\tilde{K}$ and $\mathcal{L}^{ab}$ are given by

$$\tilde{K}^{ab}(x) = P^{ab}(x) \ln(1-x) + \delta^{ab} \mathbf{T}_a^2 \left[\left[\frac{2}{1-x} \ln(1-x) \right]_+ - \frac{\pi^2}{3} \delta(1-x) \right], \tag{4.98}$$

$$\begin{aligned}\mathcal{L}^{ab}(x;p_a,p_b,n) &= \delta^{ab}\delta(1-x)2\mathbf{T}_a^2\Big[\mathrm{Li}_2\left[1-\frac{(1+v)}{2}\frac{(p_a+p_b)\cdot n}{p_a\cdot n}\right] \\ &\quad +\mathrm{Li}_2\left[1-\frac{(1-v)}{2}\frac{(p_a+p_b)\cdot n}{p_a\cdot n}\right]\Big]-P^{ab}(x)\ln\frac{n^2(p_a\cdot p_b)}{2(p_a\cdot n)^2}, \qquad (4.99)\end{aligned}$$

with

$$v = \sqrt{1-\frac{n^2(p_a+p_b)^2}{[(p_a+p_b)\cdot n]^2}}, \qquad (4.100)$$

$$n^\mu = p_{\mathrm{in}}^\mu - \sum_{a\in\text{final-state}} p_a^\mu, \qquad (4.101)$$

where p_{in} is the total incoming momentum in the scattering process and the second term on the right hand side is the sum of all momenta of the identified partons in the final state.

Using these expressions we can now build our own splitting operators for the processes in which we are interested. In our case we have 6 possible processes for initial- and final-state partons:

$$q_0 \rightarrow q_h+g_x, P_{qq}, \qquad (4.102)$$

$$q_0 \rightarrow q_h+g_x, P_{gq}, \qquad (4.103)$$

$$q_0 \rightarrow q_x+g_h, P_{qq}, \qquad (4.104)$$

$$q_0 \rightarrow q_x+g_h, P_{qg}, \qquad (4.105)$$

$$g_0 \rightarrow q_h+\bar{q}_x, P_{gg}, \qquad (4.106)$$

$$g_0 \rightarrow q_h+\bar{q}_x, P_{qg}, \qquad (4.107)$$

where the low index 0 denotes the initial-state parton, h is the final-state parton, and x the remaining parton. The P_{ab} denote the splitting function considered in each case.

We will build our splitting operators $\mathbf{S^{ab}}$ for the six cases and for initial and final state partons. Their explicit form is given by

$$\begin{aligned}&\mathbf{S}^{gq}_{\mathrm{initial}}(\{p_h(q),p_x(g)\},p_0(g),x_D) \\ &= \mathbf{P}^{gq}(\{p_h(q),p_x(g)\},p_0(g),x_D)+\mathbf{K}^{gq}(\{p_h(q),p_x(g)\},p_0(g),x_D) \\ &= \alpha_s\Big\{\frac{N_c}{C_f 8\pi}\Big(-\ln(1-x_D)+2x_D\ln(1-x_D)-2x_D^2\ln(1-x_D)+\ln\left(\frac{2z}{1-z}\right) \\ &-2x_D\ln\left(\frac{2z}{1-z}\right)+2x_D^2\ln\left(\frac{2z}{1-z}\right)-\ln\left(\frac{x\mu^2}{Q^2x_D(1-z)}\right) \\ &+2x_D\ln\left(\frac{x\mu^2}{Q^2x_D(1-z)}\right)-2x_D^2\ln\left(\frac{x\mu^2}{Q^2x_D(1-z)}\right)+\ln\left(\frac{x\mu^2}{Q^2x_Dz}\right) \\ &-2x_D\ln\left(\frac{x\mu^2}{Q^2x_Dz}\right)+2x_D^2\ln\left(\frac{x\mu^2}{Q^2x_Dz}\right)\Big)+\frac{1}{4\pi}\Big(2(1-x_D)x_D+2(1-x_D)x_D\ln\left(\frac{x\mu^2}{Q^2x_Dz}\right) \\ &+(1-2x_D(1-x_D))\ln\left(\frac{1-x_D}{x_D}\right)-\ln\left(\frac{x\mu^2}{Q^2x_Dz}\right) \\ &+(1-2x_D(1-x_D))\ln(1-x_D)-(1-2x_D(1-x_D))\ln\left(\frac{2z}{1-z}\right)\Big)\Big\}, \qquad (4.108)\end{aligned}$$

$$
\begin{aligned}
&\mathbf{S}^{gq}_{\text{initial}}(\{p_x(q),p_h(g)\},p_0(g),x_D)\\
&\quad= \mathbf{P}^{gq}(\{p_x(q),p_h(g)\},p_0(g),x_D) + \mathbf{K}^{gq}(\{p_x(q),p_h(g)\},p_0(g),x_D)\\
&\quad= \alpha_s\Big\{\frac{N_c}{C_f 8\pi}\Big(\ln(1-x_D) - 2x_D\ln(1-x_D) + 2x_D^2\ln(1-x_D) - \ln\left(\frac{2z}{1-z}\right)\\
&\quad+2x_D\ln\left(\frac{2z}{1-z}\right) - 2x_D^2\ln\left(\frac{2z}{1-z}\right) + \ln\left(\frac{x\mu^2}{Q^2x_D(1-z)}\right)\\
&\quad-2x_D\ln\left(\frac{x\mu^2}{Q^2x_D(1-z)}\right) + 2x_D^2\ln\left(\frac{x\mu^2}{Q^2x_D(1-z)}\right) - \ln\left(\frac{x\mu^2}{Q^2x_Dz}\right)\\
&\quad+2x_D\ln\left(\frac{x\mu^2}{Q^2x_Dz}\right) - 2x_D^2\ln\left(\frac{x\mu^2}{Q^2x_Dz}\right)\Big) + \frac{1}{4\pi}\Big(2(1-x_D)x_D\\
&\quad+(1-2x_D(1-x_D))\ln\left(\frac{1-x_D}{x_D}\right)\\
&\quad+(2x_D(1-x_D)-1)\ln\left(\frac{x\mu^2}{Q^2x_D(1-z)}\right)\Big)\Big\},
\end{aligned}
\tag{4.109}
$$

$$
\begin{aligned}
&\mathbf{S}^{qq}_{\text{initial}}(\{p_h(q),p_x(g)\},p_0(q),x_D)\\
&\quad= \mathbf{P}^{qq}(\{p_h(q),p_x(g)\},p_0(q),x_D) + \mathbf{K}^{qq}(\{p_h(q),p_x(g)\},p_0(q),x_D)\\
&\quad= \alpha_s\Big\{\frac{n_f}{12\pi}\left(\delta(1-x_D) + \left[\frac{1}{1-x_D}\right]_+\right) + \frac{C_f}{24\pi}\Big(\delta(1-x_D)\Big[-60+8\pi^2\\
&\quad+24\mathrm{Li}_2\left[\frac{2-3z-x+\sqrt{x^2+2(-4+x)z+9z^2}}{2(1-z)}\right]\\
&\quad+24\mathrm{Li}_2\left[\frac{2-x-3z-\sqrt{x^2+2(-4+x)z+9z^2}}{2(1-z)}\right]\Big]\\
&\quad+6\Big(2-2x_D-2\ln\left(\frac{1-x_D}{x_D}\right) - 2x_D\ln\left(\frac{1-x_D}{x_D}\right) - 2\ln(1-x_D) - 2x_D\ln(1-x_D)\\
&\quad+2\ln\left(\frac{2}{1-z}\right) + 2x_D\ln\left(\frac{2}{1-z}\right) + 2\ln(z) + 2x_D\ln(z)\Big) - 12\ln\left(\frac{x\mu^2}{Q^2x_Dz}\right)\left[\frac{1+x_D^2}{1-x_D}\right]_+\\
&\quad+12\left[\frac{2\ln\left(-1+\frac{1}{x_D}\right)}{1-x_D}\right]_+ + 12\left[\frac{2\ln(1-x_D)}{1-x_D}\right]_+\Big) + \frac{N_c}{24\pi}\Big(\delta(1-x_D)\Big[-11+2\pi^2\\
&\quad-12\mathrm{Li}_2\left[\frac{2-3z-x+\sqrt{x^2+2(-4+x)z+9z^2}}{2(1-z)}\right]\\
&\quad-12\mathrm{Li}_2\left[\frac{2-x-3z-\sqrt{x^2+2(-4+x)z+9z^2}}{2(1-z)}\right]\Big]\\
&\quad+6\left(\ln(1-x_D) + x_D\ln(1-x_D) - \ln\left(\frac{2}{1-z}\right) - x_D\ln\left(\frac{2}{1-z}\right) - \ln(z) - x_D\ln(z)\right)\\
&\quad-11\left[\frac{1}{1-x_D}\right]_+ - 6\ln\left(\frac{x\mu^2}{Q^2x_D(1-z)}\right)\left[\frac{1+x_D^2}{1-x_D}\right]_+ + 6\ln\left(\frac{x\mu^2}{Q^2x_Dz}\right)\left[\frac{1+x_D^2}{1-x_D}\right]_+\\
&\quad-6\left[\frac{2\ln(1-x_D)}{1-x_D}\right]_+\Big)\Big\},
\end{aligned}
\tag{4.110}
$$

$$
\begin{aligned}
&\mathbf{S}^{qq}_{\text{initial}}(\{p_x(q), p_h(g)\}, p_0(q), x_D) \\
&\quad = \mathbf{P}^{qq}(\{p_x(q), p_h(g)\}, p_0(q), x_D) + \mathbf{K}^{qq}(\{p_x(q), p_h(g)\}, p_0(q), x_D) \\
&\quad = \alpha_s \Big\{ \frac{C_f}{24\pi} \Big(\delta(1-x_D) \left(-78 + 12\pi^2\right) + 6 \Bigg(2(1-x_D) - 2(1+x_D) \ln\left(\frac{1-x_D}{x_D}\right)\Bigg) \\
&\quad -6 \left[\frac{1}{1-x_D}\right]_+ - 4 \ln\left(\frac{x\mu^2}{Q^2 x_D (1-z)}\right) \left[\frac{1+x_D^2}{1-x_D}\right]_+ + 4 \left[\frac{2\ln\left(\frac{1-x_D}{x_D}\right)}{1-x_D}\right]_+ \Bigg) \\
&\quad + \frac{N_c}{24\pi} \Big(\delta(1-x_D) \Big[9 - 2\pi^2 \\
&\quad +12 \mathrm{Li}_2 \left[\frac{2 - 3z - x + \sqrt{x^2 + 2(-4+x)z + 9z^2}}{2(1-z)}\right] \\
&\quad +12 \mathrm{Li}_2 \left[\frac{2 - x - 3z - \sqrt{x^2 + 2(-4+x)z + 9z^2}}{2(1-z)}\right] \Big] \\
&\quad +6(1+x_D) \left(-\ln[1-x_D] + \ln\left[\frac{2z}{1-z}\right]\right) + 9 \left[\frac{1}{1-x_D}\right]_+ \\
&\quad +6 \ln\left[\frac{x\mu^2}{Q^2 x_D (1-z)}\right] \left[\frac{1+x_D^2}{1-x_D}\right]_+ - 6 \ln\left[\frac{x\mu^2}{Q^2 x_D z}\right] \left[\frac{1+x_D^2}{1-x_D}\right]_+ + 6 \left[-\frac{2\ln[1-x_D]}{-1+x_D}\right]_+ \Big)\Big\},
\end{aligned}
\tag{4.111}
$$

$$
\begin{aligned}
&\mathbf{S}^{qg}_{\text{initial}}(\{p_h(q), p_x(q)\}, p_0(q), x_D) \\
&\quad = \mathbf{P}^{qg}(\{p_h(q), p_x(q)\}, p_0(q), x_D) + \mathbf{K}^{qg}(\{p_h(q), p_x(q)\}, p_0(q), x_D) \\
&\quad = \alpha_s \Big\{ \frac{N_c}{72\pi} \Big(\delta(1-x_D) \Big[-227 + 30\pi^2 - 33 \ln\left(\frac{x\mu^2}{Q^2(1-z)}\right) - 33 \ln\left(\frac{x\mu^2}{Q^2 z}\right) \\
&\quad +36 \mathrm{Li}_2 \left[\frac{2 - 3z - x + \sqrt{x^2 + 2(-4+x)z + 9z^2}}{2(1-z)}\right] \\
&\quad +36 \mathrm{Li}_2 \left[\frac{2 - x - 3z - \sqrt{x^2 + 2(-4+x)z + 9z^2}}{2(1-z)}\right] \Big] \\
&\quad + \frac{36}{x_D} \Big((-1 + x_D(2 - (1-x_D)x_D)) \Big(-3\ln(1-x_D) - 2\ln\left(\frac{1}{x_D}\right) + \ln\left(\frac{2}{1-z}\right) \\
&\quad + \ln(z) + \ln\left(-\frac{x\mu^2}{Q^2 x_D(-1+z)}\right) + \ln\left(\frac{x\mu^2}{Q^2 x_D z}\right) \Big)\Big) - 9 \Big(\Big(3 + 4 \ln\left(-\frac{x\mu^2}{Q^2 x_D (-1+z)}\right) \\
&\quad +4 \ln\left(\frac{x\mu^2}{Q^2 x_D z}\right) \Big) \left[\frac{1}{1-x_D}\right]_+ - 2 \left(4 \left[-\frac{\ln\left(-1 + \frac{1}{x_D}\right)}{-1+x_D}\right]_+ + \left[-\frac{2\ln(1-x_D)}{-1+x_D}\right]_+ \right) \Big)\Big) \\
&\quad + \frac{n_f}{36\pi} \delta(1-x_D) \left(3 \ln\left(\frac{x\mu^2}{Q^2(1-z)}\right) + 3 \ln\left(\frac{x\mu^2}{Q^2 z}\right) + 16 \right) \Big\},
\end{aligned}
\tag{4.112}
$$

$$\begin{aligned}
&\mathbf{S}^{gg}_{\text{initial}}(\{p_h(q), p_x(g)\}, p_0(g), x_D) \\
&\quad = \mathbf{P}^{gg}(\{p_h(q), p_x(g)\}, p_0(g), x_D) + \mathbf{K}^{gg}(\{p_h(q), p_x(g)\}, p_0(g), x_D) \\
&\quad = \alpha_s \frac{C_f}{4\pi x_D}\Big(2x_D^2 + 2(2-x_D)^2 \ln\left(\frac{1-x_D}{x_D}\right) + (2-x_D)^2 \ln(1-x_D) \\
&\quad -(2-x_D)^2 \ln\left(\frac{2z}{1-z}\right) - (2-x_D)^2 \left(\ln\left(\frac{x\mu^2}{Q^2 x_D(1-z)}\right) + \ln\left(\frac{x\mu^2}{Q^2 x_D z}\right)\right)\Big),
\end{aligned} \tag{4.113}$$

$$\begin{aligned}
&\mathbf{S}^{qq}_{\text{final}}(\{p_0(q), p_x(g)\}, p_h(q), z_D) \\
&\quad = \mathbf{P}_{qq}(\{p_0(q), p_x(g)\}, p_h(q), z_D) + \mathbf{H}_{qq}(\{p_0(q), p_x(g)\}, p_h(q), z_D) \\
&\quad = \alpha_s\Big\{\frac{n_f}{12\pi}\left(-1 + \delta(1-z_D) + \left[\frac{1}{1-z_D}\right]_+\right) + \frac{N_c}{24\pi}\Big(\delta(1-z_D)\Big[-11 + 2\pi^2 \\
&\quad -12\mathrm{Li}_2\left[\frac{z(1-x+z) - 1 - \sqrt{1 + 2z(1-x) + z^2(x^2+2x-5) + 2z^3(1-x) + z^4}}{2(1-x)z}\right] \\
&\quad -12\mathrm{Li}_2\left[\frac{z(1-x+z) - 1 + \sqrt{1 + 2z(1-x) + z^2(x^2+2x-5) + 2z^3(1-x) + z^4}}{2(1-x)z}\right]\Big] \\
&\quad +11 - 6\ln\left(\frac{1-z}{1-x}\right) - 6z_D \ln\left(\frac{1-z}{1-x}\right) + 6\ln(1-z_D) + 6z_D\ln(1-z_D) \\
&\quad -11\left[\frac{1}{1-z_D}\right]_+ + 6\ln(z_D)\left[\frac{1+z_D^2}{1-z_D}\right]_+ - 6\ln\left(\frac{xz_D\mu^2}{Q^2(1-x)}\right)\left[\frac{1+z_D^2}{1-z_D}\right]_+ \\
&\quad +6\ln\left(\frac{xz_D\mu^2}{Q^2 z}\right)\left[\frac{1+z_D^2}{1-z_D}\right]_+ - 6\left[\frac{2\ln(1-z_D)}{1-z_D}\right]_+\Big) + \frac{C_f}{24\pi}\Big(\delta(1-z_D)\Big[-60 + 8\pi^2 \\
&\quad +24\mathrm{Li}_2\left[\frac{z(1-x+z) - 1 - \sqrt{1 + 2z(1-x) + z^2(x^2+2x-5) + 2z^3(1-x) + z^4}}{2(1-x)z}\right] \\
&\quad +24\mathrm{Li2}\left[\frac{z(1-x+z) - 1 + \sqrt{1 + 2z(1-x) + z^2(x^2+2x-5) + 2z^3(1-x) + z^4}}{2(1-x)z}\right]\Big] \\
&\quad +12 - 12z_D + 12\ln\left(\frac{1-z}{1-x}\right) + 12z_D\ln\left(\frac{1-z}{1-x}\right) - 24\ln(1-z_D) - 24z_D\ln(1-z_D) \\
&\quad -12\ln\left(\frac{1}{z_D}\right) - 12z_D\ln\left(\frac{1}{z_D}\right) + 24\ln(z_D)\left[\frac{1+z_D^2}{1-z_D}\right]_+ - 12\ln\left(\frac{xz_D\mu^2}{Q^2 z}\right)\left[\frac{1+z_D^2}{1-z_D}\right]_+ \\
&\quad +12\left[\frac{2\ln\left(\frac{1-z_D}{z_D}\right)}{1-z_D}\right]_+ + 12\left[\frac{2\ln(1-z_D)}{1-z_D}\right]_+\Big)\Big\},
\end{aligned} \tag{4.114}$$

$$\begin{aligned}
&\mathbf{S}^{qg}_{\text{final}}(\{p_0(g), p_x(q)\}, p_h(q), z_D) \\
&\quad = \mathbf{P}_{qg}(\{p_0(g), p_x(q)\}, p_h(q), z_D) + \mathbf{H}_{qg}(\{p_0(g), p_x(q)\}, p_h(q), z_D) \\
&\quad = \alpha_s\{-\frac{N_c}{4\pi z_D}(2-z_D)^2\left(\ln\left(\frac{1-z}{1-x}\right) - \ln(1-z_D) + \ln(z_D)\right) \\
&\quad +\frac{C_f}{2\pi z_D}\left(z_D^2 + (2-z_D)^2\ln\left(\frac{1-z_D}{z_D}\right) + 3(2-z_D)^2\ln(z_D)\right).
\end{aligned} \tag{4.115}$$

$$
\begin{aligned}
&\mathbf{S}^{gq}_{\text{final}}(\{p_0(q),p_x(q)\},p_h(g),z_D)\\
&\quad=\mathbf{P}_{gq}(\{p_0(q),p_x(q)\},p_h(g),z_D)+\mathbf{H}_{gq}(\{p_0(q),p_x(q)\},p_h(g),z_D)\\
&\quad=\alpha_s\Bigl\{\frac{N_c}{8\pi}\Bigl(\frac{1}{9}\delta(1-z_D)\Bigl[-227+30\pi^2-33\ln\left(\frac{x\mu^2}{Q^2(1-x)}\right)-33\ln\left(\frac{x\mu^2}{Q^2z}\right)\\
&\quad+36\mathrm{Li}_2\left[\frac{z(1-x+z)-1-\sqrt{1+2z(1-x)+z^2(x^2+2x-5)+2z^3(1-x)+z^4}}{2(1-x)z}\right]\\
&\quad+36\mathrm{Li}_2\left[\frac{z(1-x+z)-1+\sqrt{1+2z(1-x)+z^2(x^2+2x-5)+2z^3(1-x)+z^4}}{2(1-x)z}\right]\Bigr]\\
&\quad+\frac{1}{z_D}\Bigl[3z_D+12\ln(1-z_D)+8\ln\left(\frac{1}{z_D}\right)+20\ln(z_D)-4\ln\left(\frac{xz_D\mu^2}{Q^2(1-x)}\right)\\
&\quad+4\Bigl((-1+z_D(2+(-1+z_D)z_D))\ln\left(\frac{1-z}{1-x}\right)-z_D(2+(-1+z_D)z_D)\Bigl(3\ln(1-z_D)\\
&\quad+2\ln\left(\frac{1}{z_D}\right)+5\ln(z_D)-\ln\left(\frac{xz_D\mu^2}{Q^2(1-x)}\right)-\ln\left(\frac{xz_D\mu^2}{Q^2z}\right)\Bigr)\Bigr)-4\ln\left(\frac{xz_D\mu^2}{Q^2z}\right)\Bigr]\\
&\quad+\left(-3+20\ln(z_D)-4\ln\left(\frac{xz_D\mu^2}{Q^2(1-x)}\right)-4\ln\left(\frac{xz_D\mu^2}{Q^2z}\right)\right)\left[\frac{1}{1-z_D}\right]_+\\
&\quad+2\left(4\left[\frac{\ln\left(\frac{1-z_D}{z_D}\right)}{1-z_D}\right]_++\left[\frac{2\ln[1-z_D]}{1-z_D}\right]_+\right)\Bigr)\\
&\quad+\frac{n_f}{36\pi}\delta(1-z_D)\left(3\ln\left(\frac{x\mu^2}{Q^2(1-z)}\right)+3\ln\left(\frac{x\mu^2}{Q^2z}\right)+16\right)\Bigr\},
\end{aligned}
\tag{4.116}
$$

$$
\begin{aligned}
&\mathbf{S}^{qg}_{\text{final}}(\{p_0(q),p_x(g)\},p_h(q),z_D)\\
&\quad=\mathbf{P}_{qg}(\{p_0(q),p_x(g)\},p_h(q),z_D)+\mathbf{H}_{qg}(\{p_0(q),p_x(g)\},p_h(q),z_D)\\
&\quad=\alpha_s\Bigl\{\frac{N_c}{8\pi}\Bigl(-8\ln\left(\frac{1-z}{1-x}\right)+\frac{8\ln\left(\frac{1-z}{1-x}\right)}{z_D}+2z_D\ln\left(\frac{1-z}{1-x}\right)+8\ln(1-z_D)\\
&\quad-\frac{8\ln(1-z_D)}{z_D}-2z_D\ln(1-z_D)-8\ln(z_D)+\frac{8\ln(z_D)}{z_D}+2z_D\ln(z_D)\Bigr)\\
&\quad+\frac{C_f}{8\pi}\Bigl(4z_D+16\ln\left(\frac{1-z}{1-x}\right)-\frac{16\ln\left(\frac{1-z}{1-x}\right)}{z_D}-4z_D\ln\left(\frac{1-z}{1-x}\right)-32\ln(1-z_D)\\
&\quad+\frac{32\ln(1-z_D)}{z_D}+8z_D\ln(1-z_D)-16\ln\left(\frac{1}{z_D}\right)+\frac{16\ln\left(\frac{1}{z_D}\right)}{z_D}+4z_D\ln\left(\frac{1}{z_D}\right)\\
&\quad-32\ln(z_D)+\frac{32\ln(z_D)}{z_D}+8z_D\ln(z_D)\Bigr)\Bigr\},
\end{aligned}
\tag{4.117}
$$

$$\begin{aligned}
&\mathbf{S}^{gg}_{\text{final}}(\{p_0(q),p_x(q)\},p_h(g),z_D)\\
&\quad=\mathbf{P}_{gg}(\{p_0(q),p_x(q)\},p_h(g),z_D)+\mathbf{H}_{gg}(\{p_0(q),p_x(q)\},p_h(g),z_D)\\
&\quad=\alpha_s\Big\{\frac{C_f}{8\pi}\Big(16\ln\left(\frac{xz_D\mu^2}{Q^2(1-x)}\right)-\frac{16\ln\left(\frac{xz_D\mu^2}{Q^2(1-x)}\right)}{z_D}-4z_D\ln\left(\frac{xz_D\mu^2}{Q^2(1-x)}\right)\\
&\quad+16\ln\left(\frac{xz_D\mu^2}{Q^2z}\right)-\frac{16\ln\left(\frac{xz_D\mu^2}{Q^2z}\right)}{z_D}-4z_D\ln\left(\frac{xz_D\mu^2}{Q^2z}\right)\Big)\\
&\quad+\frac{N_c}{8\pi}\Big(-8\ln\left(\frac{xz_D\mu^2}{Q^2(1-x)}\right)+\frac{8\ln\left(\frac{xz_D\mu^2}{Q^2(1-x)}\right)}{z_D}+2z_D\ln\left(\frac{xz_D\mu^2}{Q^2(1-x)}\right)\\
&\quad-8\ln\left(\frac{xz_D\mu^2}{Q^2z}\right)+\frac{8\ln\left(\frac{xz_D\mu^2}{Q^2z}\right)}{z_D}+2z_D\ln\left(\frac{xz_D\mu^2}{Q^2z}\right)\Big)\\
&\quad+\frac{1}{8\pi}\Big(4z_D(1-z_D-2z_D(1-z_D)\Big(2\ln\left(\frac{1}{z_D}\right)+5\ln(z_D)-\ln\left(\frac{xz_D\mu^2}{Q^2(1-x)}\right)-\ln\left(\frac{xz_D\mu^2}{Q^2z}\right)\Big)\Big)\\
&\quad+(2z_D(1-z_D)-1)\ln\left(\frac{1-z}{1-x}\right)+(3-6z_D(1-z_D))\ln(1-z_D)+2\ln\left(\frac{1}{z_D}\right)\\
&\quad+5\ln(z_D)-\ln\left(\frac{xz_D\mu^2}{Q^2(1-x)}\right)-\ln\left(\frac{xz_D\mu^2}{Q^2z}\right)\Big)\Big\},
\end{aligned}\tag{4.118}$$

$$\begin{aligned}
&\mathbf{S}^{qq}_{\text{final}}(\{p_0(g),p_x(q)\},p_h(q),z_D)\\
&\quad=\mathbf{P}_{qq}(\{p_0(g),p_x(q)\},p_h(q),z_D)+\mathbf{H}_{qq}(\{p_0(g),p_x(q)\},p_h(q),z_D)\\
&\quad=\alpha_s\{\frac{C_f}{8\pi}\Big(\frac{1}{3}\delta(1-z_D)\left[-78+12\pi^2\right]+10-4z_D-4\ln\left(\frac{1-z_D}{z_D}\right)-4z_D\ln\left(\frac{1-z_D}{z_D}\right)\\
&\quad-6\left[\frac{1}{1-z_D}\right]_++12\ln(z_D)\left[\frac{1+z_D^2}{1-z_D}\right]_++4\left[\frac{2\ln\left(-1+\frac{1}{z_D}\right)}{1-z_D}\right]_+\Big)+\frac{N_c}{8\pi}\Big(\frac{1}{3}\delta(1-z_D)\Big[9-2\pi^2\\
&\quad+12\mathrm{Li}_2\left[\frac{z(1-x+z)-1-\sqrt{1+2z(1-x)+z^2(x^2+2x-5)+2z^3(1-x)+z^4}}{2(1-x)z}\right]\\
&\quad+12\mathrm{Li}_2\left[\frac{z(1-x+z)-1+\sqrt{1+2z(1-x)+z^2(x^2+2x-5)+2z^3(1-x)+z^4}}{2(1-x)z}\right]\Big]\\
&\quad-3+2\ln\left(\frac{1-z}{1-x}\right)+2z_D\ln\left(\frac{1-z}{1-x}\right)-2\ln(1-z_D)-2z_D\ln(1-z_D)+3\left[\frac{1}{1-z_D}\right]_+\\
&\quad-2\ln(z_D)\left[\frac{1+z_D^2}{1-z_D}\right]_++2\left[\frac{2\ln(1-z_D)}{1-z_D}\right]_+\Big)\},
\end{aligned}\tag{4.119}$$

Chapter 5

Results to first order in α_s

In this chapter we present our numerical results for the single-hadron inclusive production of charged particles, measured by the H1 and ZEUS collaborations. Cross sections are normalized to the total cross section and will be presented in distributions in Q^2 and the scaled momentum of the detected hadron x_p defined as $x_p = 2p_h \cdot q/q^2$. In fragmentation function fits, uncertainties at small x_p, such as higher-twist effects, quark and hadron mass effects and unresummed soft-gluon logarithms in the evolution of the FFs, render the theoretical calculations for hadron production data from e^+e^- interactions unreliable when the scaled momentum falls below 0.1. Because of the resulting uncertainties in the FFs at small x_p, and because *ep* interaction data suffer from similar uncertainties at small x_p, we only study *ep* interaction data for which $x_p > 0.1$. Cross sections are calculated to NLO in the $\overline{\text{MS}}$ scheme as described in chapter 3. We set the number of active quark flavours, $n_f = 5$. To account for the initial-state proton, we use the CTEQ6.6M PDF set of Ref. [32] and to account for the final state hadron we use the AKK set of fragmentation functions [34], unless otherwise stated. The charged particles are obtained as a sum of the light charged hadrons ($\pi^\pm$, $K^\pm$, and $p/\overline{p}$):

$$D_a^{h^\pm}(x, \mu_f) = D_a^{\pi^\pm}(x, \mu_f) + D_a^{K^\pm}(x, \mu_f) + D_a^{p/\overline{p}}(x, \mu_f). \tag{5.1}$$

We use CTEQ6.6M NLO value $\Lambda_{\text{QCD}}^{(5)} = 226$ MeV. The factorization / renormalization scale is chosen as $\mu = Q$ unless stated otherwise.

5.1 Scaled momentum distributions

In this section we compare theoretical predictions with single hadron inclusive production x_p distributions measured by H1 [56] (see Fig. 5.1 for the kinematic constraints) and ZEUS [57] (see Fig.

5.2). The predictions generally agree well with the ZEUS data (Fig. 5.3). The predictions using the Kretzer FF set [36] are similar to those in Ref. [58], where the CTEQ5M1 PDF set was used. A similar comparison was performed in Ref. [59] using the BKK FF set [60], and the agreements were good when the CTEQ3M and MRSA$'$ PDF sets were used. We also show our results using the KKP set of fragmentation functions [35] that also agree with the data. In figure 5.4, we show our results obtained with a variation in μ^2 of a factor of 2, which gives us an estimate of the theoretical uncertainty of our calculation. In figure 5.5 we can also see the variation introduced by choosing a different PDF set, in this case the MSTW set [33], and in figure 5.6, we can see the K-factor obtained for this prediction.

The results for the H1 data are divided into two groups, one for low Q^2 ($12\text{GeV}^2 < Q^2 < 100\text{GeV}^2$) and another for high Q^2 ($100\text{GeV}^2 < Q^2 < 8000\text{GeV}^2$). In figures 5.7 to 5.13 we show our results and the same variations as before.

For both the H1 and ZEUS data, the predictions using the KKP FF set are the most gradual in x_p, while the Kretzer predictions are the steepest. The predictions from the AKK and Kretzer sets are quite similar, particularly at large x_p and for all x_p values of the high Q H1 data. The uncertainty due to the choice of FF set is largest at large x_p, since the data from e^+e^- interactions are most inaccurate and most scarce at large x_p. The predictions for the low Q^2 H1 data show an undershoot at large x_p. This behaviour may result from unresummed logarithms at large x_p in the partonic cross section, since resummation tends to enhance the cross section. The overshoot from the low Q^2 H1 data at small x_p may be due to the theoretical errors in ep interaction data discussed above. Indeed, better agreement is found at small x_p with the high Q^2 H1 data where resummation is less necessary and where higher-twist and mass effects are significantly reduced. The error due to the choice of PDF set is rather small for all values of x_p while the uncertainty due to the scale variation is largest at the large values of scaled momentum. In general, increasing the scale steepens the drop in the cross section with increasing x_p.

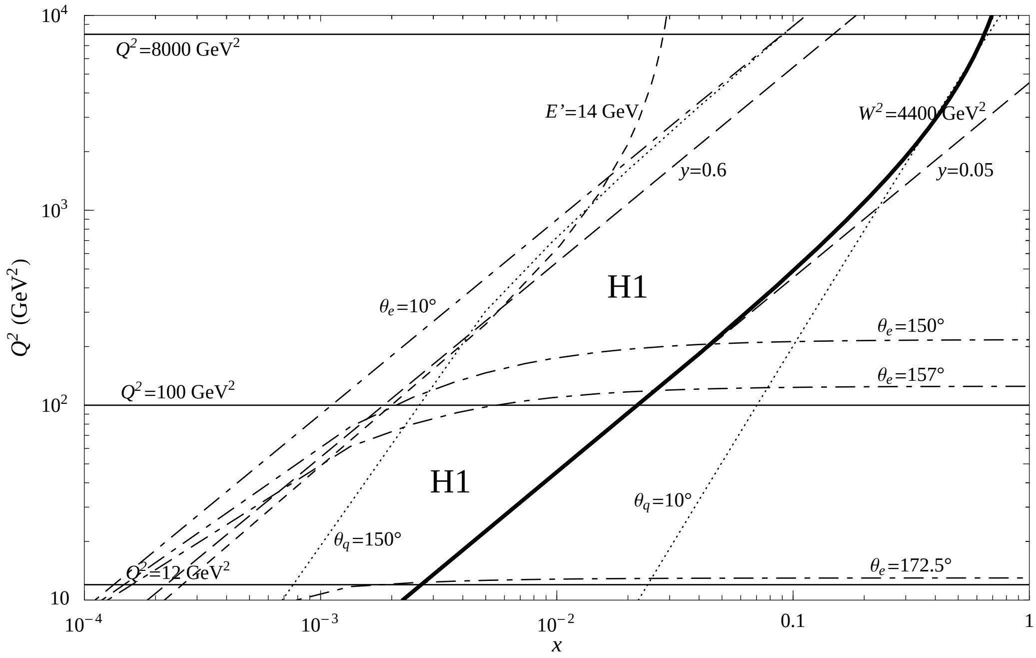

Figure 5.1: Cuts in the (x, Q^2) plane used in the H1 analysis of Ref. [56].

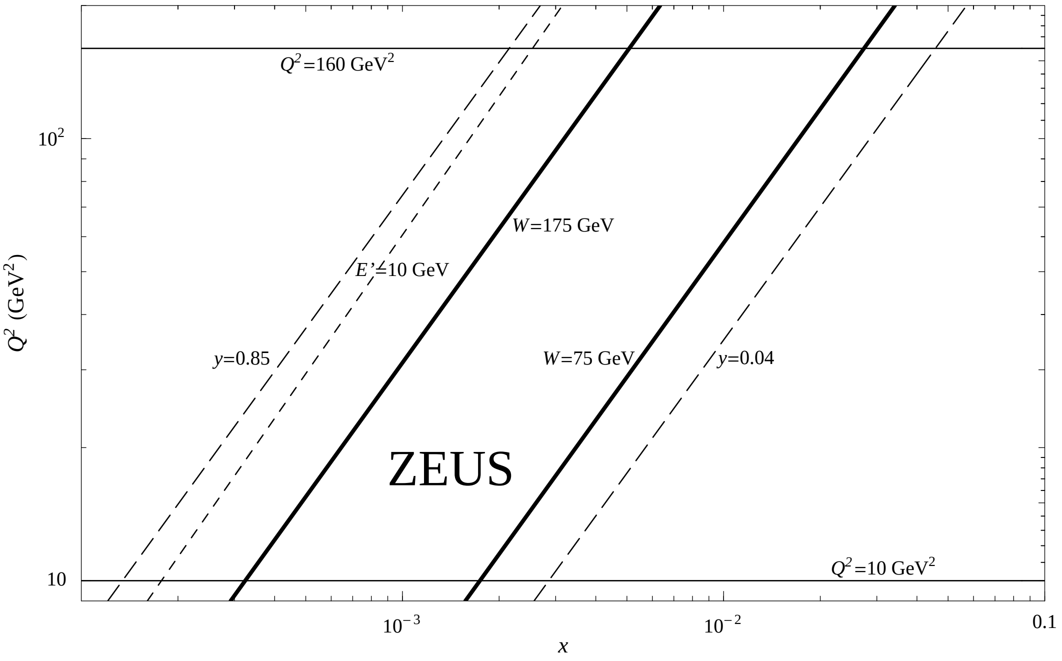

Figure 5.2: Cuts in the (x, Q^2) plane used in the ZEUS analysis of Ref. [57].

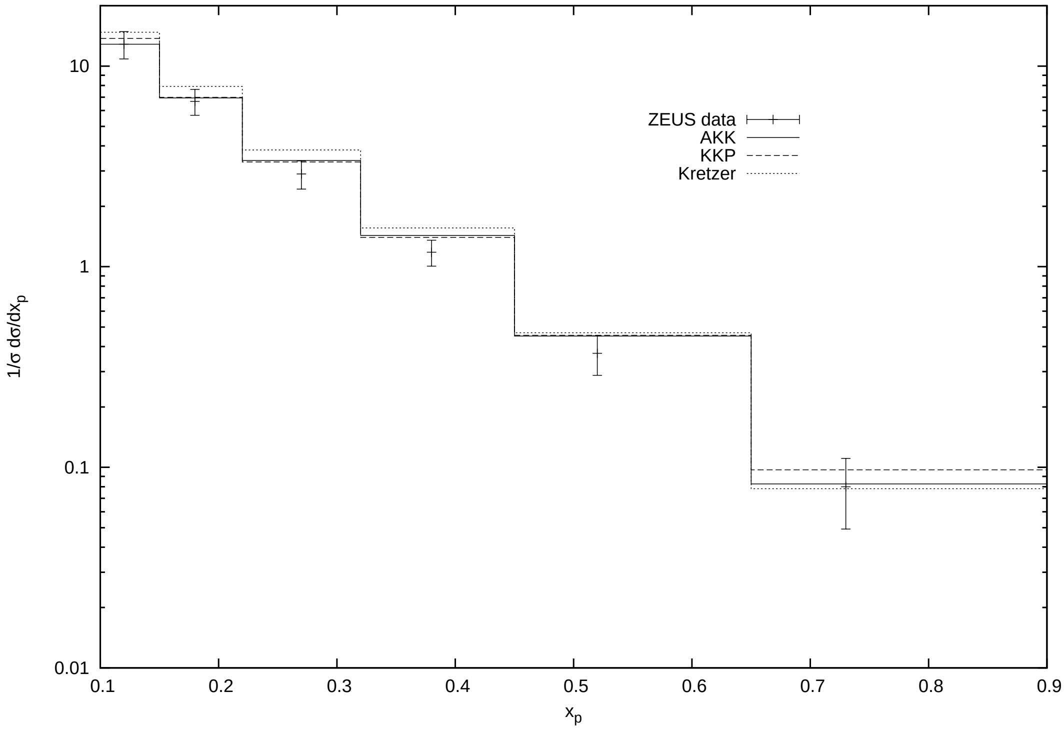

Figure 5.3: Comparisons of theoretical predictions using the AKK, Kretzer and KKP FF sets with the x_p distribution from ZEUS [57].

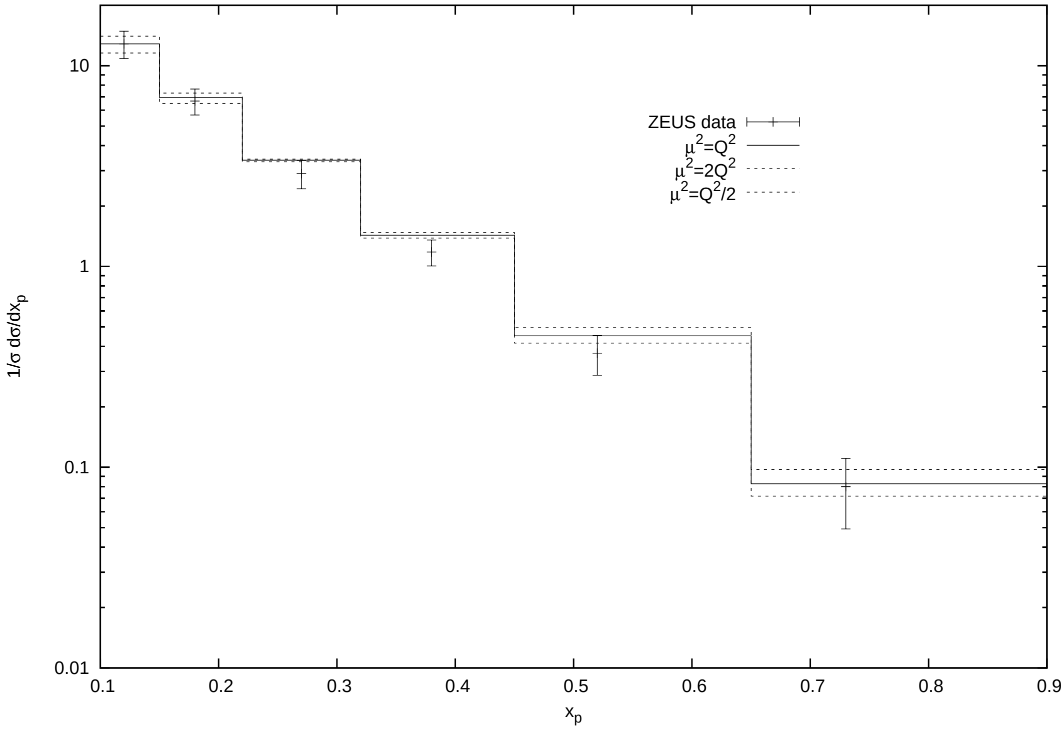

Figure 5.4: As in figure 5.3 but showing the theoretical uncertainty introduced by a change in the scale chosen.

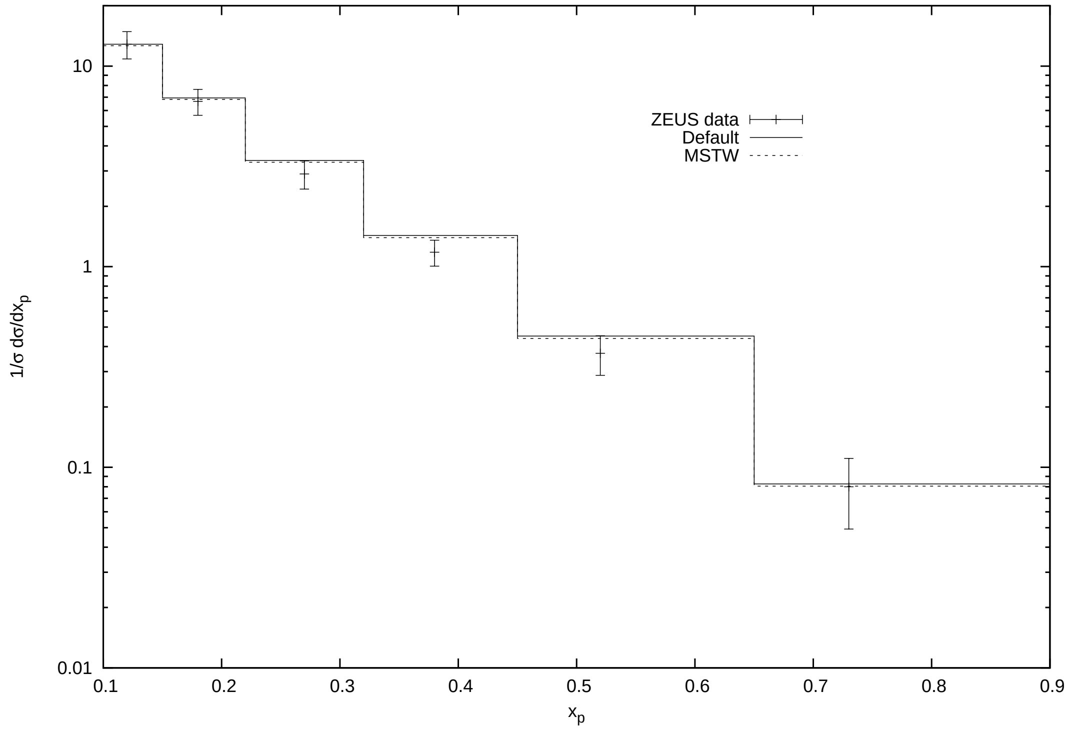

Figure 5.5: As in figure 5.3 but showing the theoretical uncertainty introduced by choosing a different PDF set.

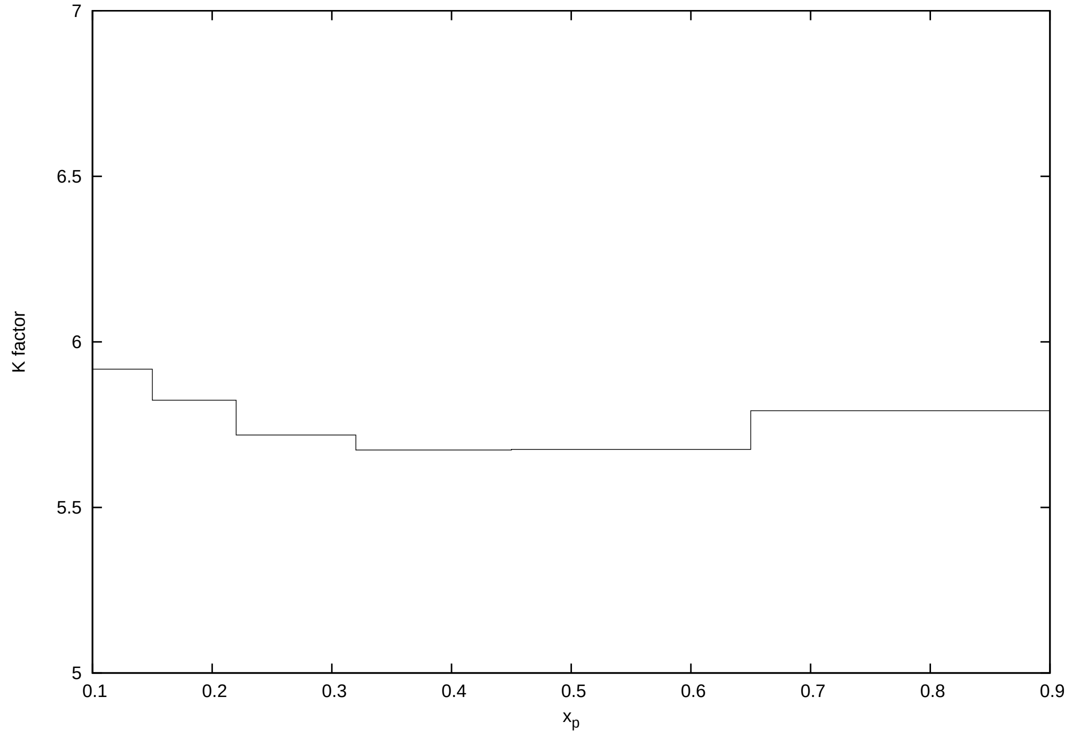

Figure 5.6: K-factor corresponding to our predictions in figure 5.3 with AKK and CTEQ6.6M.

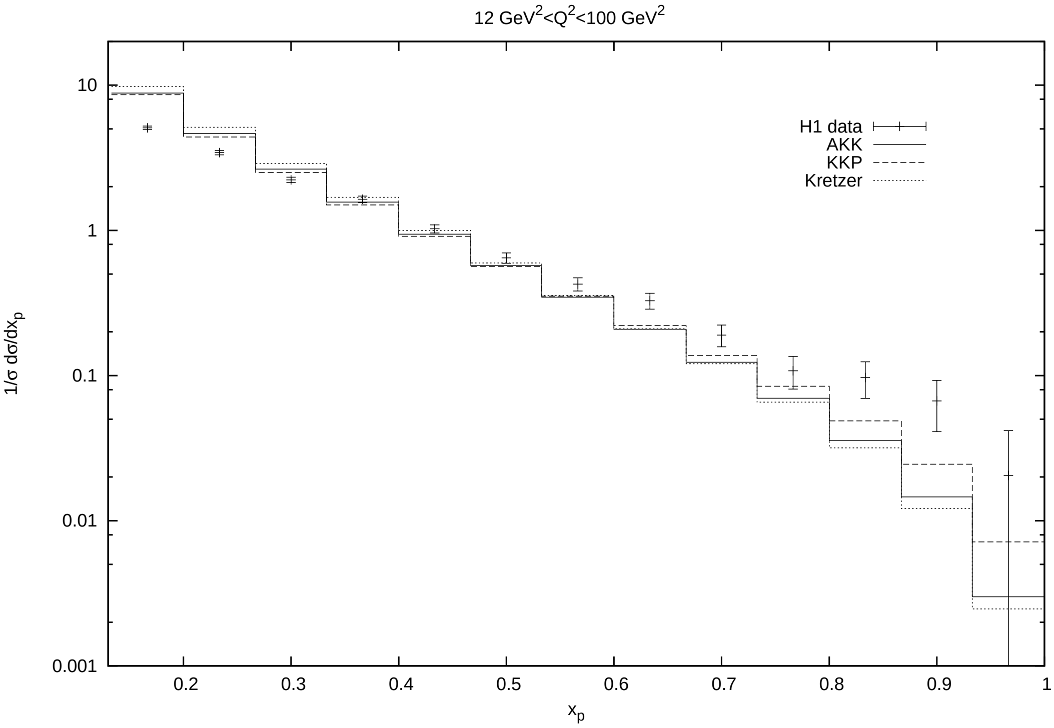

Figure 5.7: Comparisons of theoretical predictions using the AKK, Kretzer and KKP FF sets with the x_p distribution from H1 [56] at low Q^2.

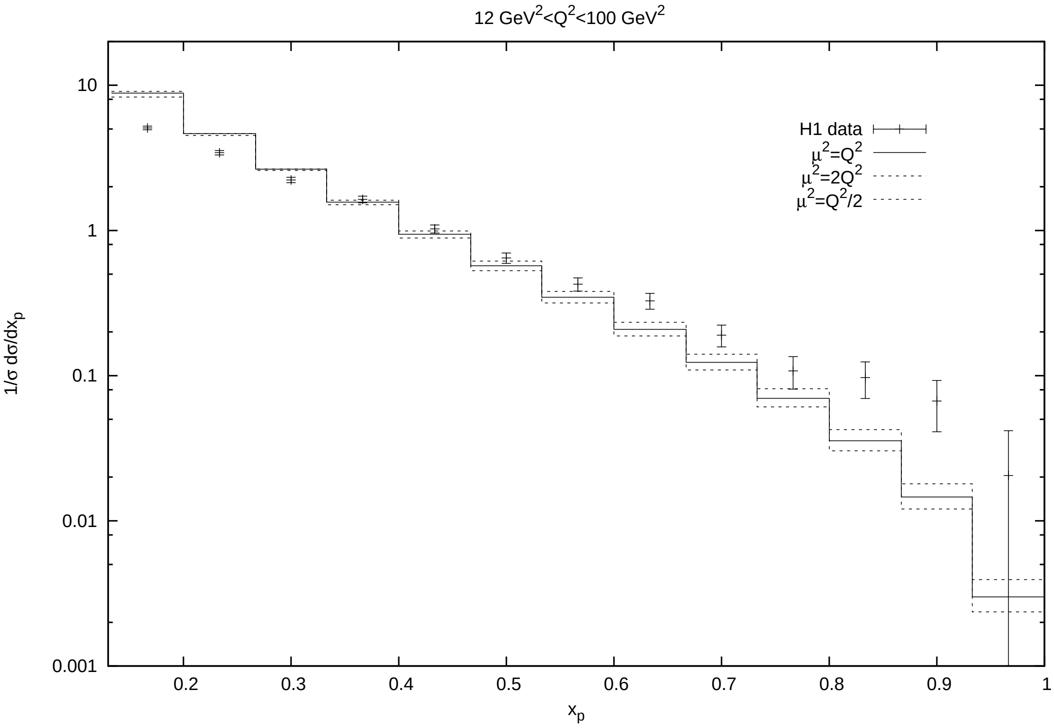

Figure 5.8: As in figure 5.7 but showing the theoretical uncertainty introduced by a change in the scale chosen.

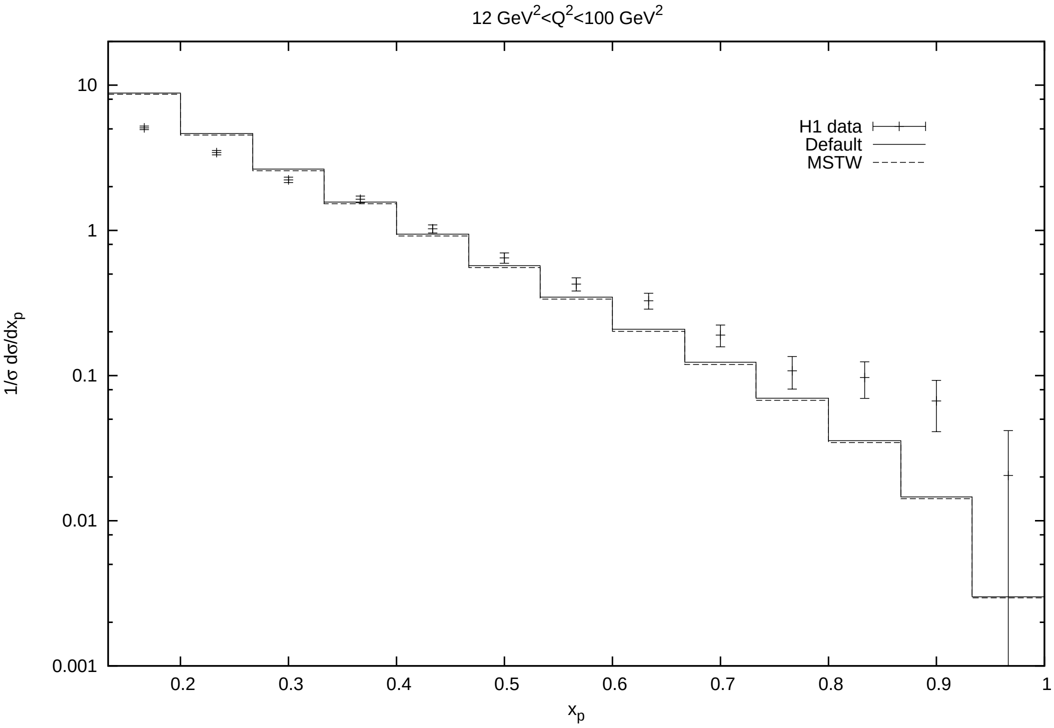

Figure 5.9: As in figure 5.7 but showing the theoretical uncertainty introduced by choosing a different PDF set.

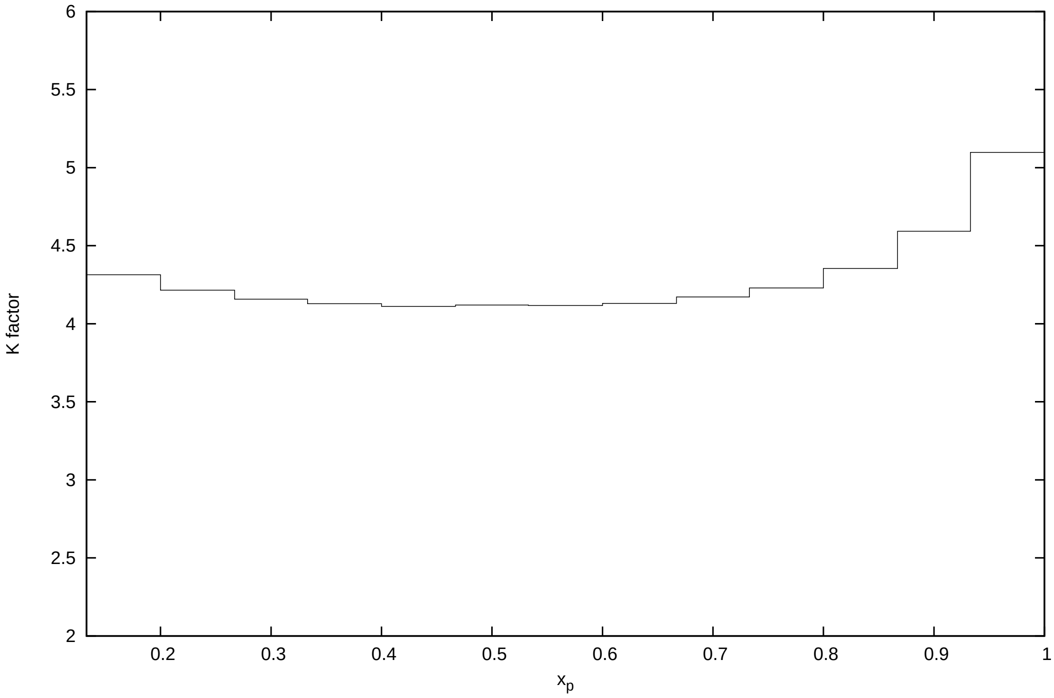

Figure 5.10: K-factor corresponding to our predictions in figure 5.7 with AKK and CTEQ6.6M.

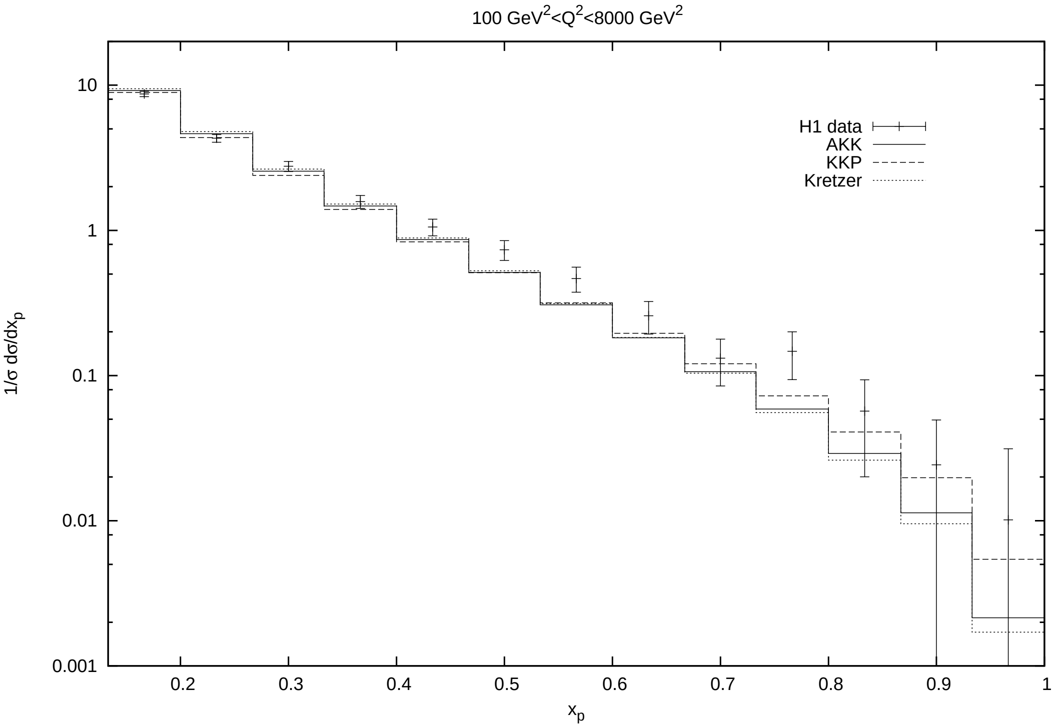

Figure 5.11: Comparisons of theoretical predictions using the AKK, Kretzer and KKP FF sets with the x_p distribution from H1 [56] at high Q^2.

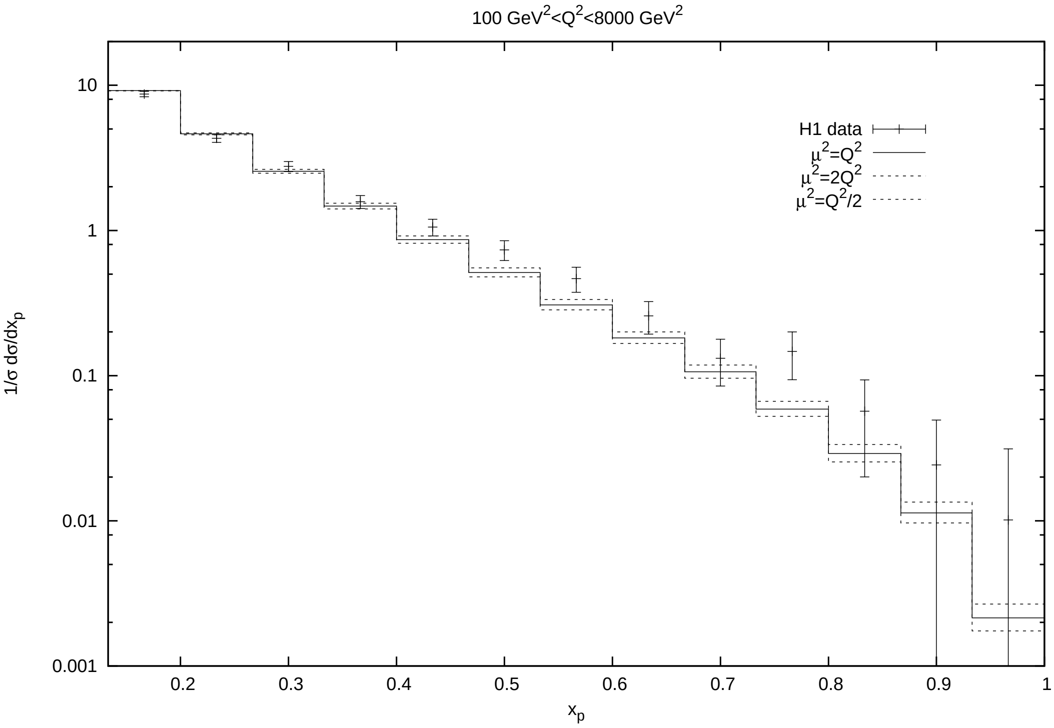

Figure 5.12: As in figure 5.11 but showing the theoretical uncertainty introduced by a change in the scale chosen.

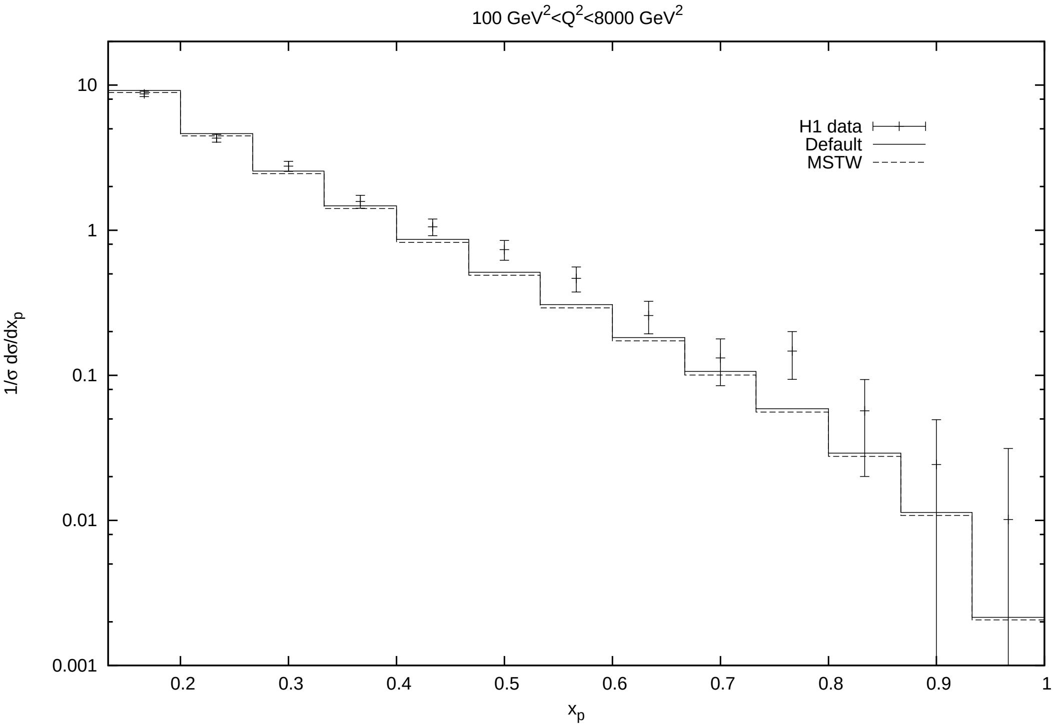

Figure 5.13: As in figure 5.11 but showing the theoretical uncertainty introduced by choosing a different PDF set.

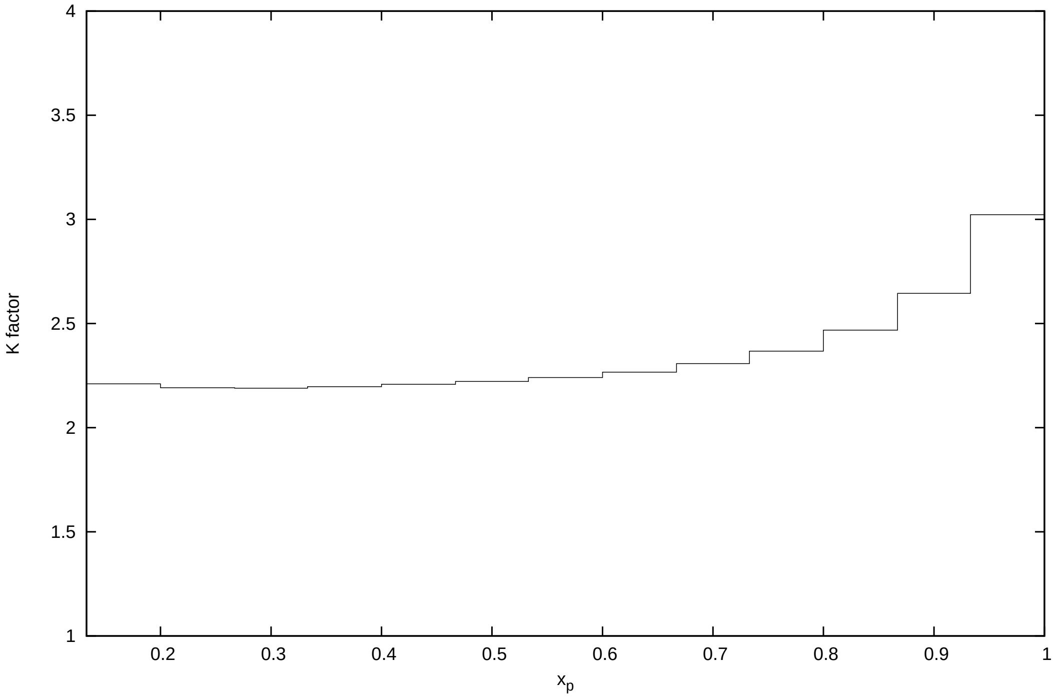

Figure 5.14: K-factor corresponding to our predictions in figure 5.11 with AKK and CTEQ6.6M

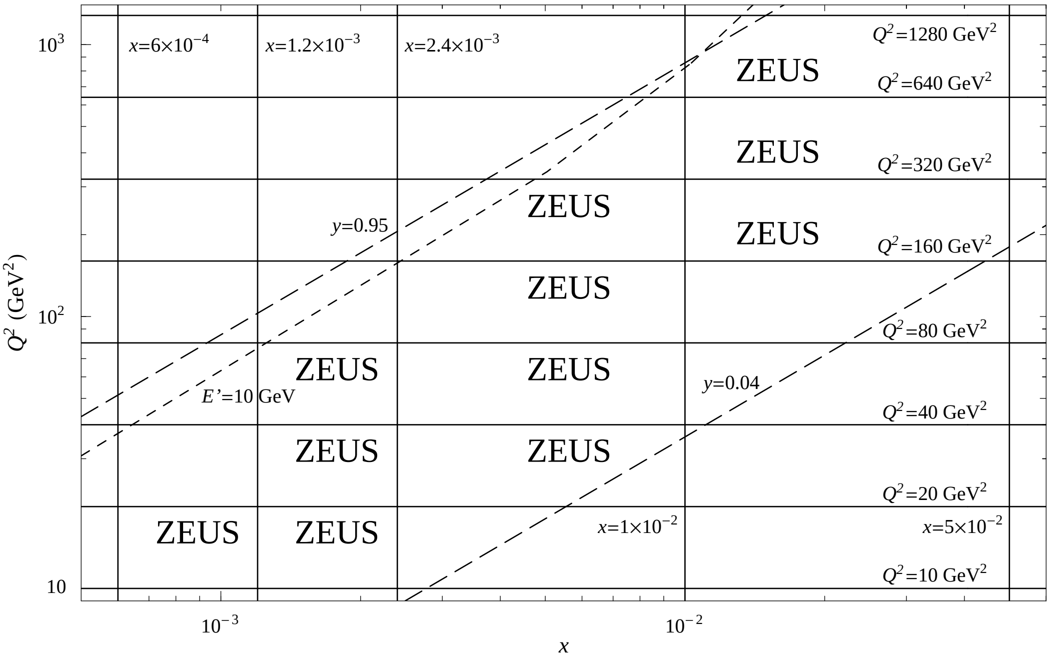

Figure 5.15: Cuts in the (x, Q^2) plane used in the ZEUS analysis of Ref. [61].

5.2 Distributions in Q^2

Next we compare theoretical predictions with the single hadron inclusive production measurements at various Q^2 values from ZEUS [61] (see Fig. 5.15). Our predictions are presented in figures ??-5.18, where we have separated the points for different ranges in x_B by a factor Δ. The predictions agree well with the ZEUS data (Fig. 5.16), except for, at low Q^2, they overshoot at small x_p and the undershoot at large x_p. Note that the theoretical predictions are rather constant over the whole Q^2 range, as foreseen in our theoretical description. Except at the lower Q^2 and smaller x_p region, the AKK predictions tend to be closer to the Kretzer predictions than to the KKP ones. The uncertainty due to the choice of PDF set for the proton (Fig. 5.18) is everywhere insignificant. At smaller x_p values, the uncertainty with respect to the arbitrary scale choice (Fig. 5.17) become less relevant with increasing Q^2, and is unimportant for all Q^2 at the other x_p values. The large deviation of the prediction for $\mu = Q/2$ (dotted line) from the one for $\mu = Q$ is caused by the vanishing of the c quark FF below threshold. This behaviour is not physical since we have neglected charm mass effects. The procedure for incorporating these effects is given in Ref. [62], which amounts to retaining the heavy quark mass dependence in the heavy quark flavour creation from photon-gluon fusion, and using the same scaling variable that results in the latter process for the heavy quark flavour excitation. Furthermore, the matching conditions of Ref. [63] must be imposed on the FFs at the quark flavour thresholds. In any case, our results at low Q^2 suffer other theoretical errors mentioned earlier, such as higher twist.

New, more precise data were released by the H1 collaboration in 2007 [64]. Our comparisons are shown in figures 5.19, 5.20 and 5.21. In this case the obtained distributions do not match the data very well, especially in the lowest and highest bins in x_p. The results for AKK and Kretzer remain quite close, while the KKP set shows the largest deviation from these two. The uncertainty due to the choice of PDF is negligible again here and the uncertainty in the scale variation remains more or less constant. Similar data has been analyzed by the ZEUS collaboration [65], our comparison with these data is shown in figures 5.22, 5.23 and 5.24, with similar conclusions to the comparison with the H1 data.

We also compared these data to our predictions including the Z boson contribution, expecting to see some effect at high Q^2. However, since all the cross sections are normalized to the total cross section, where the effect is also present, it is impossible to distinguish between curves with and without the Z boson contribution. We can nevertheless, plot the cross sections without normalization to see the effect of considering the complete neutral current cross section (Fig. 5.25). The effect is found to be as large as 30% for the highest Q^2 bin and, as can be seen from the plot, the effect is similar for all bins in x_p.

Unfortunately, there are no data available for single particle inclusive production in charged-current deep inelastic scattering, but since we have all the formalism and code in place, we will show here a cross section obtained as in 5.25, without normalization and for production of charged particles in charged current DIS. The kinematic region was chosen to be the same as in the H1 analysis. The results are shown in figure 5.26.

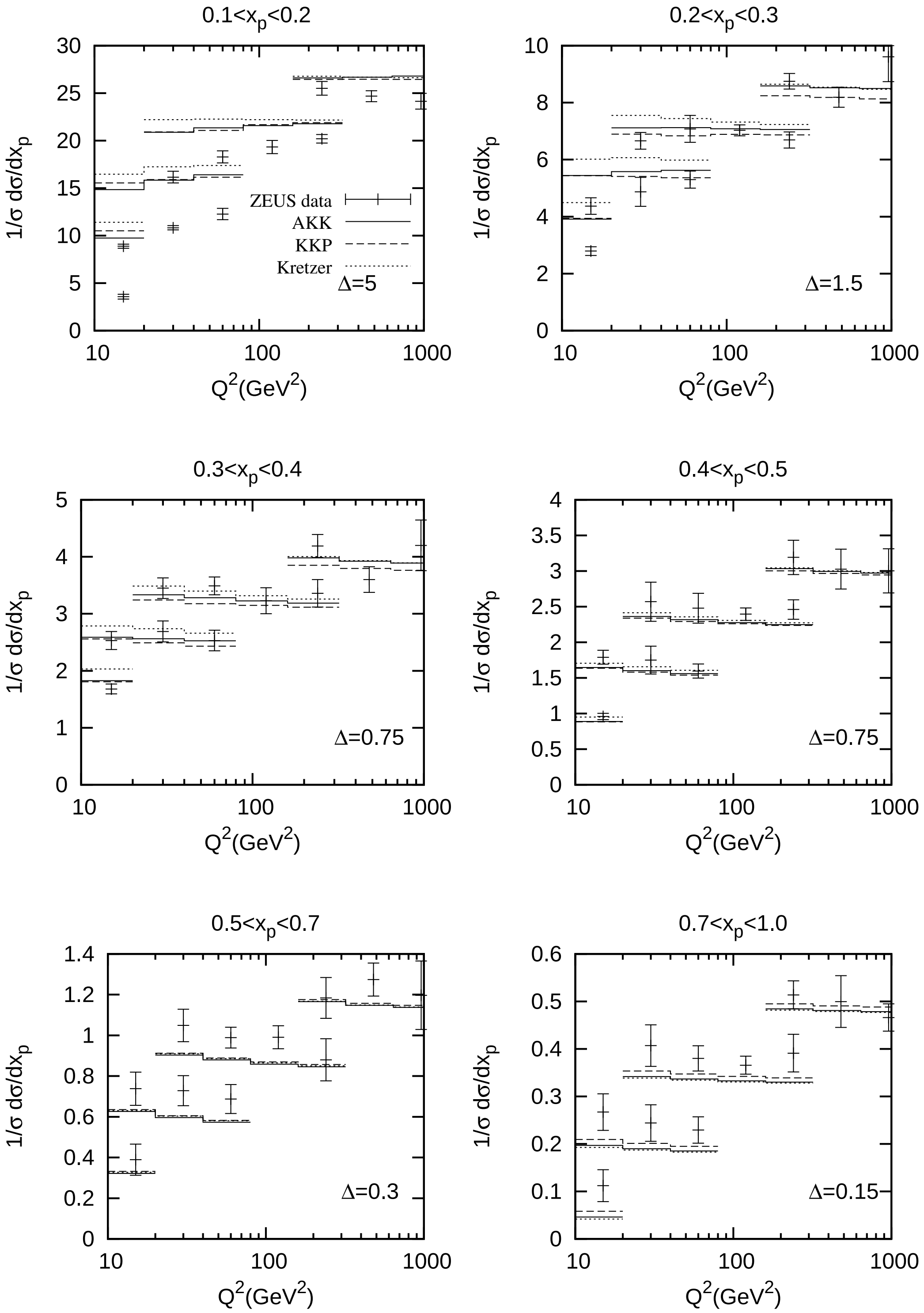

Figure 5.16: Comparisons of theoretical predictions using the AKK, Kretzer and KKP FF sets with the Q^2 distribution from ZEUS [61]. The factor Δ is a shift in the actual values separating the results for different ranges in x_B according to the kinematic cuts shown in figure 5.15.

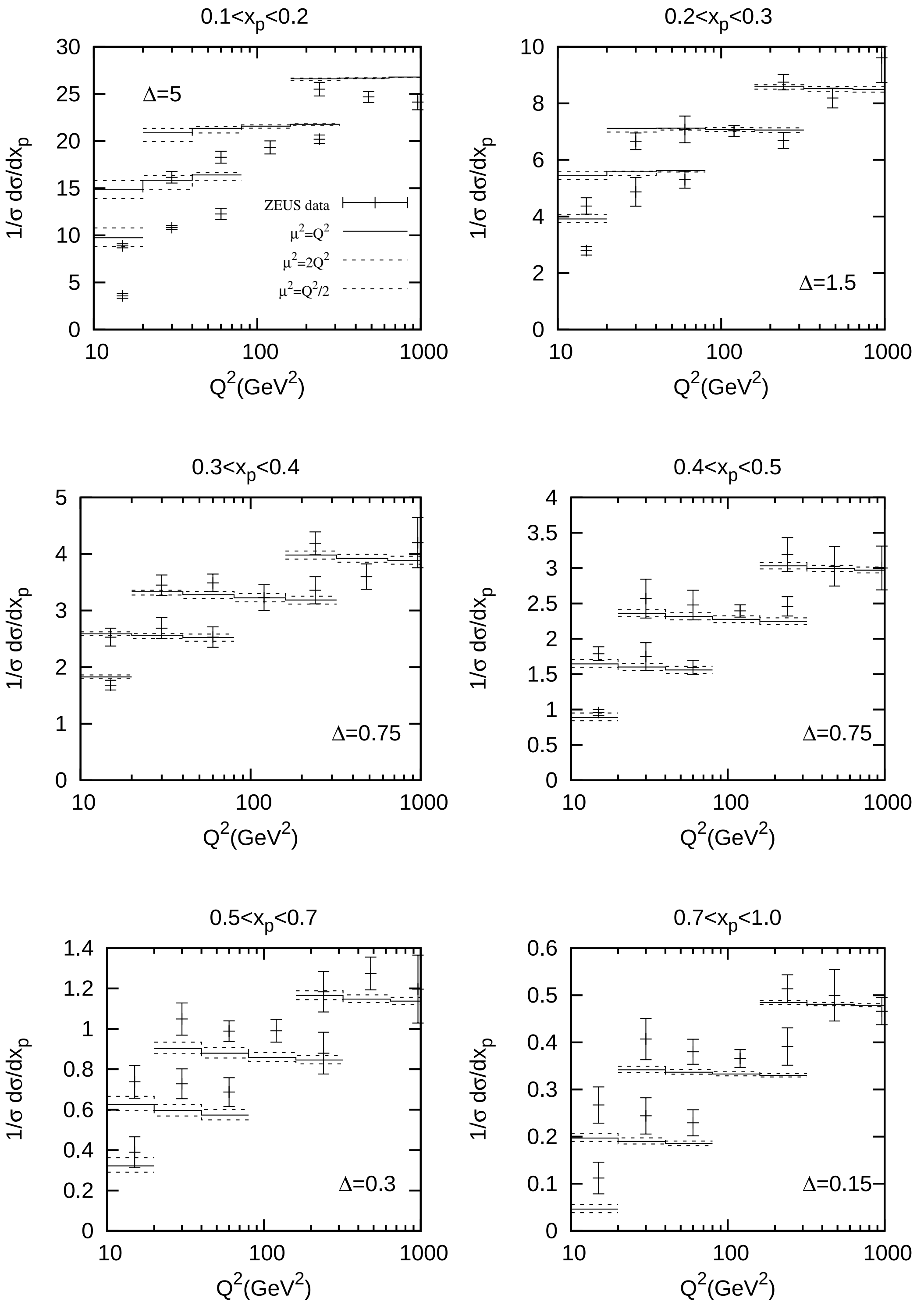

Figure 5.17: As in figure 5.16 but showing the theoretical uncertainty introduced by a change in the scale chosen.

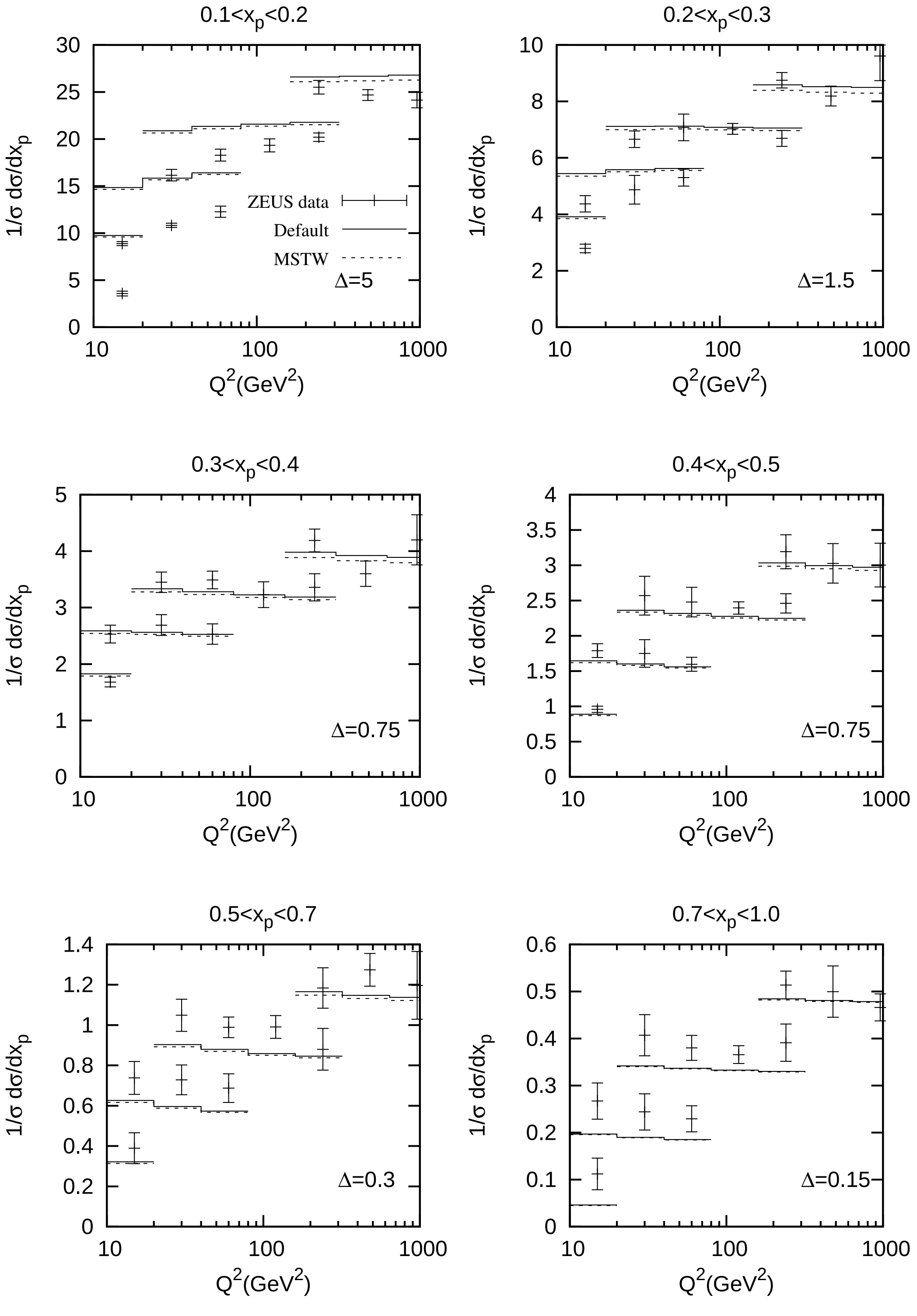

Figure 5.18: As in figure 5.16 but showing the theoretical uncertainty introduced by choosing a different PDF set.

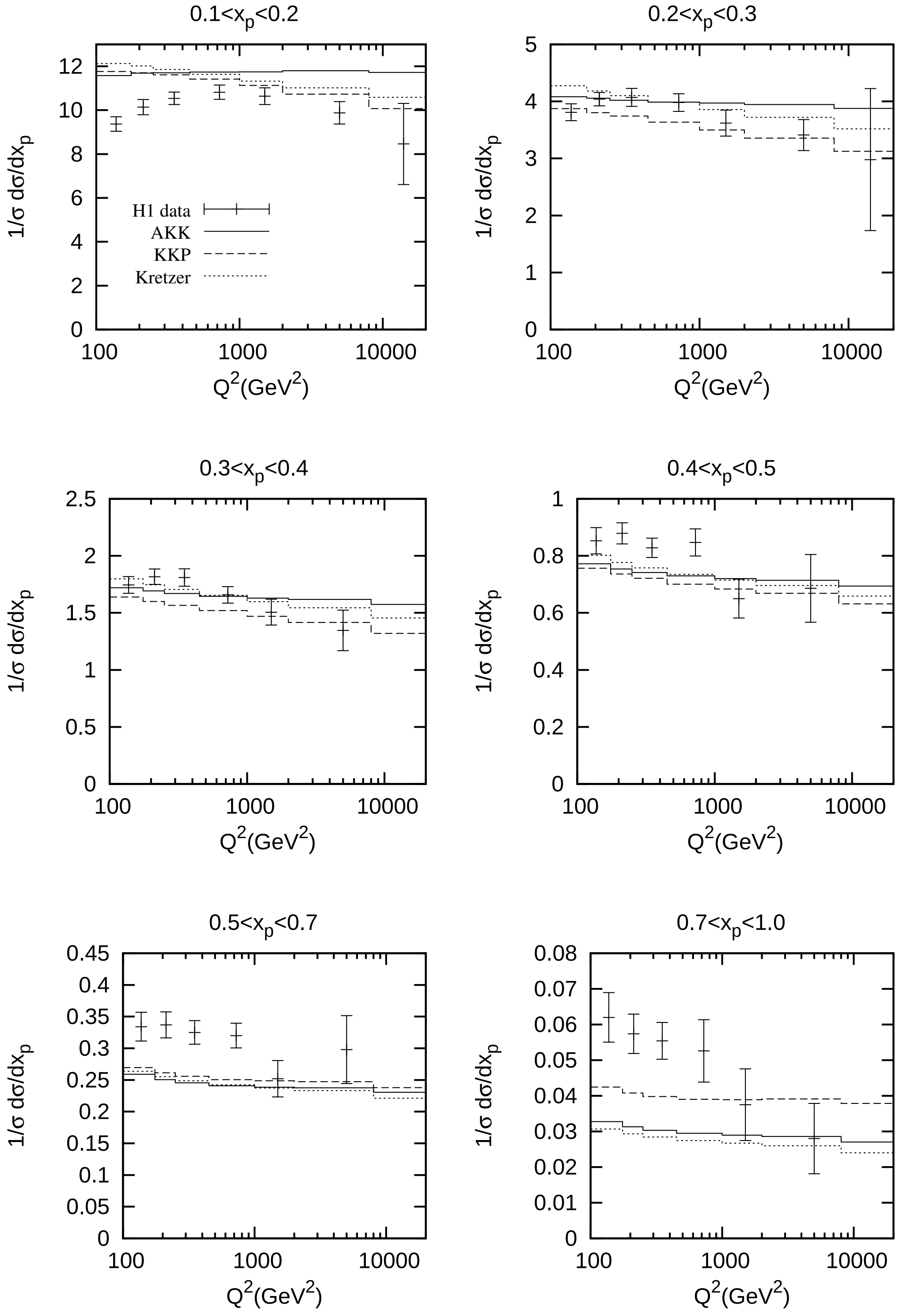

Figure 5.19: Comparisons of theoretical predictions using the AKK, Kretzer and KKP FF sets with the Q^2 distribution from H1 [64].

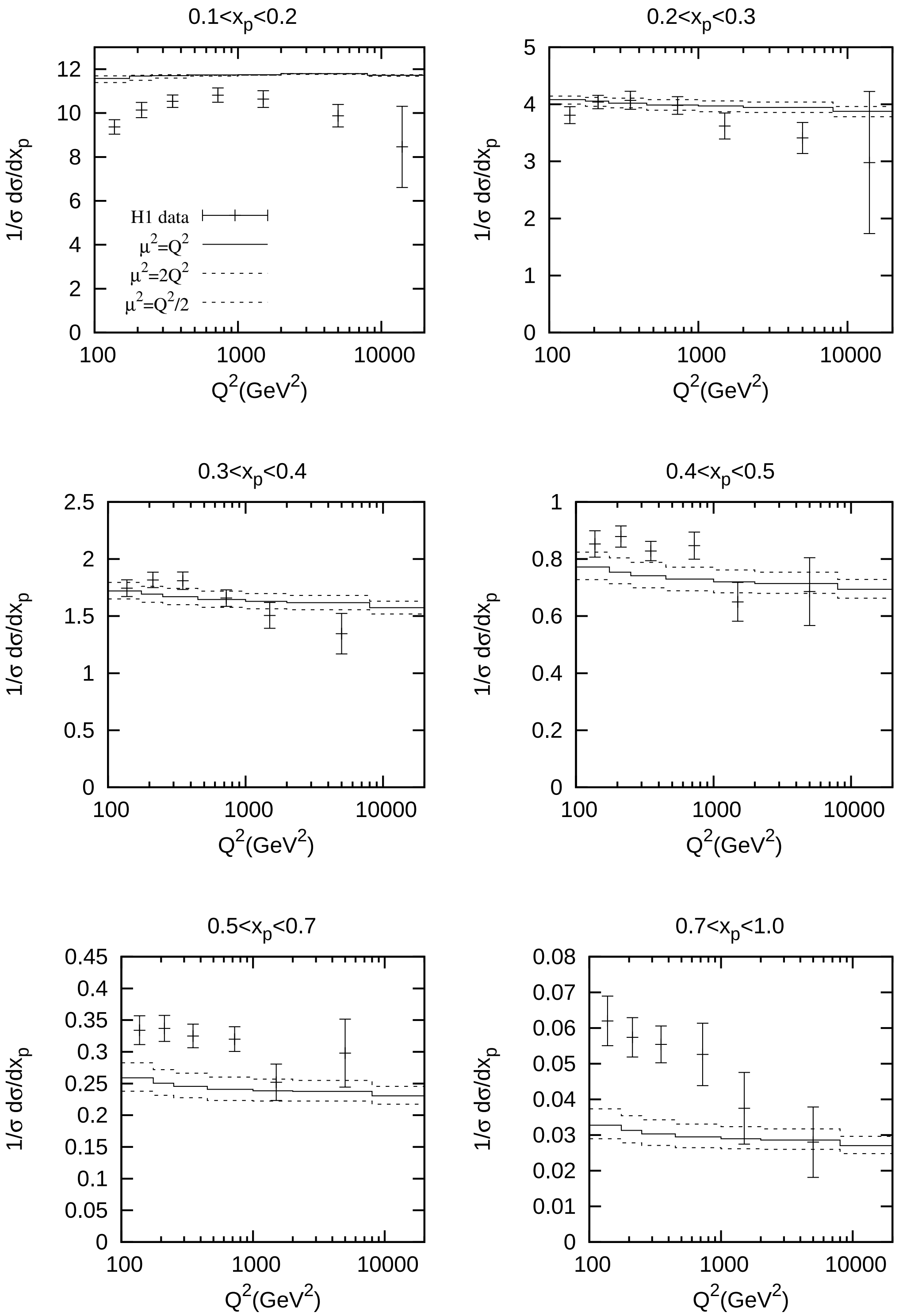

Figure 5.20: As in figure 5.19 but showing the theoretical uncertainty introduced by a change in the scale chosen.

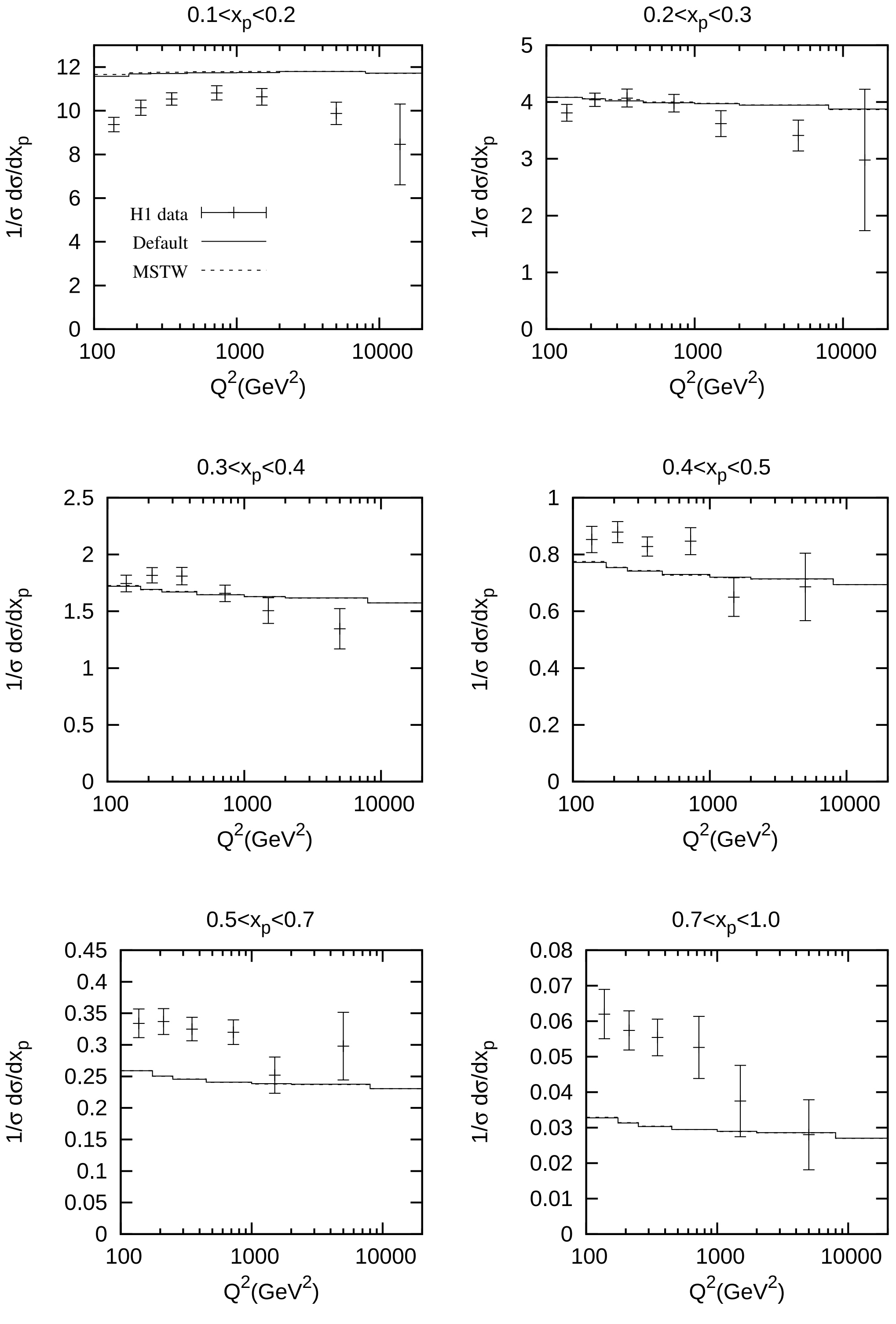

Figure 5.21: As in figure 5.19 but showing the theoretical uncertainty introduced by choosing a different PDF set.

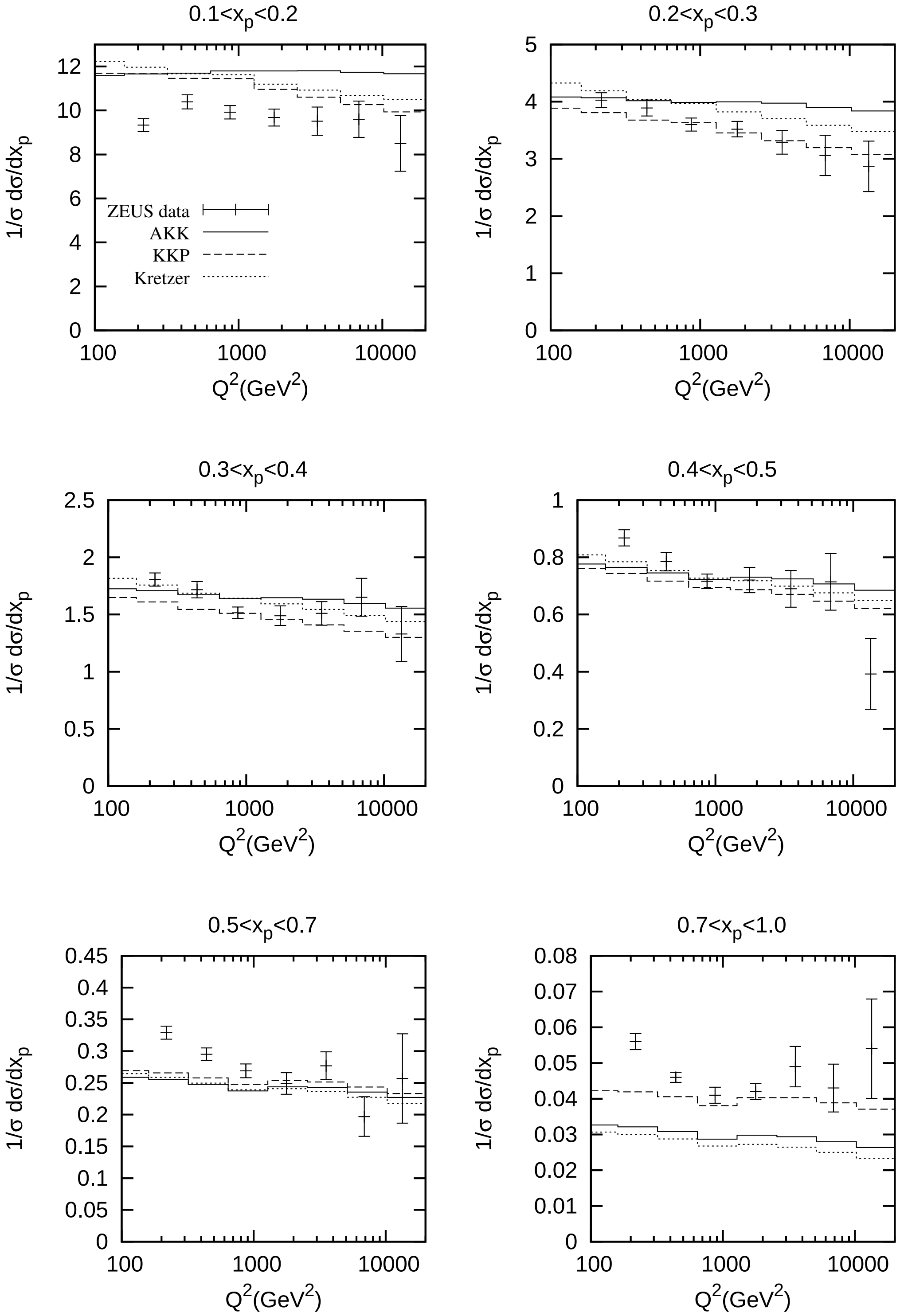

Figure 5.22: Comparisons of theoretical predictions using the AKK, Kretzer and KKP FF sets with the Q^2 distribution from ZEUS [65].

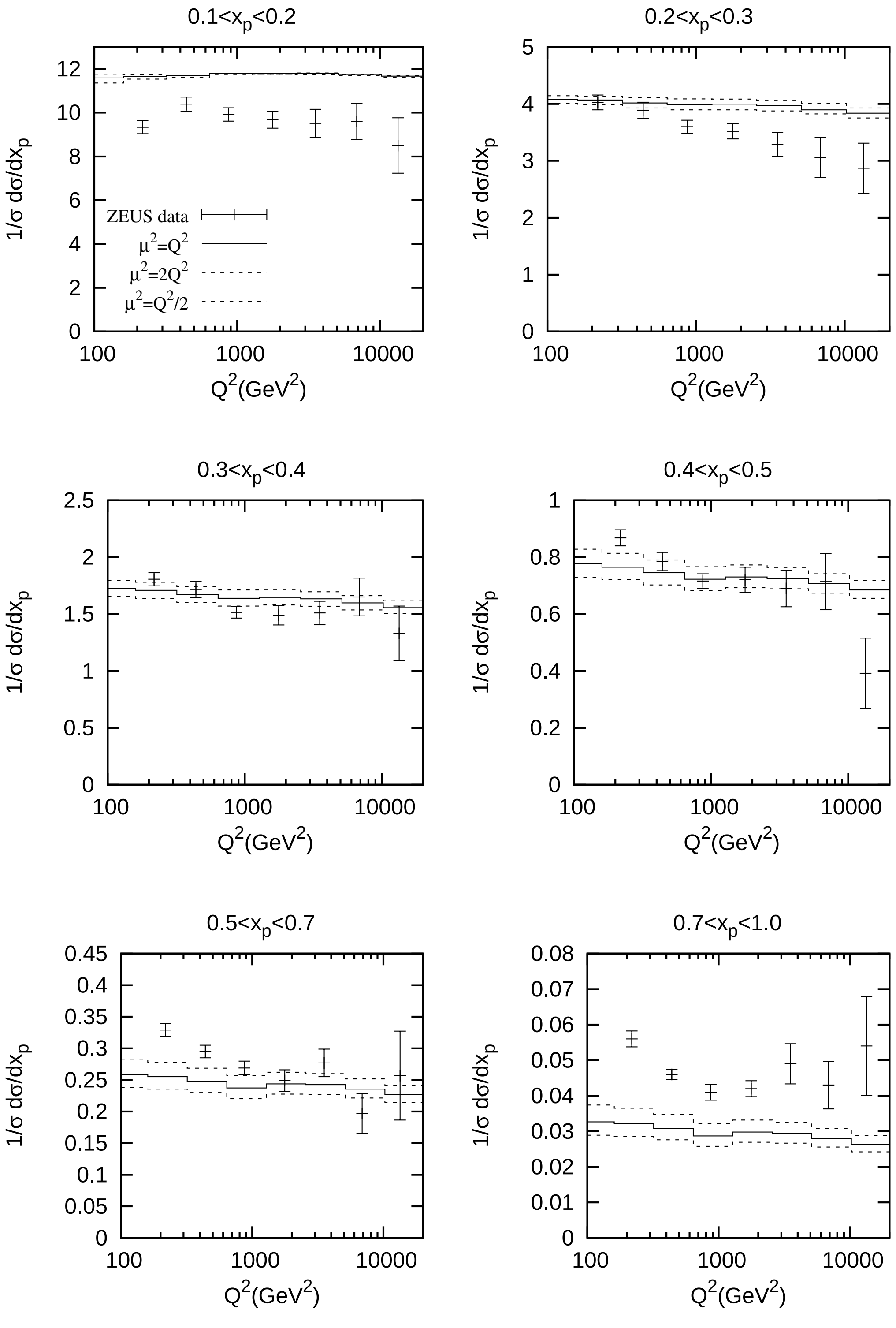

Figure 5.23: As in figure 5.22 but showing the theoretical uncertainty introduced by a change in the scale chosen.

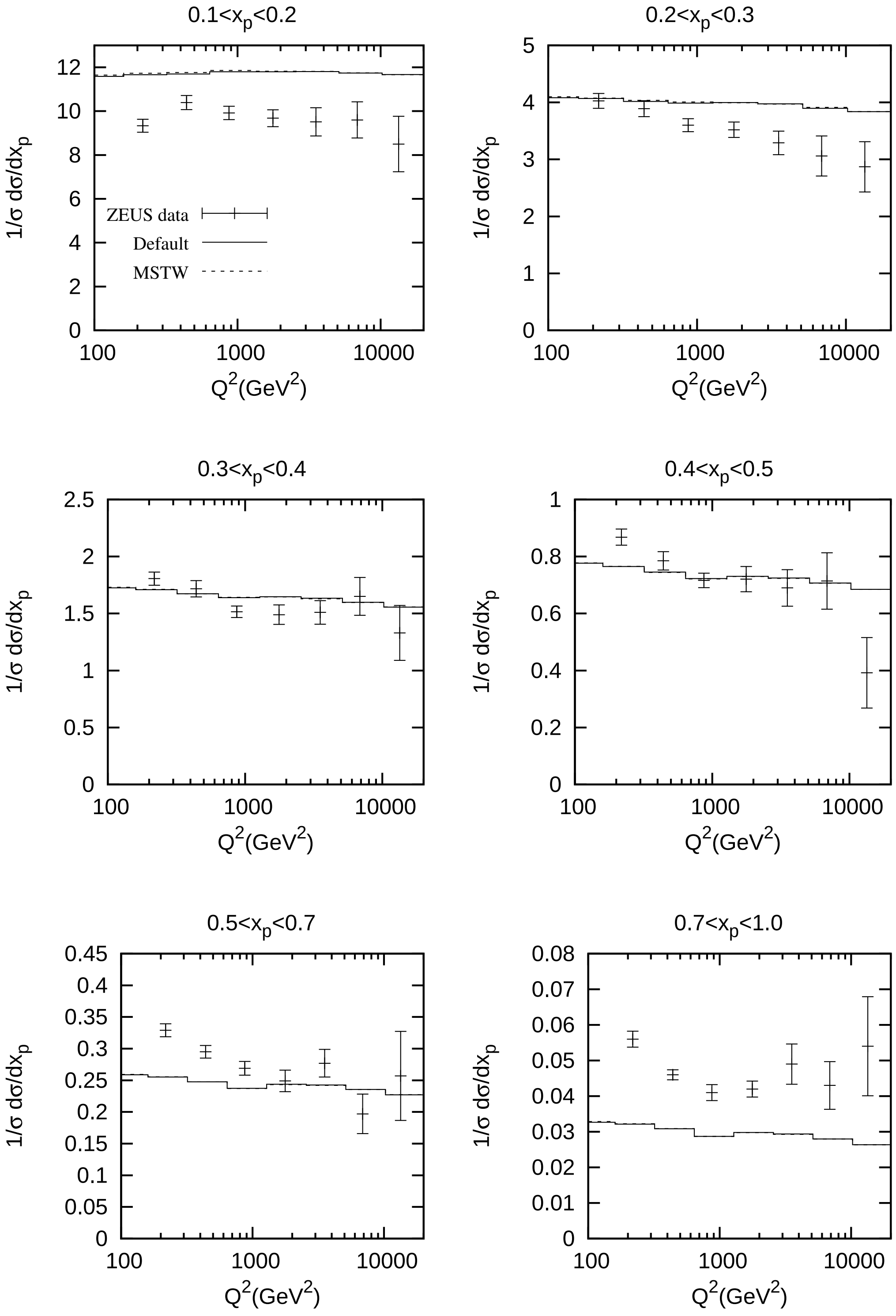

Figure 5.24: As in figure 5.22 but showing the theoretical uncertainty introduced by choosing a different PDF set.

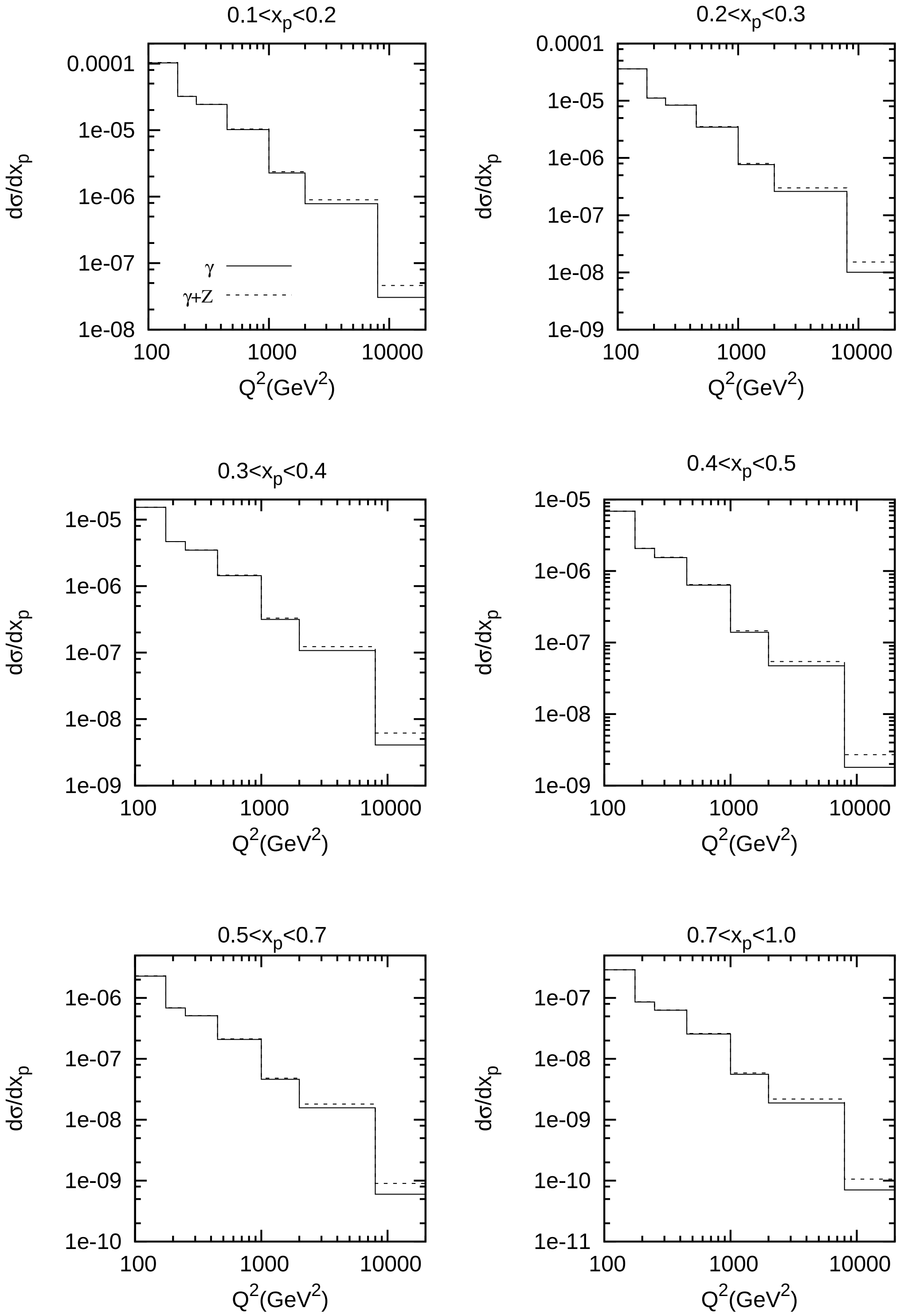

Figure 5.25: Cross section differential in x_p showing the contribution due to the Z boson.

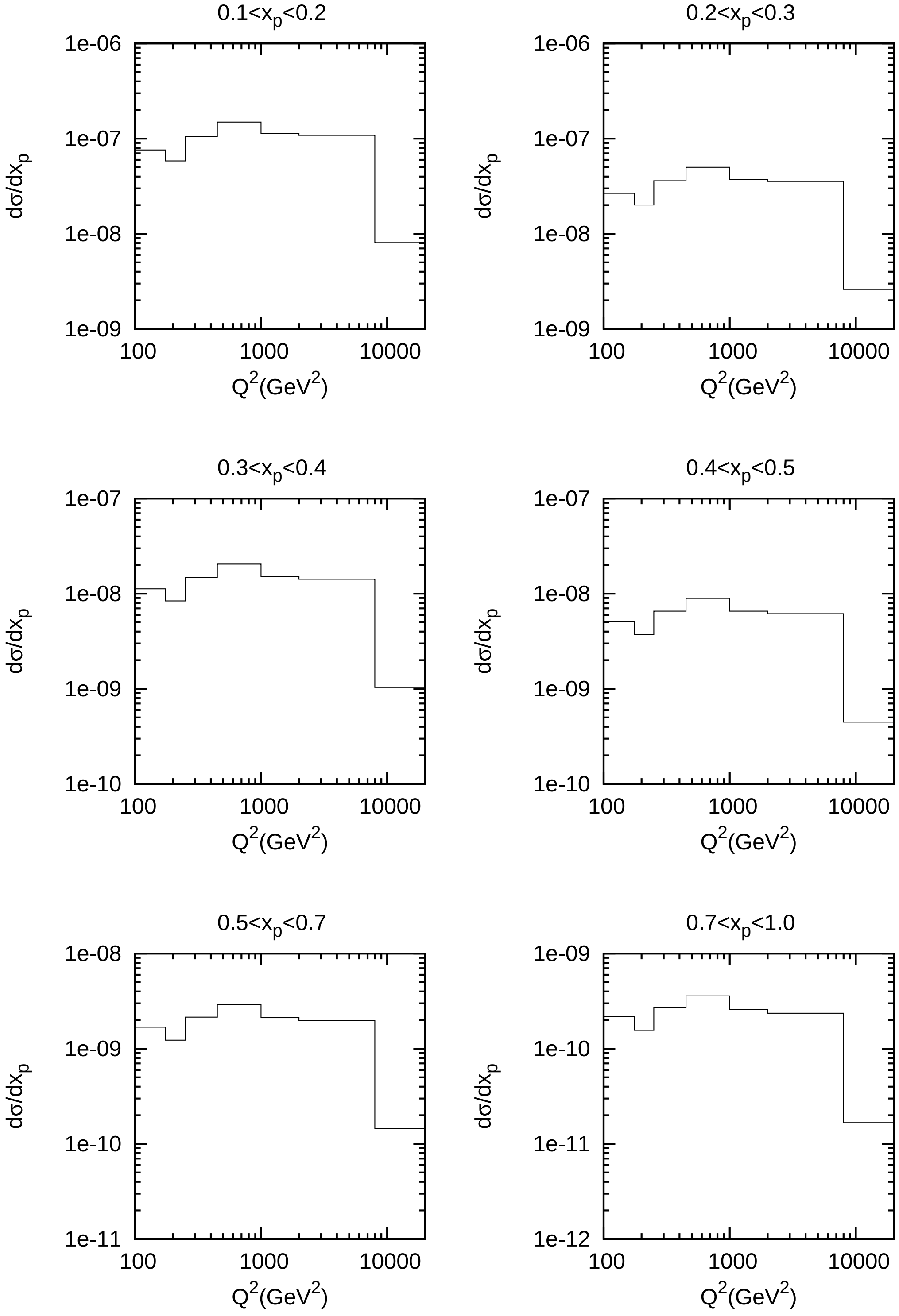

Figure 5.26: Cross section differential in x_p for charged-current DIS.

Chapter 6

Results to second order in α_s

6.1 Inclusive production of π^0 in neutral current DIS

As in the previous case, we work in the $\overline{\text{MS}}$ renormalization and factorization scheme with $n_f = 5$ massless quark flavours. We use CTEQ6.6M NLO set [32] for the proton PDFs and the NLO set of AKK FFs [34] for light charged hadrons ($\pi^\pm$, $K^\pm$, and $p/\overline{p}$). Furthermore, we take the two-loop formula for $\alpha_s^{(n_f)}(\mu_r)$ with asymptotic scale parameter $\Lambda^{(5)}_{\text{QCD}} = 226$ MeV. We approximate the π^0 FFs as

$$D_a^{\pi^0}(x, \mu_f) = \frac{1}{2} D_a^{\pi^\pm}(x, \mu_f), \tag{6.1}$$

where $D_a^{\pi^\pm}$ refers to the sum of the π^+ and π^- mesons which is supported by LEPI data of hadronic Z^0-boson decays [54]. Furthermore, we assume the charged hadrons to be exhausted by the charged pions, charged kaons, protons, and antiprotons, via

$$D_a^{h^\pm}(x, \mu_f) = D_a^{\pi^\pm}(x, \mu_f) + D_a^{K^\pm}(x, \mu_f) + D_a^{p/\overline{p}}(x, \mu_f). \tag{6.2}$$

For simplicity, we identify the renormalization scale μ_r and the initial- and final-state factorization scales, μ_i and μ_f, respectively, and relate them to the characteristic variables Q^2 and p_T^* by setting $\mu_r^2 = \mu_i^2 = \mu_f^2 = Q^2 + (p_T^*)^2$. As in the previous chapter, we will consider variations on this to estimate the theoretical uncertainty in our calculation.

We now compare our theoretical predictions with HERA data on π^0 mesons in the forward region from the H1 Collaboration [66, 67]. These data were taken in DIS of positrons with energy $E_e = 27.6$ GeV on protons with energy $E_p = 820$ GeV in the laboratory frame, so that $\sqrt{S} = 2\sqrt{E_e E_p} = 301$ GeV, during the running periods 1996 and 1996/1997, and correspond to integrated luminosities of 5.8 and 21.2 pb^{-1}, respectively. In Refs. [66, 67], the π^0 mesons were described by their transverse momentum, p_T^*, in the $\gamma^* p$ centre-of-mass (c.m.) frame and by their angle θ with respect to the proton flight direction, their pseudorapidity $\eta = -\ln[\tan(\theta/2)]$, and their energy $E = x_E E_p$ in the laboratory frame. They were detected within the acceptance cuts $p_T^* > 2.5$ GeV or 3.5 GeV, $5^\circ < \theta < 25^\circ$, and $x_E > 0.01$. The DIS phase space was restricted to the kinematic regime defined by $0.1 < y < 0.6$ and $2 < Q^2 < 70$ GeV^2.

We will discuss our comparisons with the cross sections measured differentially in p_T^*, x_B [67] for various Q^2 intervals, and differentially in Q^2 [66]. We present our predictions at NLO and LO compared to these data in figures 6.1-6.8, using the AKK and KKP sets of fragmentation functions. In figures 6.3, 6.4, 6.5 and 6.6, the upper three frames refer to the Q^2 intervals $2 < Q^2 < 4.5$ GeV^2, $4.5 < Q^2 < 15$ GeV^2, and $15 < Q^2 < 70$ GeV^2. In figures 6.7 and 6.8, the upper three frames refer to the Q^2 intervals $2 < Q^2 < 8$ GeV^2, $8 < Q^2 < 20$ GeV^2, and $20 < Q^2 < 70$ GeV^2. In all figures, the minimum-p_T^* cut is $p_T^* > 2.5$ GeV, except for figures 6.7 and 6.8, where it is $p_T^* > 3.5$ GeV. In all figures the dotted lines show the theoretical uncertainty due to the scale variation and the dashed line the LO prediction. Here, in figure 6.1 only, we have shown the prediction with the MSTW set of PDFs, since as we found before, its effect is negligible. The K factors, defined as the NLO to LO ratios of our default predictions, are shown in the lower frames of all figures.

In general all our NLO predictions agree with the data within errors, while they significantly overshoot our default LO predictions. Indeed, the K factors always exceed unity and even reach one order of magnitude at low values of p_T^*, Q^2, or x_B. Not only do the LO predictions disagree with the H1 data in their normalizations, but they also exhibit deviating shapes. On the other hand, under the effect of asymptotic freedom, the K factors approach unity for increasing values of μ_r, i.e. for increasing values of p_T^* and/or Q^2.
There is an obvious explanation for the sizable K factors at low values of μ_r in terms of the different kinematic constraints at LO and NLO. The LO processes are $2 \to 2$, and their cross sections are only sensitive to collinear singularities as $p_T^* \to 0$. On the other hand, processes contributing to the real NLO correction are $2 \to 3$, so that collinear configurations can also arise for finite values of p_T^*. After mass factorization of the corresponding collinear singularities, the finite remainders can be sizable, leading to large NLO corrections.

The theoretical uncertainties in our NLO predictions due to scale variation are not small, especially at low values of p_T^*, Q^2, or x_B, where the K factors themselves are large, which is partly related to the opening of new partonic production channels at NLO, which are still absent at LO. A reduction in the dependence of the scale variation can only be expected to occur at next-to-next-to-leading order (NNLO). Besides the freedom in the choice of the renormalization and factorization scales, there are other sources of theoretical uncertainty, including the variations of the PDF and FF sets. The effect of these can be seen in the different figures by comparing the results for AKK and KKP sets of FFs and the results when the MSTW set was used for the PDFs.

A similar calculation was done in Ref [54], where we were able to compare the analytical expressions involved in the virtual and real corrections and found agreement, as it was mention in the previous chapter. An independent calculation was done in Ref. [68] using a method different from the subtraction method. For this reason we can only perform a numerical comparison with their results. In figures 6.9-6.10 we present our cross sections compared to those in [68] for the same data discussed previously using CTEQ6.6M and KKP and $n_f = 4$. For low Q^2 and low x_B, our cross sections are lower but both still describe the data within the experimental uncertainty. In the case of the p_T^* distributions there is a difference in the cross sections that increases with p_T^* increases. We can investigate this further by removing from both sets of code the kinematic cuts and setting $\alpha_s = 1$, and looking at the distributions in various ranges of the variables in which we are interested. In figur'es 6.12 and 6.13, we show our comparison with the output of the code used in [68], for $2 < Q^2 < 4.5$ GeV^2, $4.5 < Q^2 < 15$ GeV^2, and $15 < Q^2 < 70$ GeV^2, $3.7\times10^{-5} \leq x_B \leq 4.98\times10^{-4}$, $8.31\times10^{-5} \leq x_B \leq 1.66\times10^{-3}$ and $2.7\times10^{-4} \leq x_B \leq 7.76\times10^{-3}$ respectively, and $|\eta| \leq 1.25$ for different bins in p_T^*. At LO, the difference between cross sections is as low as less than 1%, while we find a bigger disagreement for the NLO results. The results from Ref. [68] become lower as p_T* increases, reaching a negative value for $p_T^* > 13$ GeV. This is the case for $2 < Q^2 < 4.5$ GeV^2 and $4.5 < Q^2 < 15$ GeV^2. Whereas for the remaining bin in Q^2, their cross sections never reach negative values. In figures 6.14 and 6.15 we see the same behaviour, this time for $|\eta| \leq 1$ and $|\eta| \leq 10$ respectively. This obvously tells us of a problem in Ref. [68], since it is unphysical to have negative cross sections. Finally, in figures 6.16 and 6.17, we present similar plots to the ones discussed previously but separating some channels that seem to be responsible for the negative values observed before. The channels $q \to g + \bar{q} \to g$ (where we have only written the parton tagged in the PDF and the parton tagged in the FF), seem to have the effect of decreasing the cross section yielding a negative value for large p_T^*. We found good agreement in the channel $g \to g$ where the difference between the two was less than 5%.

In figures 6.18-6.19 we present one last comparison with the results in Ref. [54], using KKP and CTEQ6.6 for the fragmentation functions and parton distributions respectively. The two predictions agree much better than in the comparison with Ref. [68], which is expected since the matrix elements were compared analytically in this case as it was mentioned in chapter 4.

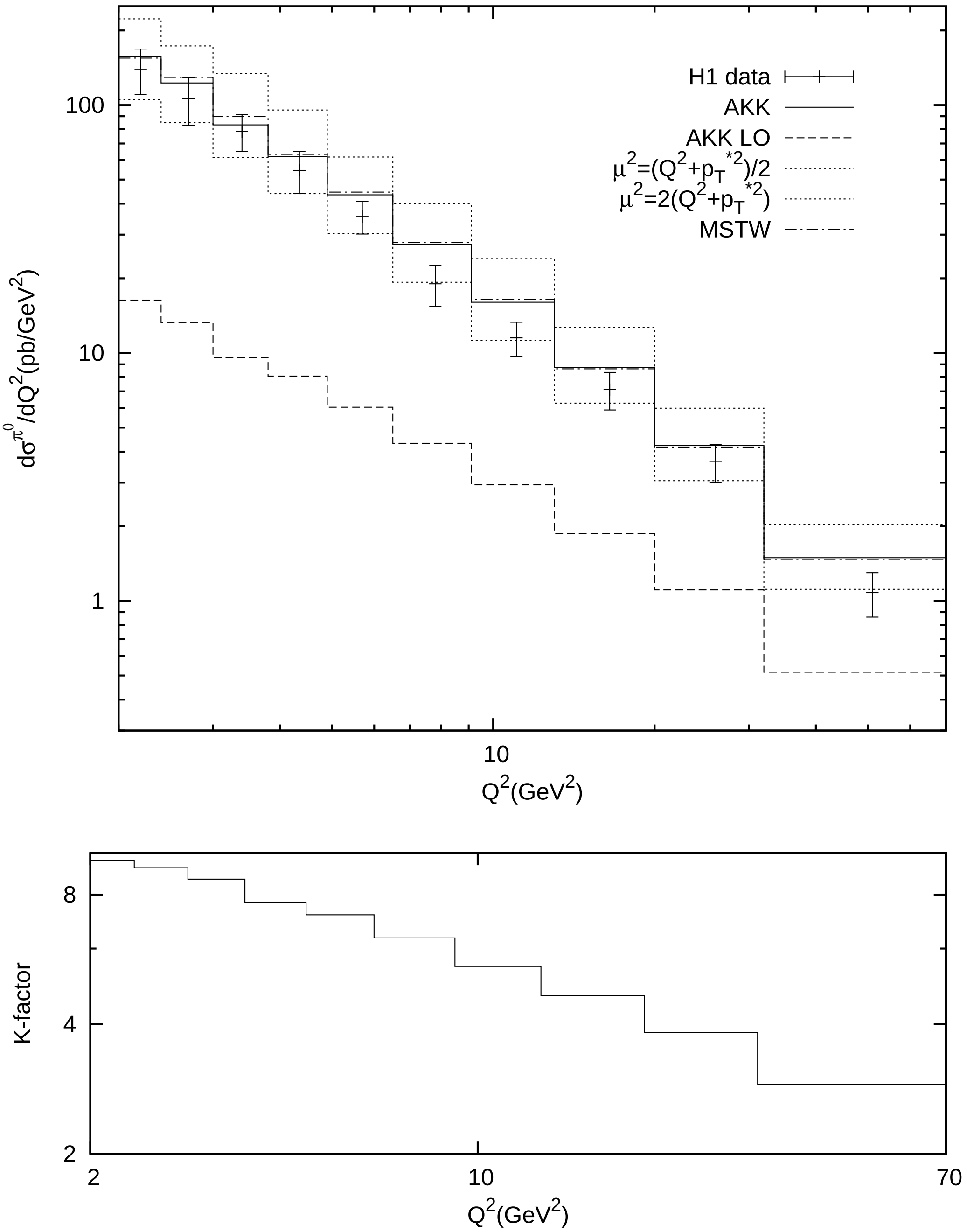

Figure 6.1: $\frac{d\sigma^{\pi^0}}{dQ^2}$ with the AKK set of FFs compared to the experimental data from H1 [66].

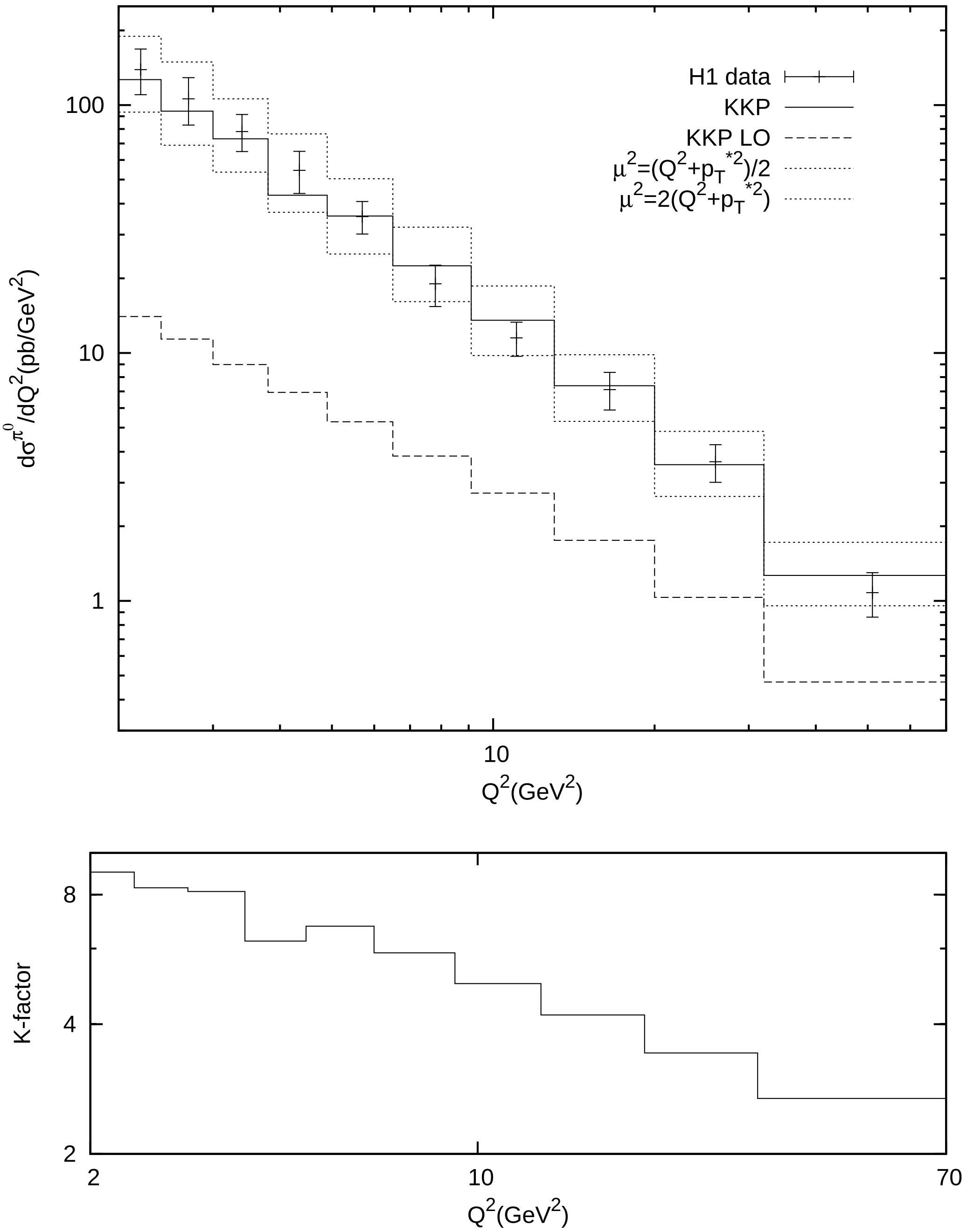

Figure 6.2: $\frac{d\sigma^{\pi^0}}{dQ^2}$ with the KKP set of FFs compared to the experimental data from H1 [66].

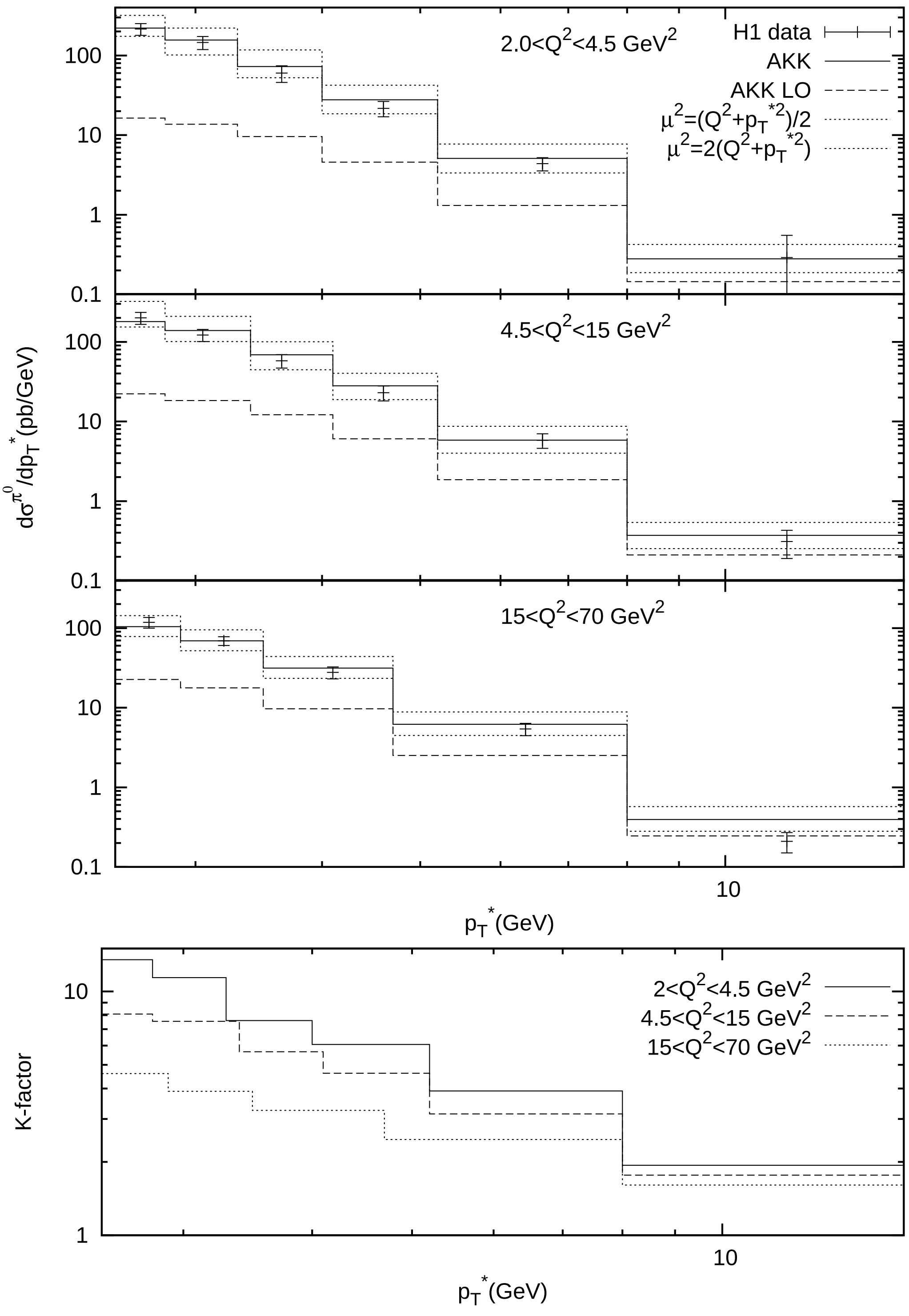

Figure 6.3: $\frac{d\sigma^{\pi^0}}{dp_T^*}$ with the AKK set of FFs compared to the experimental data from H1 [67].

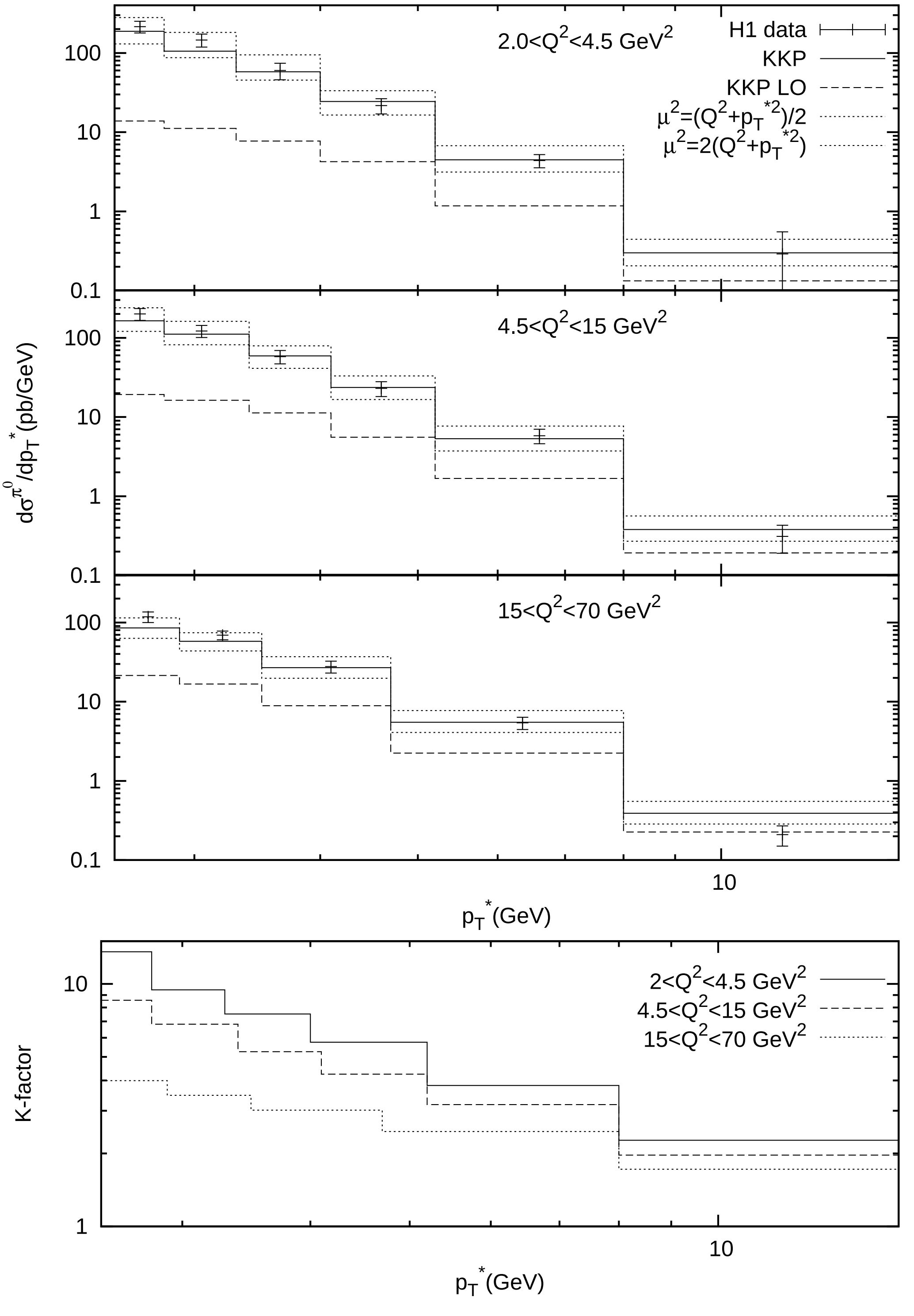

Figure 6.4: $\frac{d\sigma^{\pi^0}}{dp_T^*}$ with the KKP set of FFs compared to the experimental data from H1 [67].

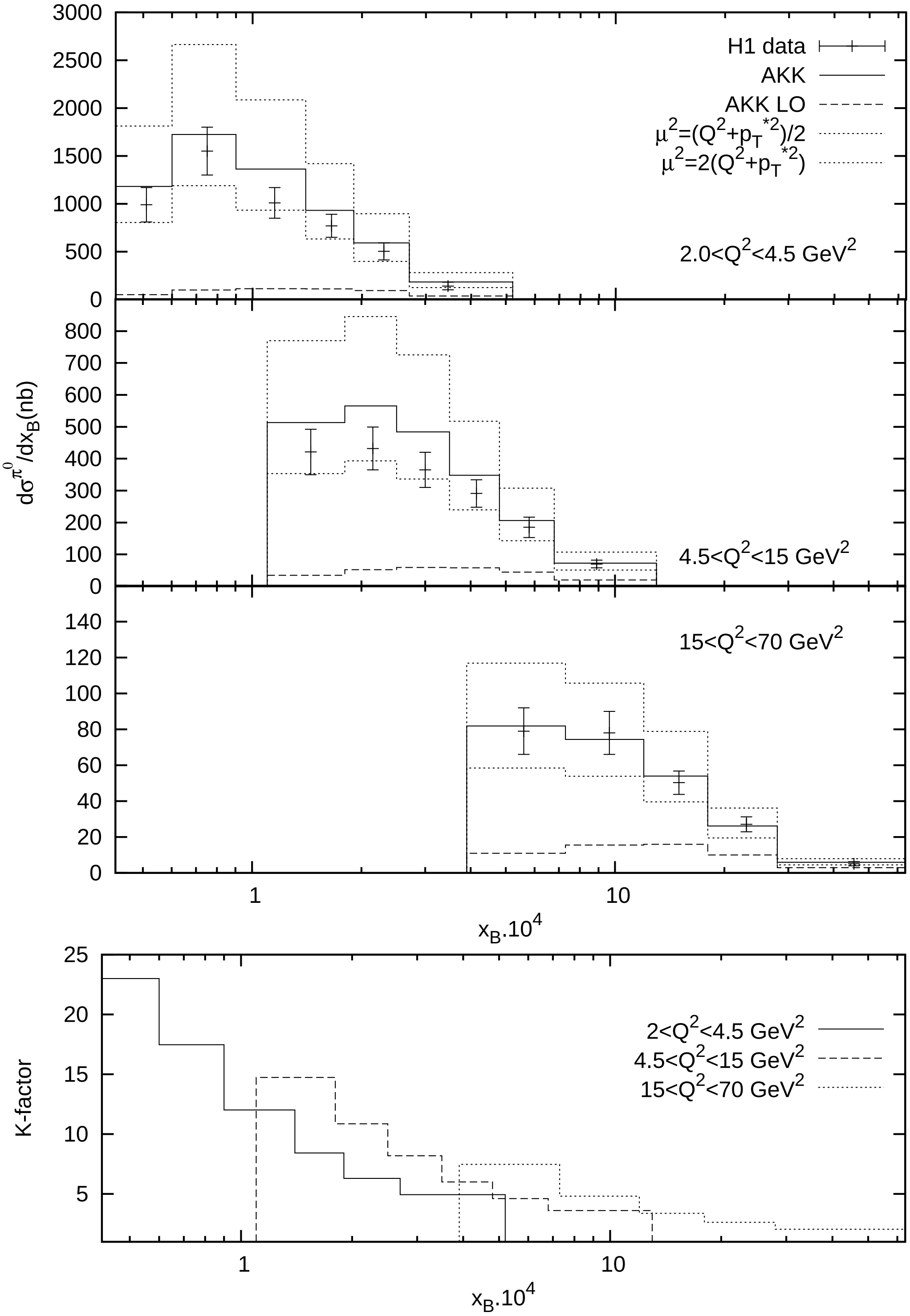

Figure 6.5: $\frac{d\sigma^{\pi^0}}{dx_B}$ with the AKK set of FFs compared to the experimental data from H1 [67].

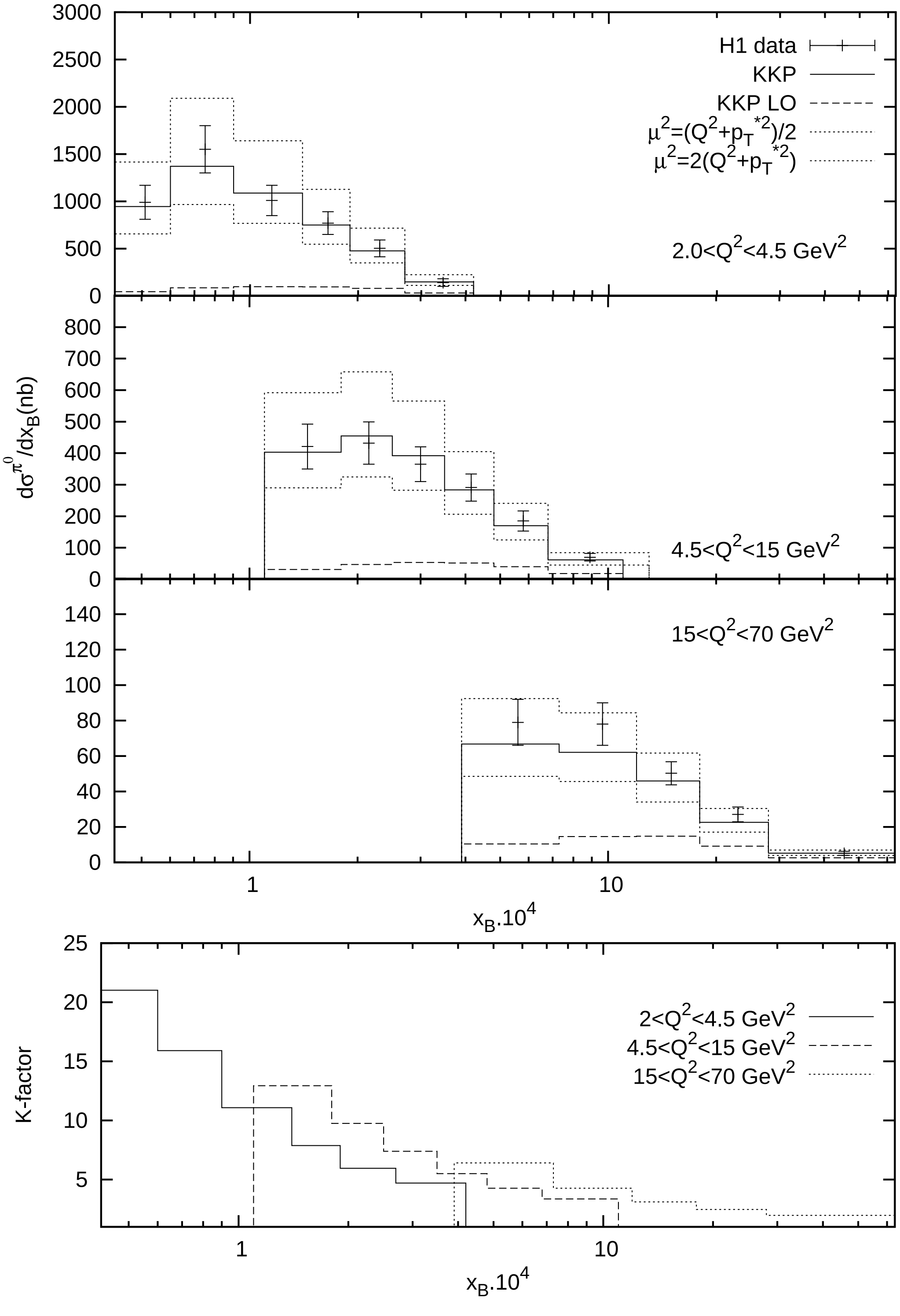

Figure 6.6: $\frac{d\sigma^{\pi^0}}{dx_B}$ with the KKP set of FFs compared to the experimental data from H1 [67].

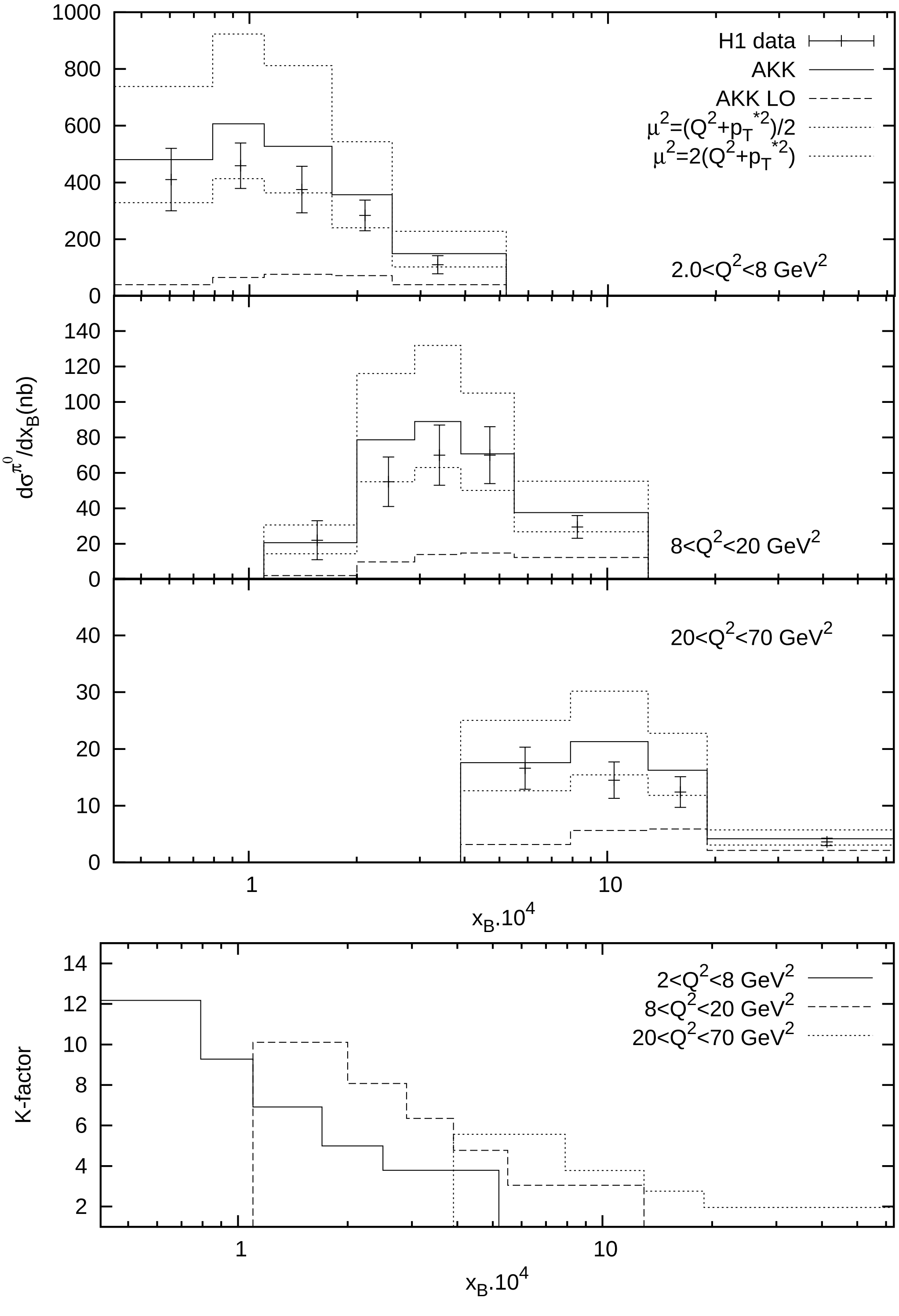

Figure 6.7: $\frac{d\sigma^{\pi^0}}{dx_B}$ with the AKK set of FFs compared to the experimental data from H1 [67].

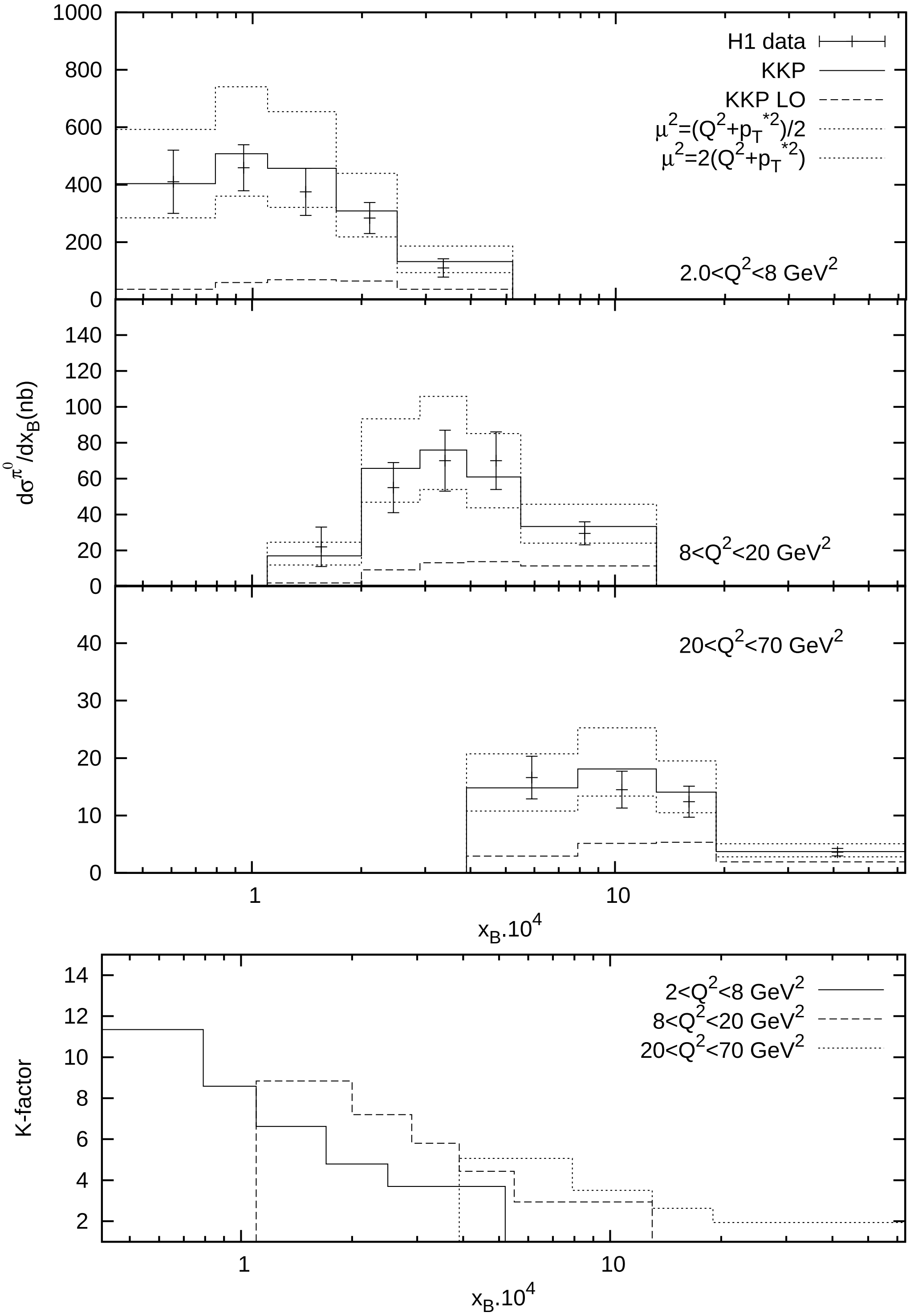

Figure 6.8: $\frac{d\sigma^{\pi^0}}{dx_B}$ with the KKP set of FFs compared to the experimental data from H1 [67].

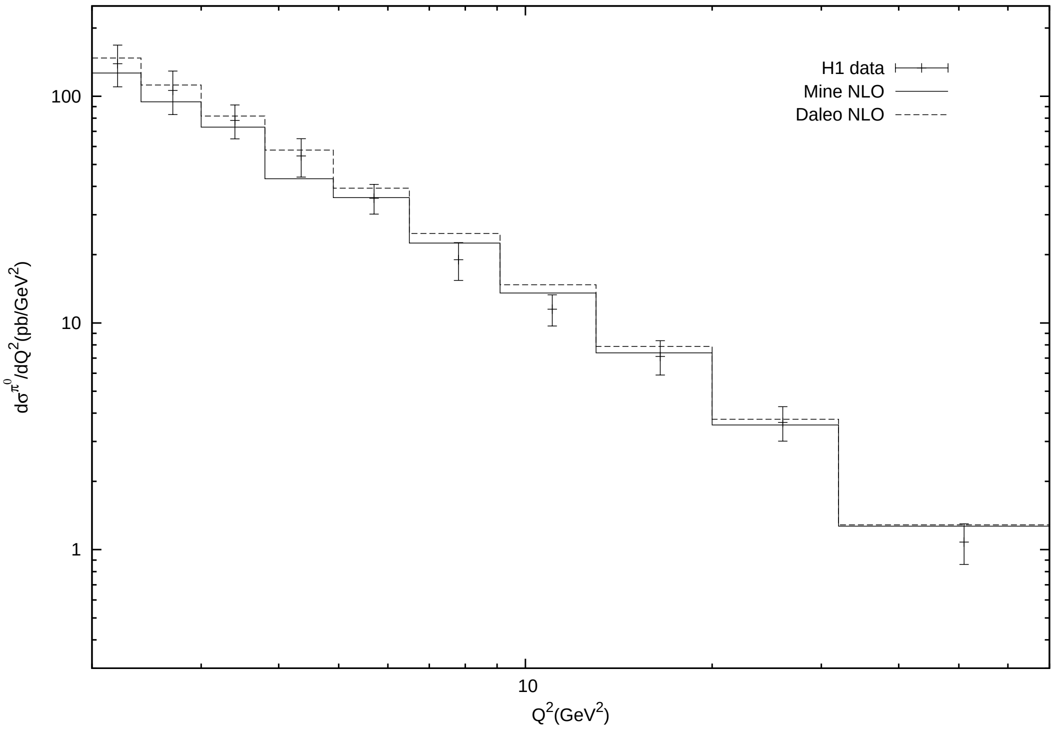

Figure 6.9: $\frac{d\sigma^{\pi^0}}{dQ^2}$ comparing our results and the ones obtained using the code by Daleo et al. [68], for the same kinematic region as in the H1 data discussed using KKP, CTEQ6.6 and $n_f = 4$.

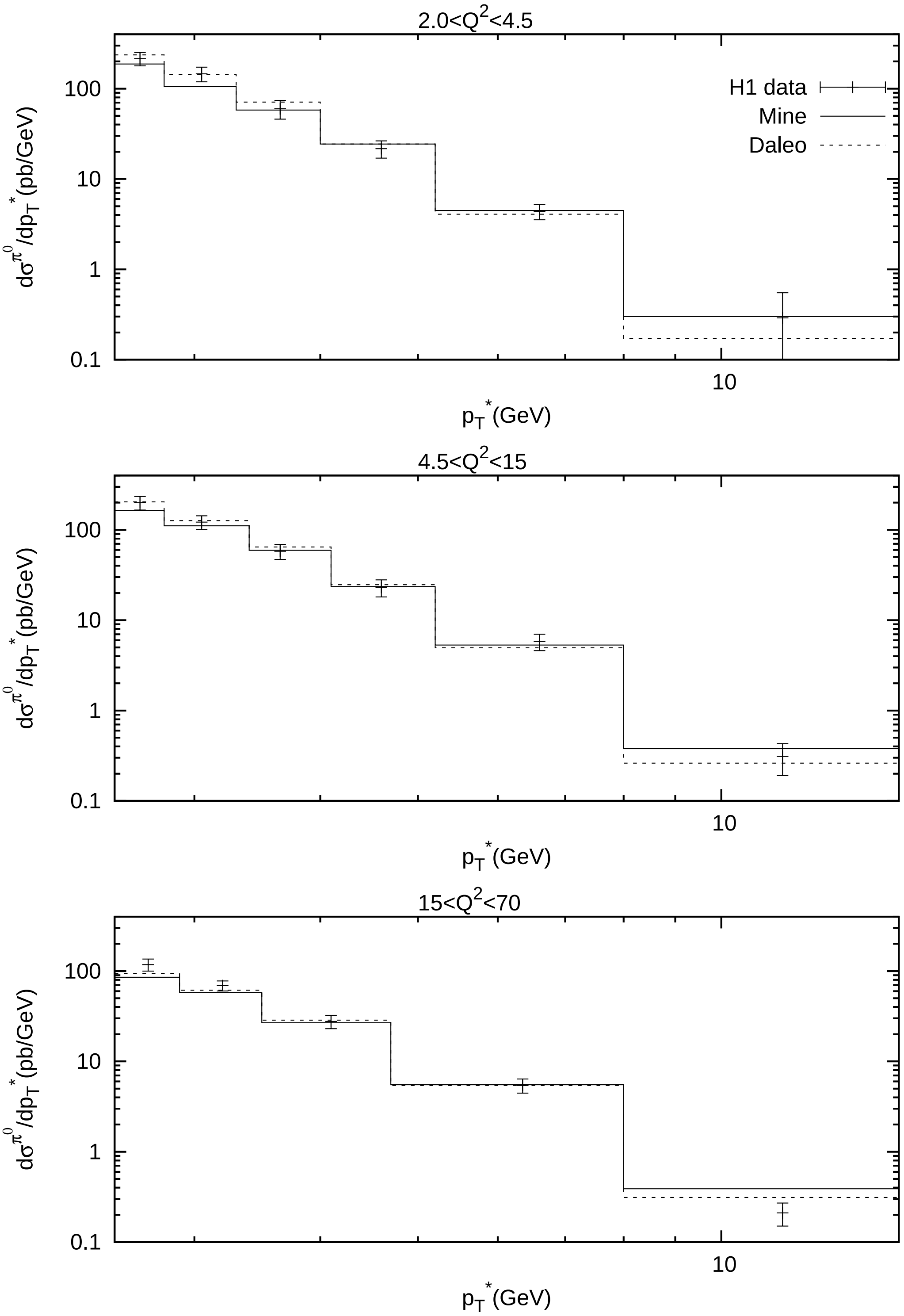

Figure 6.10: $\frac{d\sigma^{\pi^0}}{dp_T^*}$ comparing our results and the ones obtained using the code by Daleo et al. [68], for the same kinematic region as in the H1 data discussed using KKP, CTEQ6.6 and $n_f = 4$.

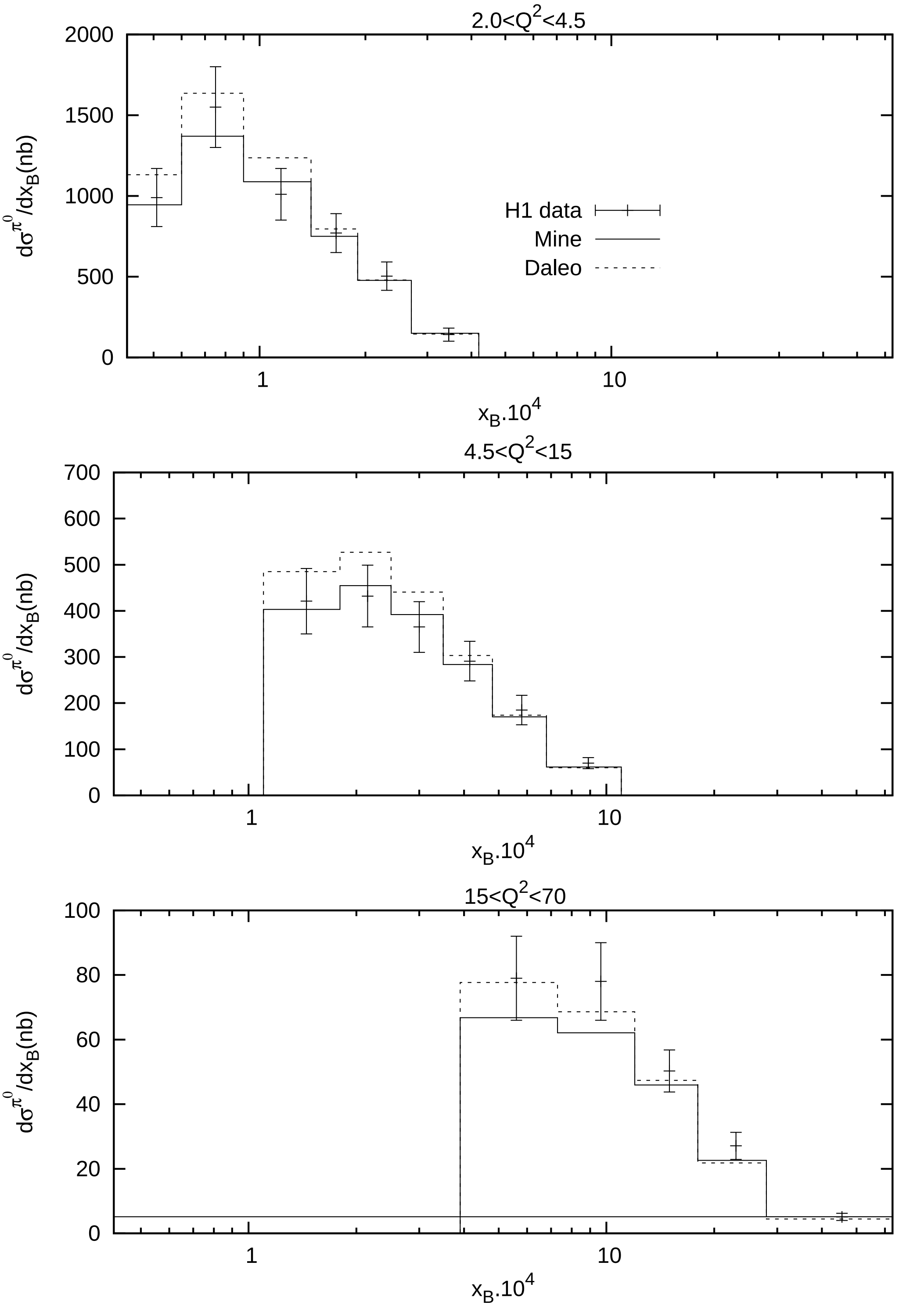

Figure 6.11: $\frac{d\sigma^{\pi^0}}{dx_B}$ comparing our results and the ones obtained using the code by Daleo et al. [68], for the same kinematic region as in the H1 data discussed using KKP, CTEQ6.6 and $n_f = 4$.

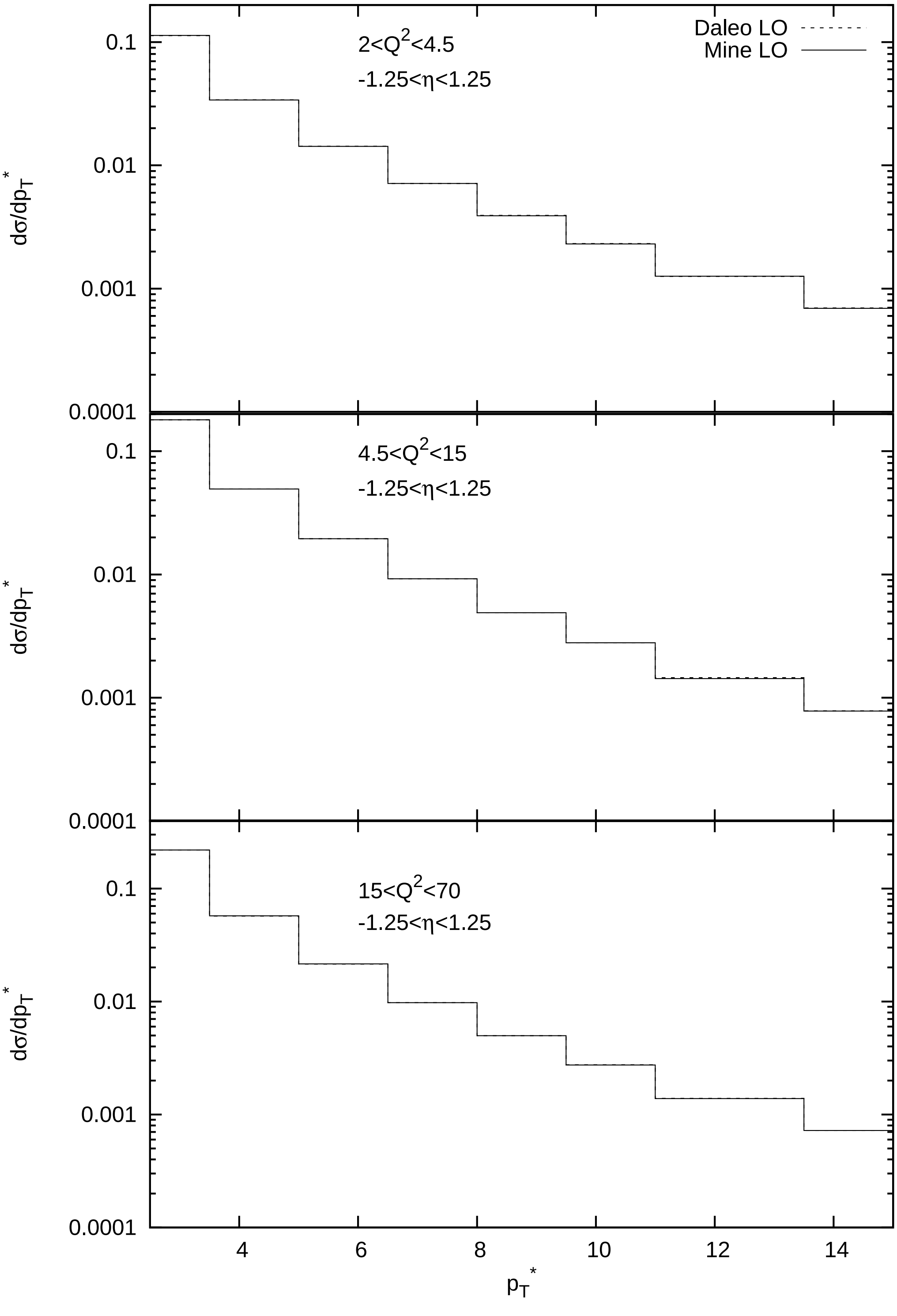

Figure 6.12: Comparison with the paper by Daleo et al. at LO

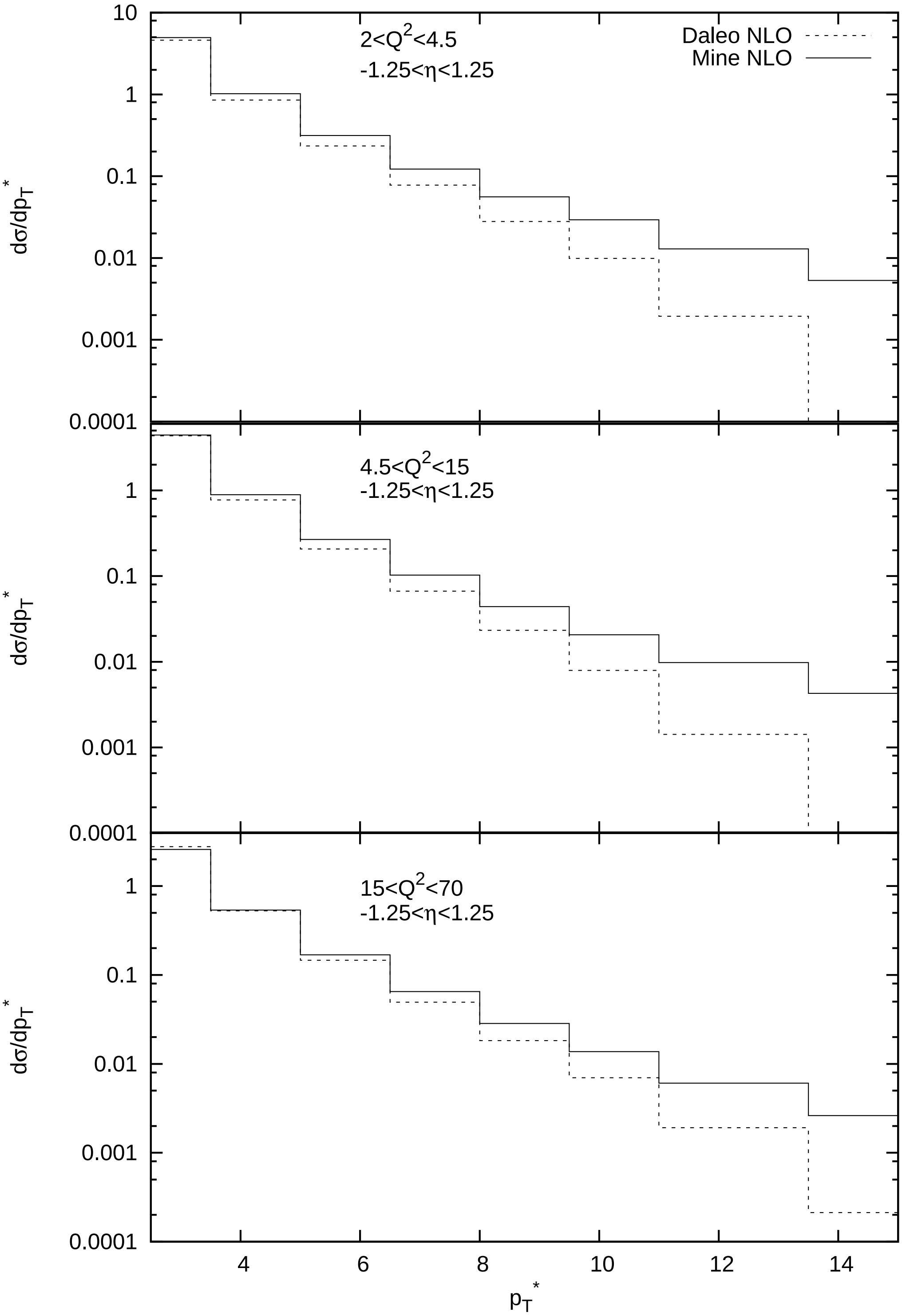

Figure 6.13: Comparison with the paper by Daleo et al. at NLO

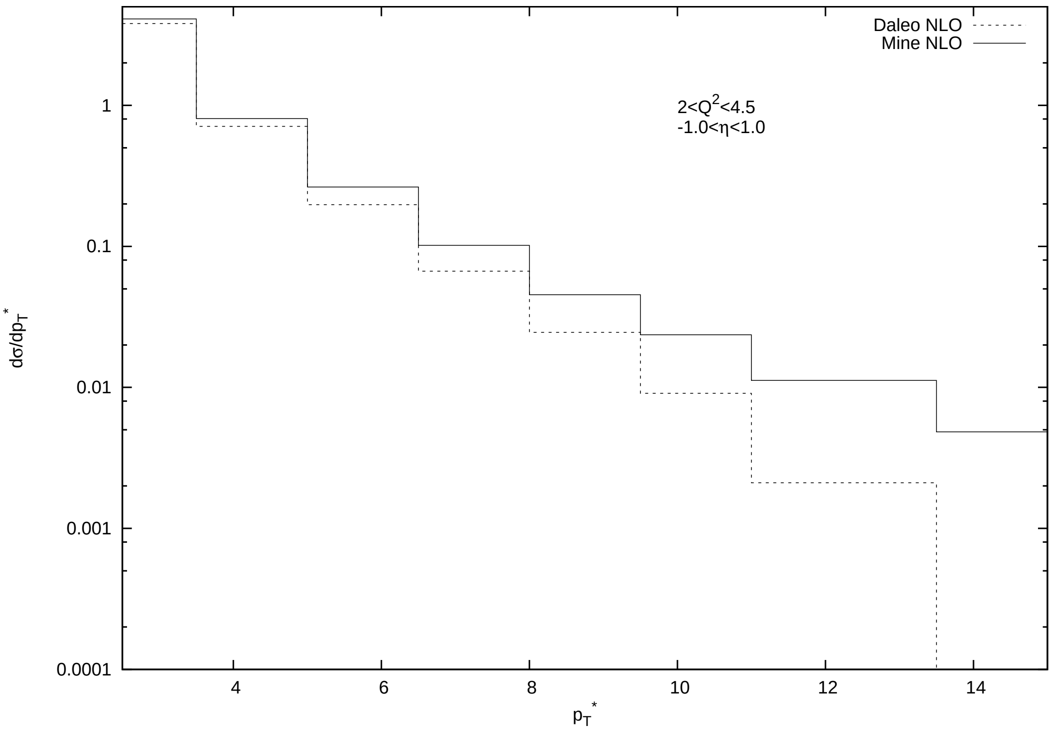

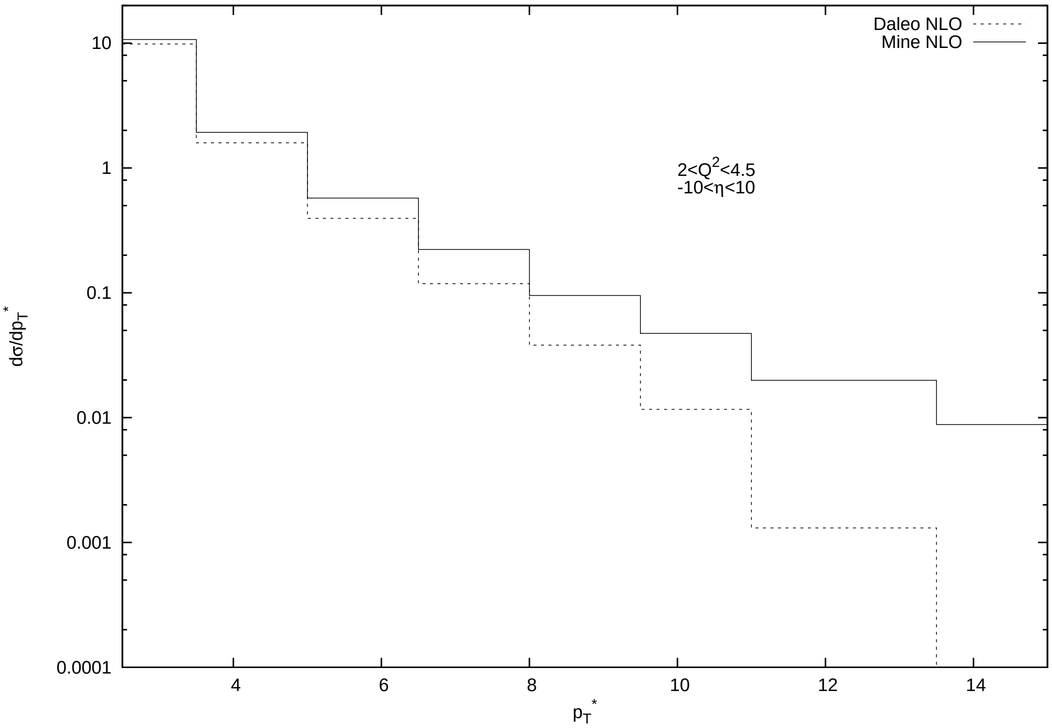

Figure 6.14: Comparison with the paper by Daleo et al. at NLO for different ranges of η.

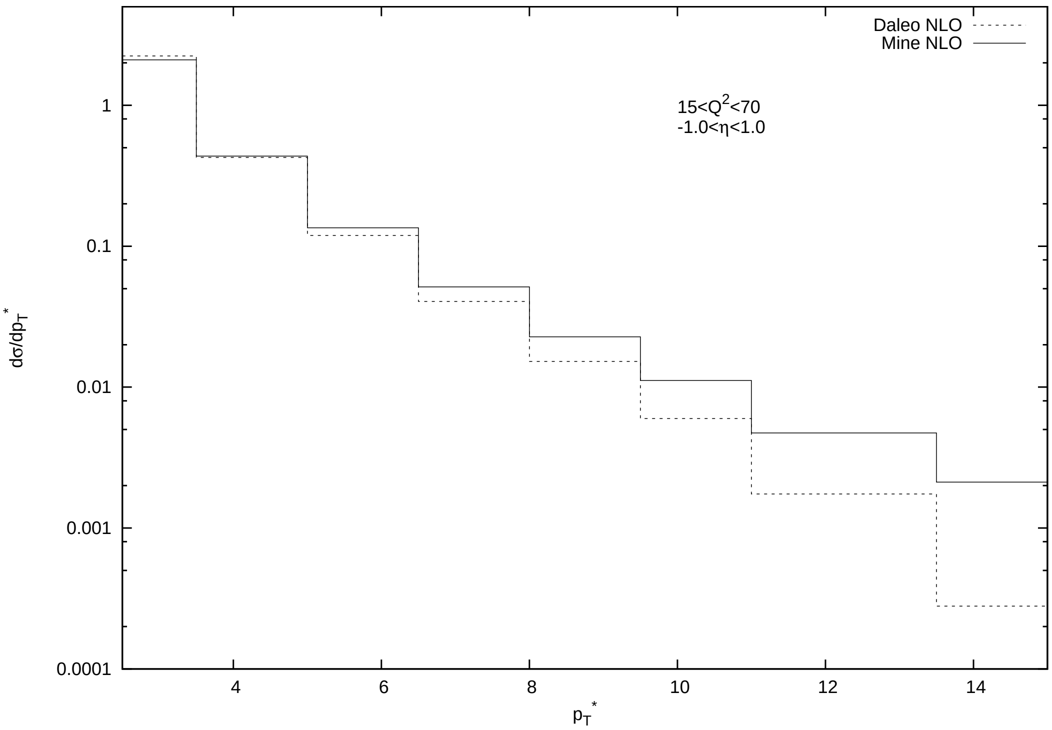

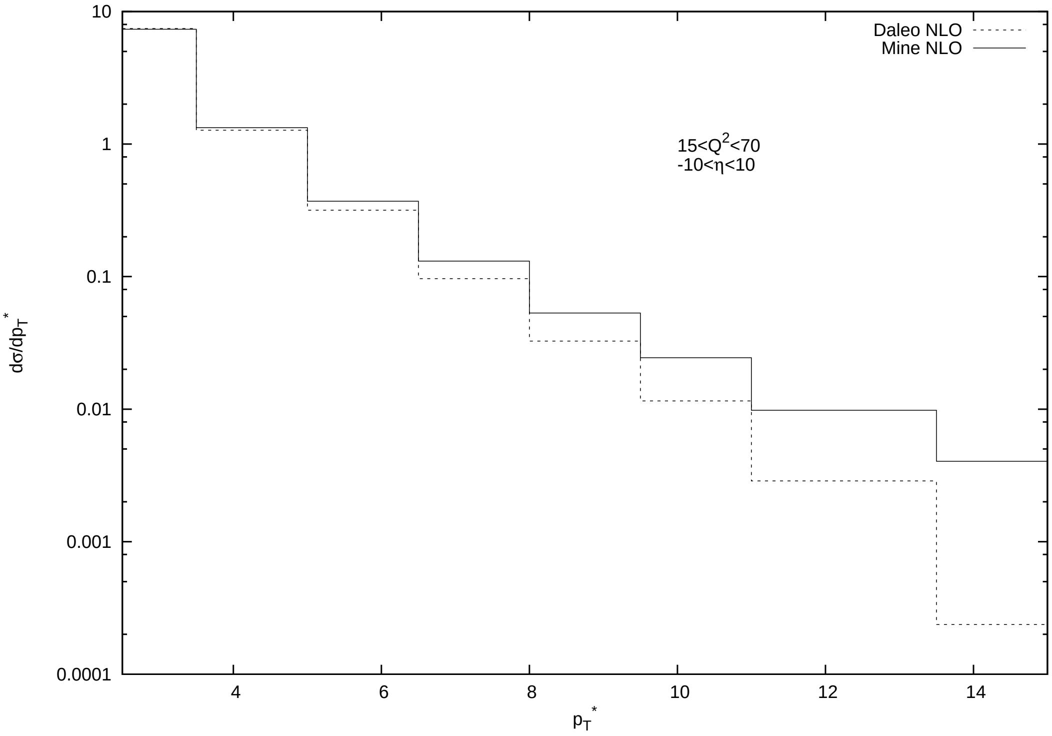

Figure 6.15: Comparison with the paper by Daleo et al. at NLO for different ranges of η.

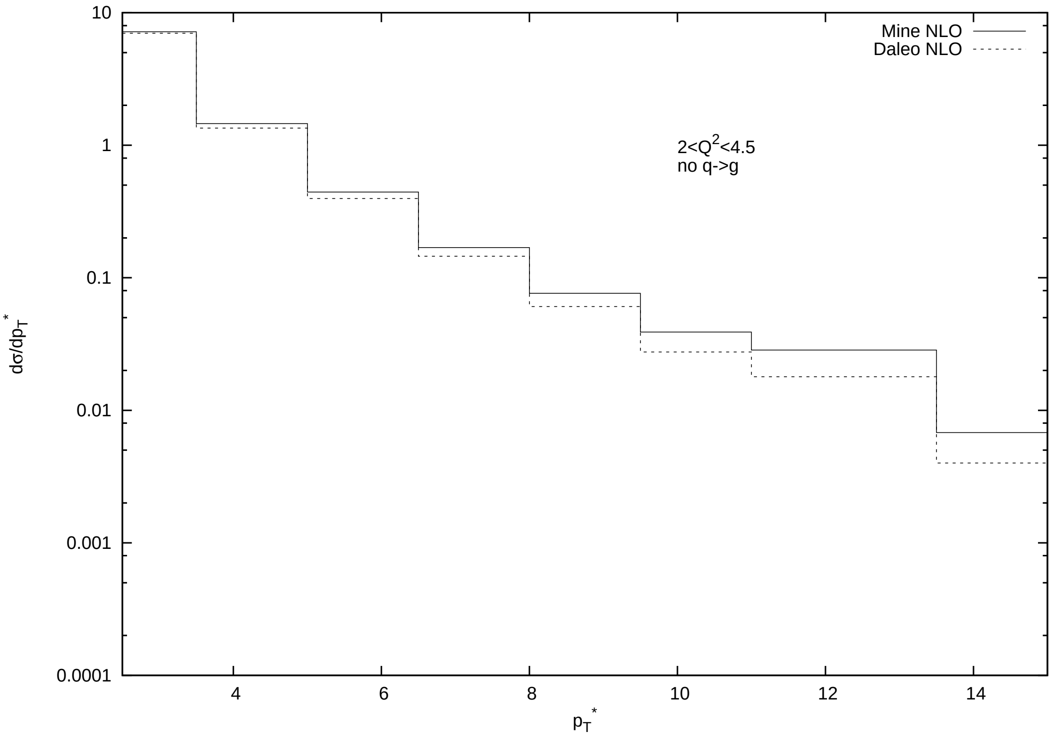

Figure 6.16: Comparison with the paper by Daleo et al. at NLO neglecting channels with $q \rightarrow g$.

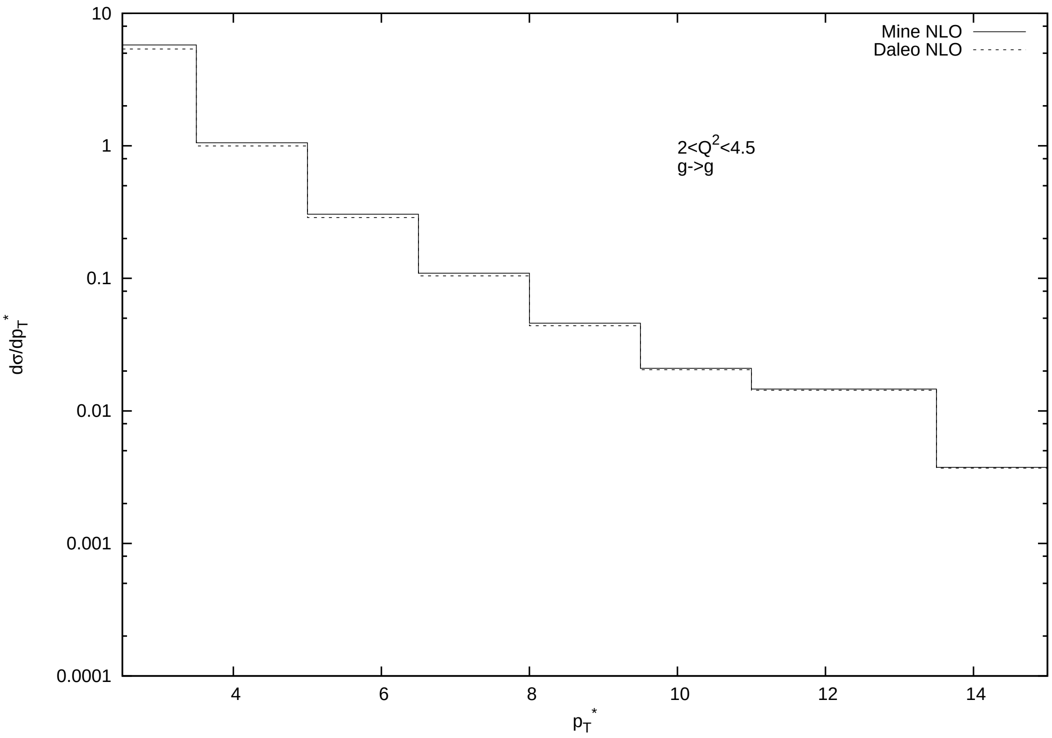

Figure 6.17: Comparison with the paper by Daleo et al. at NLO neglecting all channels except the $g \rightarrow g$ channel.

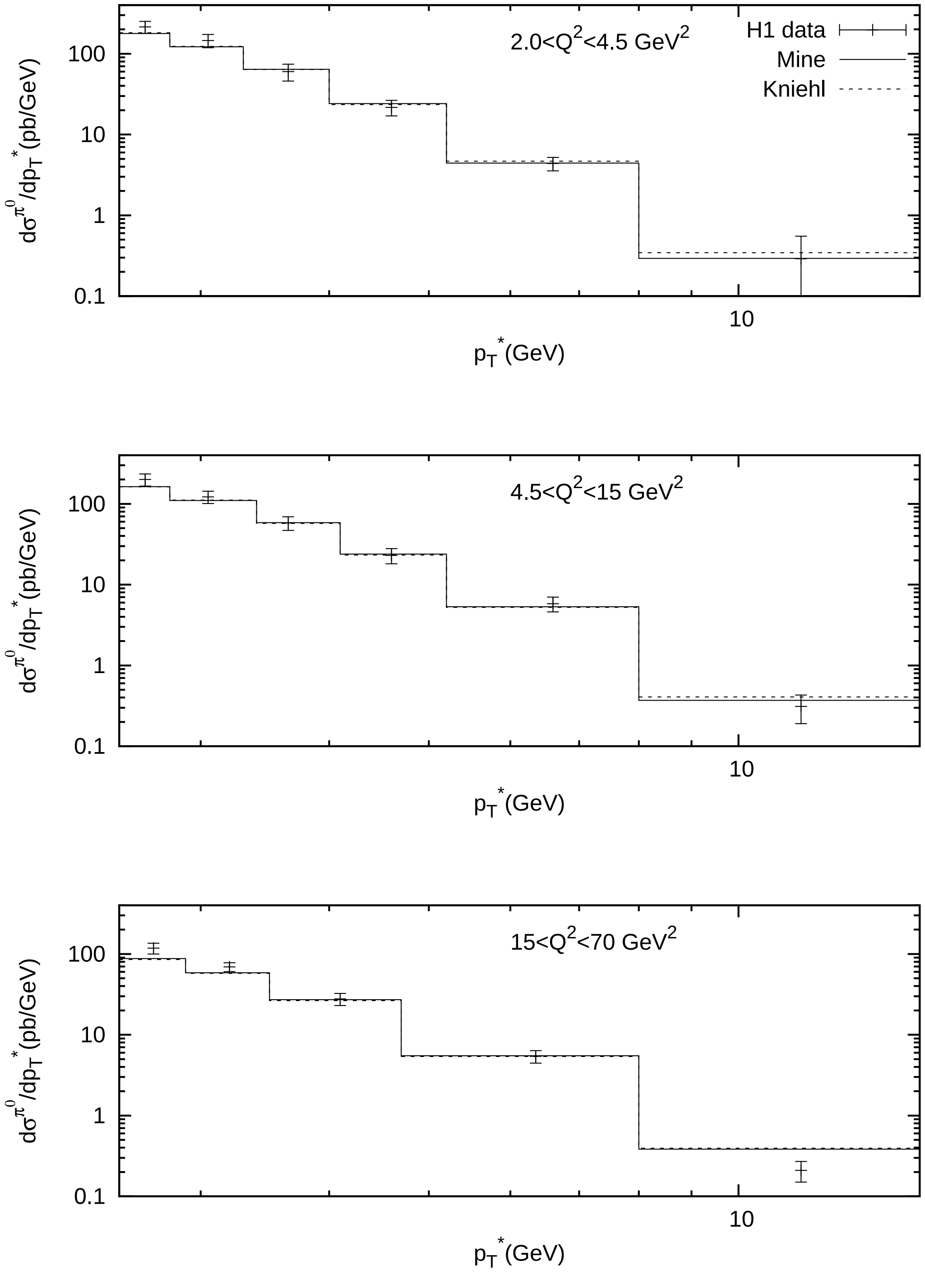

Figure 6.18: $\frac{d\sigma^{\pi^0}}{dp_T^*}$ comparing our results and the ones in Ref. [54], for the same kinematic region as in the H1 data discussed.

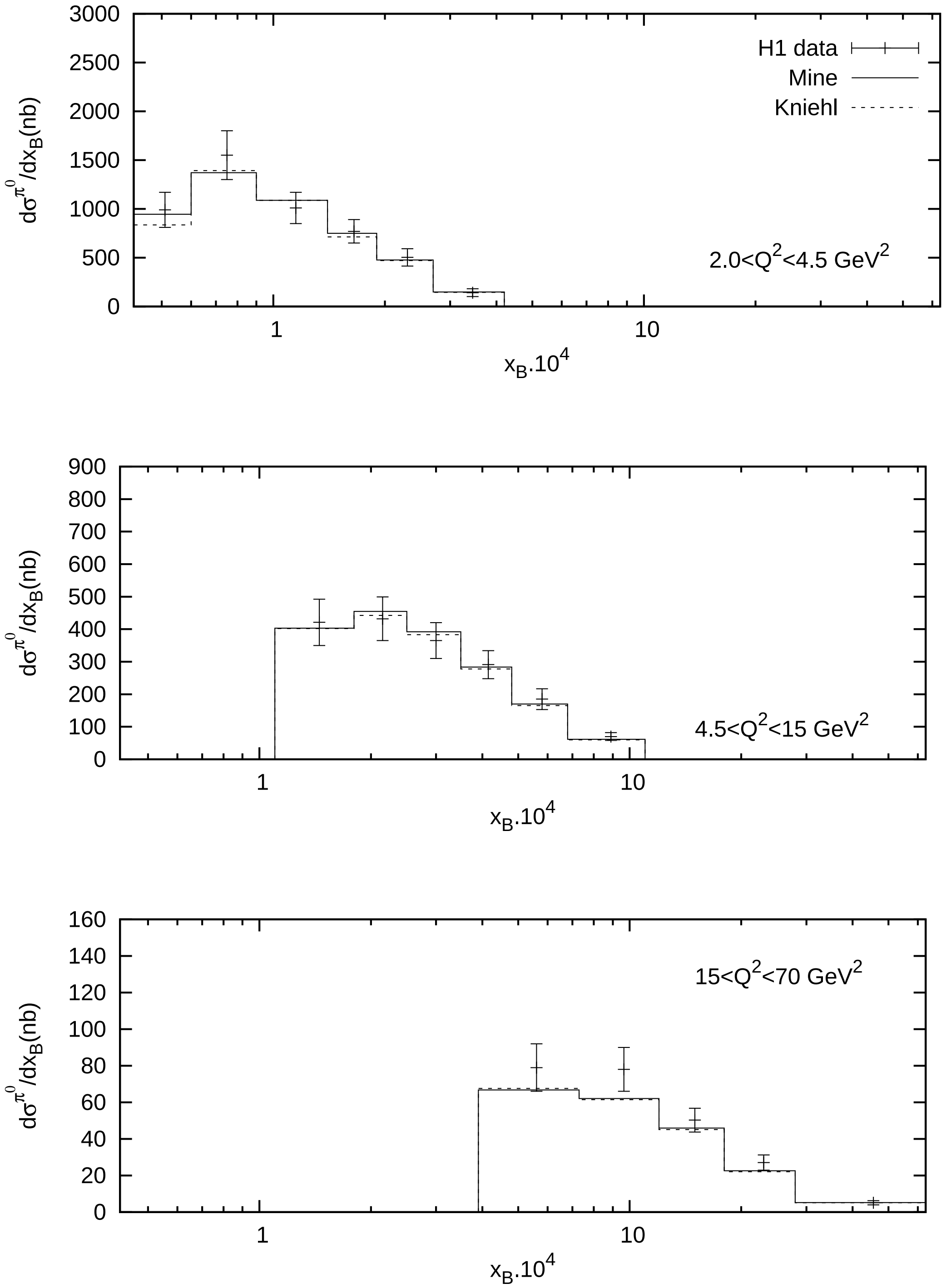

Figure 6.19: $\frac{d\sigma^{\pi^0}}{dx_B}$ comparing our results and the ones in Ref. [54], for the same kinematic region as in the H1 data discussed.

6.2 Inclusive production of $D^{*\pm}$ in neutral current DIS

In the same fashion as before, we can also make a comparison with data from $D^{*\pm}$ production by the H1 collaboration. Although in this work we have made a massless calculation, it is possible to use a set of fragmentation functions describing the final state $D^{*\pm}$ and use the same code to produce cross sections and compare those to the data. For this purpose we have used two sets of FFs, the KKKS08 [69] and the KKS05 [70] sets.

First, we will compare our predictions to the data in [71], where the DIS region covered was $2 \leq Q^2 \leq 100$ GeV^2 and $0.05 \leq y \leq 0.7$. As usual, we take CTEQ6.6M NLO as our default PDF set, and the scale $\mu_r^2 = \mu_i^2 = \mu_f^2 = Q^2 + (p_T^*)^2$. These data have some other kinematic cuts such as $p_T \geq 1.5$ GeV, $|\eta| \leq 1.5$, and most importantly in our calculation, $p_T^* \geq 2$ GeV, since our calculation is only valid for finite values of p_T^* i.e. the value of p_T^* can not go all the way down to zero, it must have a cut.
Our results are presented in figures 6.20, 6.22 and 6.24 for the results with KKKS08 and in figures 6.21, 6.23 and 6.25 for the results with KKKS05. The cross sections were calculated differentially in Q^2, p_T and x_B, considering the kinematic cuts mentioned in the previous paragraph and as usual, we display the theoretical uncertainty by a variation in the scale used. Here our NLO results describe the data quite well for both sets of FFs, except for high x_B and Q^2 where our predictions overshoot the data. The LO predictions do not describe the data and the K factor is found to be around 2 for all cross sections. Furthermore, the results for both sets of FFs are rather similar, with small deviations between them at high p_T.

More recent precise data was analyzed recently by the H1 collaboration for a wider range in Q^2 and p_T. At low Q^2, the kinematic region in Ref. [72] was $5 \leq Q^2 \leq 100$ GeV^2, $0.02 \leq y \leq 0.7$, $p_T \geq 0.8$ GeV, $|\eta| \leq 1.9$ and $p_T^* \geq 2$ GeV. Our results for this comparison are shown in figures 6.26-6.31, where we have calculated the differential cross section in Q^2, p_T and p_T^* for the two available sets of fragmentation functions as we did for the other set of data. Our results here also agree with the data within the error for all cross sections except at low values of p_T, where our calculation is not reliable.

The last set of data we can use for comparison is for high Q^2, and can be found in Ref. [73]. The kinematic range here is $100 \leq Q^2 \leq 1000$ GeV^2, $0.02 \leq y \leq 0.7$, $p_T \geq 1.5$ GeV, $|\eta| \leq 1.5$ and $p_T^* \geq 2$ GeV. In this case our predictions do not describe the data very well. Although they all present the behaviour shown by the data, our values are larger than the data for all four cross sections shown, as functions of Q^2, p_T, x_B and p_T^* (figures 6.32-6.35). We have carried out this calculation for two different sets of scales, one with $\mu^2 = Q^2 + p_T^{*2}$ and the other with $\mu^2 = Q^2 + m_c^2$, obtaining similar results in both. The reason for this disagreement might be connected with the fact that the measurements are made in the HERA laboratory system and to compare with our calculations a transformation of the data to the $\gamma^* p$ c.m. system was necessary.

6.3 Charged and neutral current contributions

Unfortunately, there are no data available for single hadron production at high enough Q^2 for us to see any effect caused by the Z boson in this comparisons. However, we can extrapolate the kinematic region to high Q^2. In figure 6.36 we can see the cross section with and without a contribution from the Z boson, and the ratio between these cross sections. At very high Q^2 the difference between the two could reach about 15 %.

We have the same for the charged current case, where there is no available data to compare with, but again, we can define a kinematic region with large Q^2 and make the calculation of these cross sections. Our results are shown in figure 6.37, where we can see the cross section as a function of Q^2 for values of up to 40000 GeV^2. We also show the scale variation and the K-factor for this case. We can see from both results, W and Z boson contributions, how at very large Q^2, the cross sections in figures 6.36 and 6.37 approach each other.

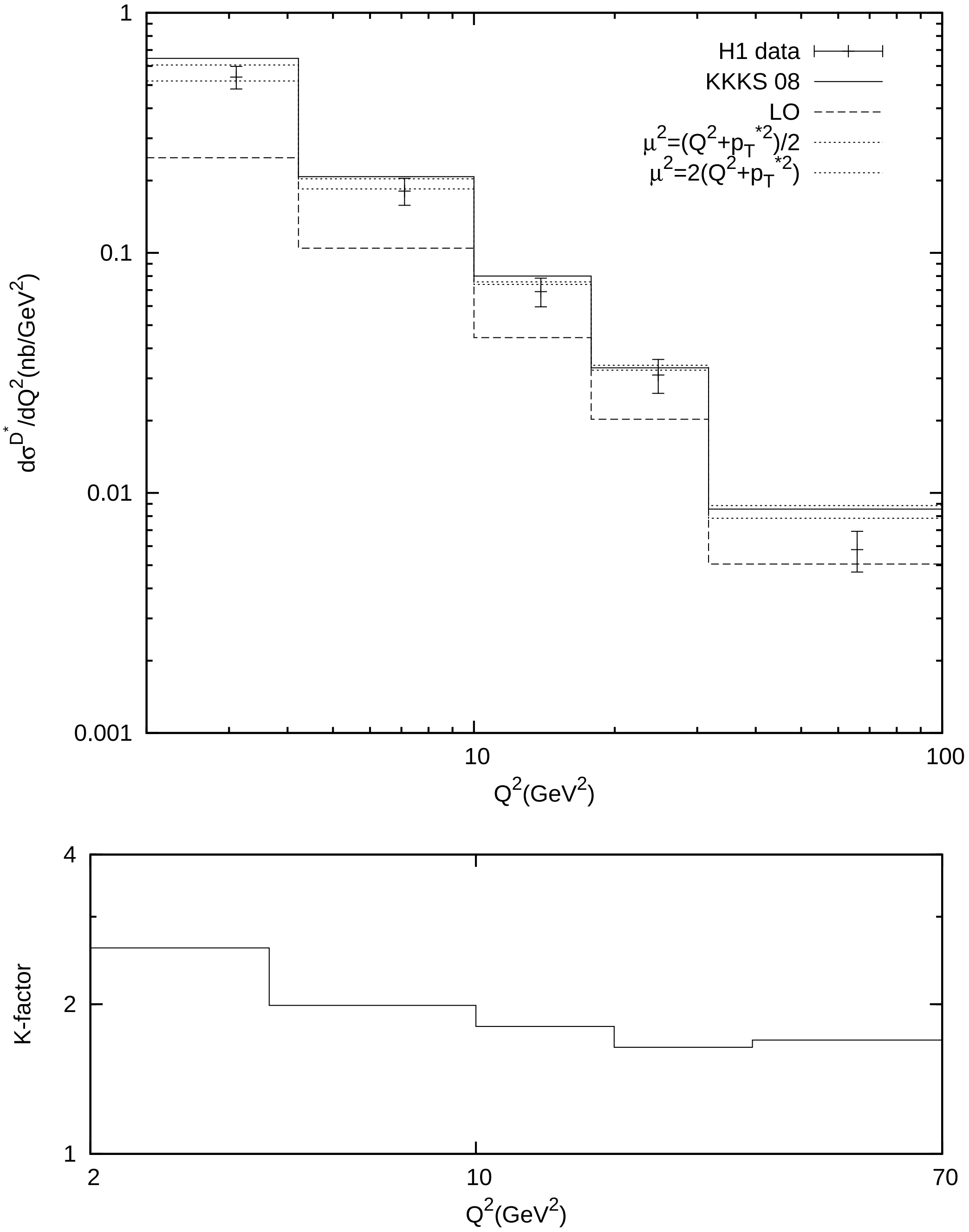

Figure 6.20: $\frac{d\sigma^{D^{*\pm}}}{dQ^2}$ with the KKKS08 set of FFs compared to the experimental data from H1 [71].

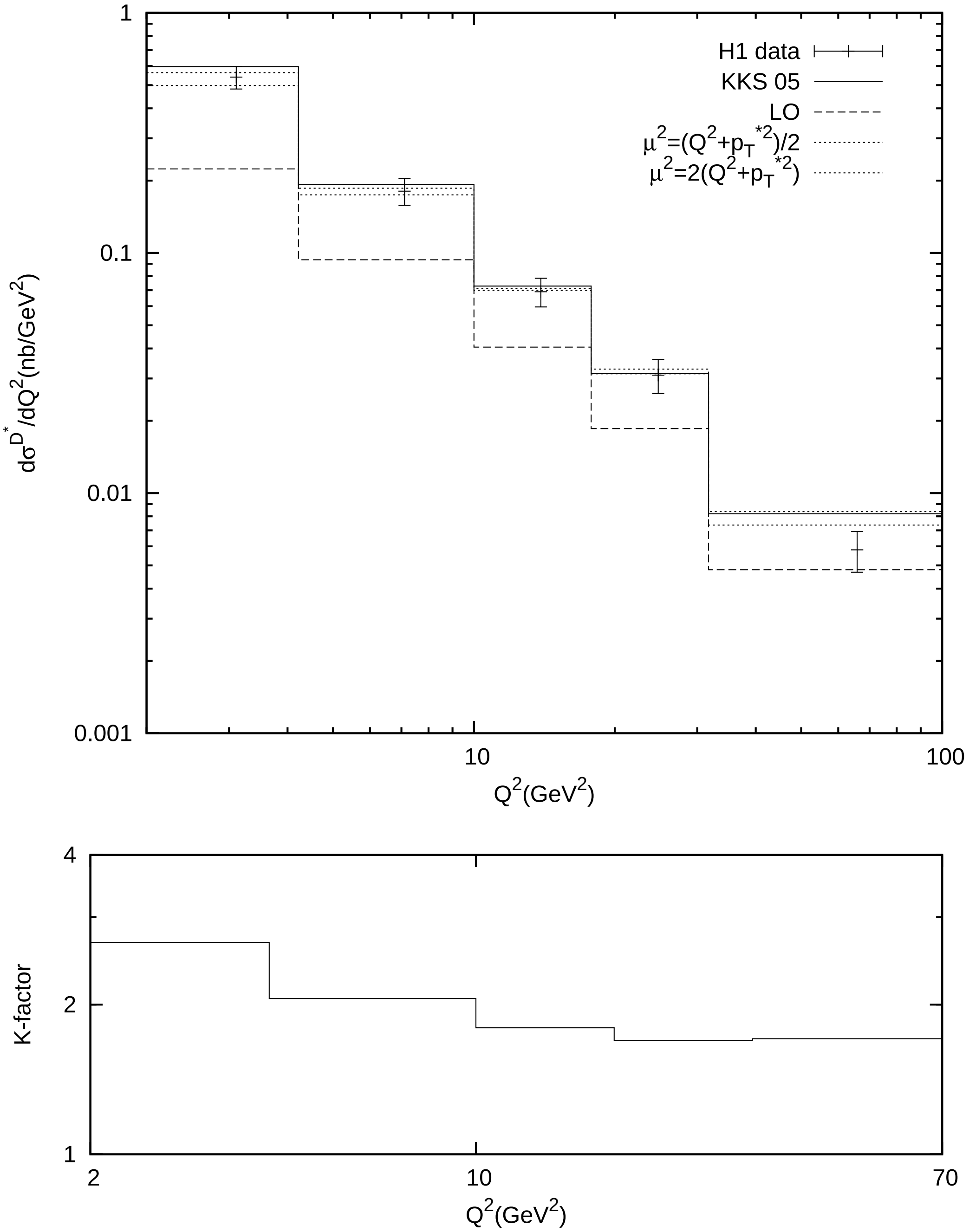

Figure 6.21: $\frac{d\sigma^{D^{*\pm}}}{dQ^2}$ with the KKS05 set of FFs compared to the experimental data from H1 [71].

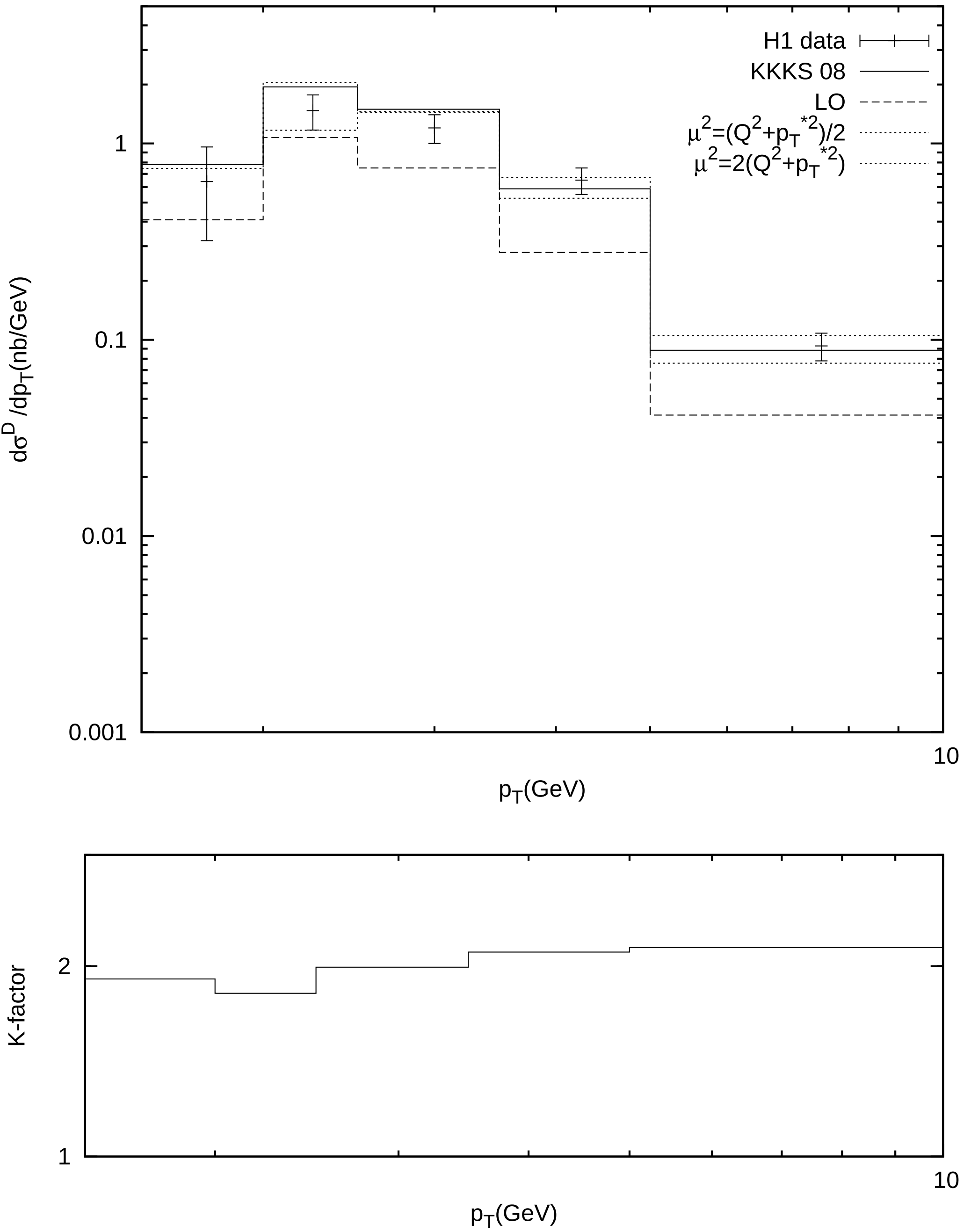

Figure 6.22: $\frac{d\sigma^{D^{*\pm}}}{dp_T}$ with the KKKS08 set of FFs compared to the experimental data from H1 [71].

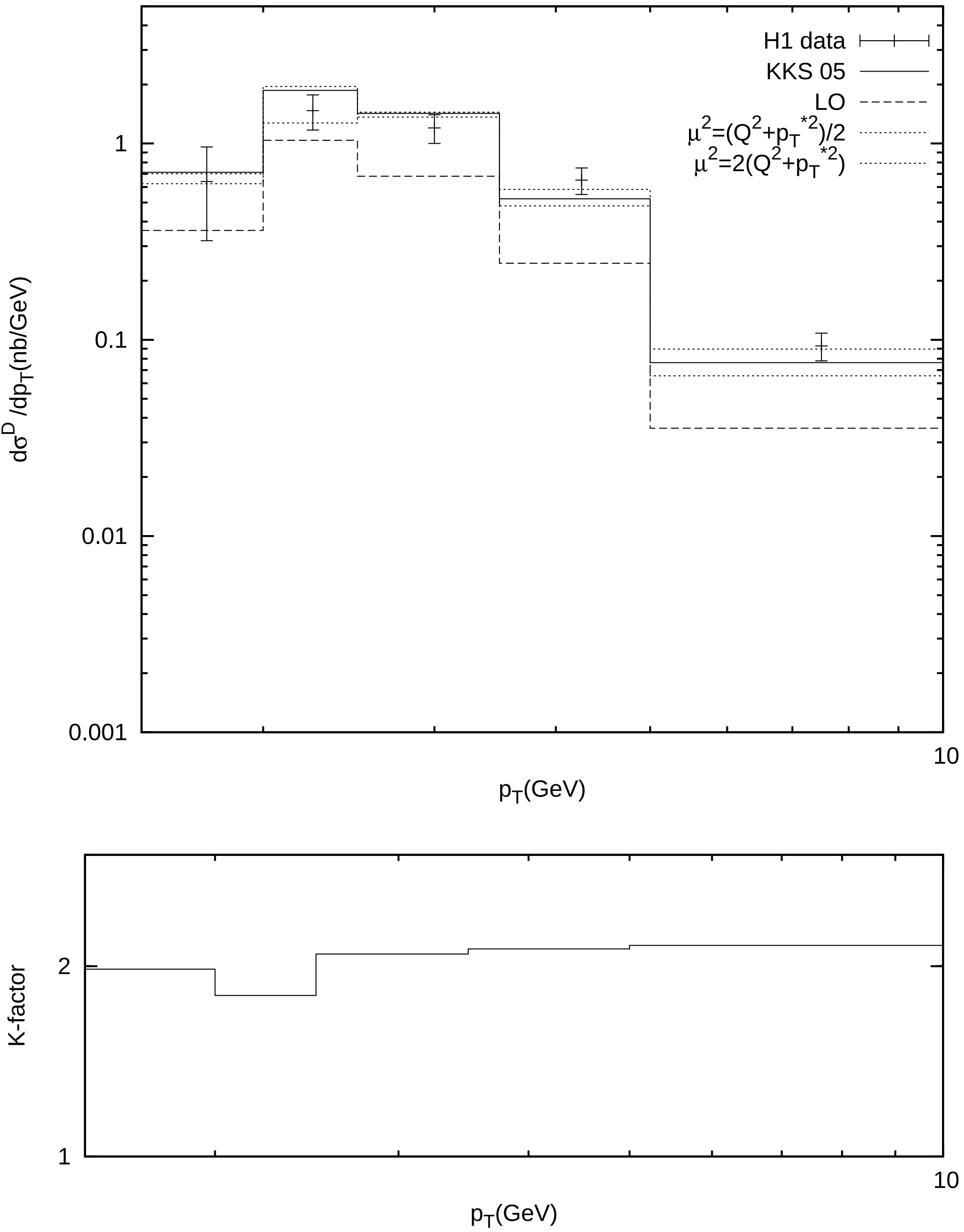

Figure 6.23: $\frac{d\sigma^{D^{*\pm}}}{dp_T}$ with the KKS05 set of FFs compared to the experimental data from H1 [71].

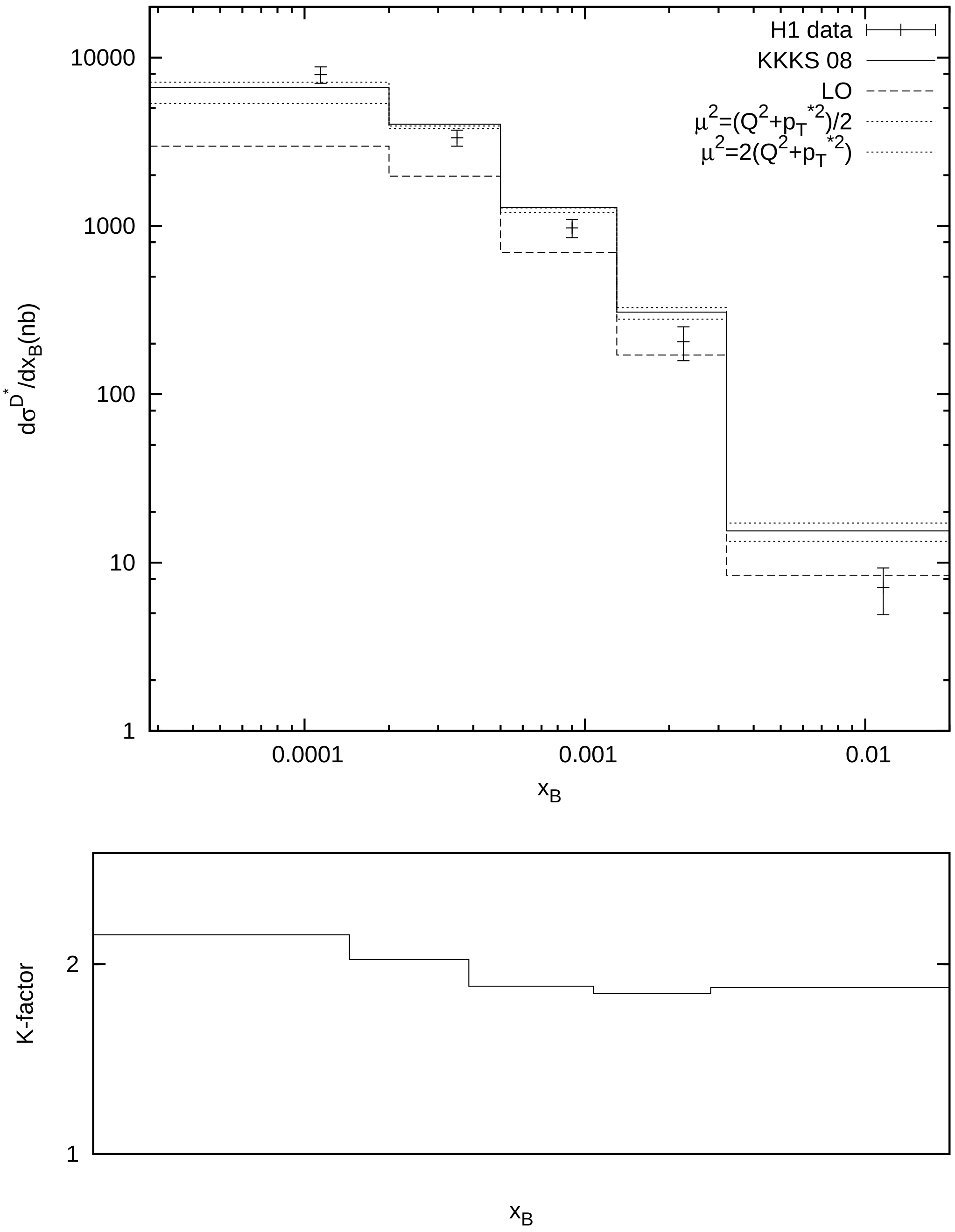

Figure 6.24: $\frac{d\sigma^{D^{*\pm}}}{dx_B}$ with the KKKS08 set of FFs compared to the experimental data from H1 [71].

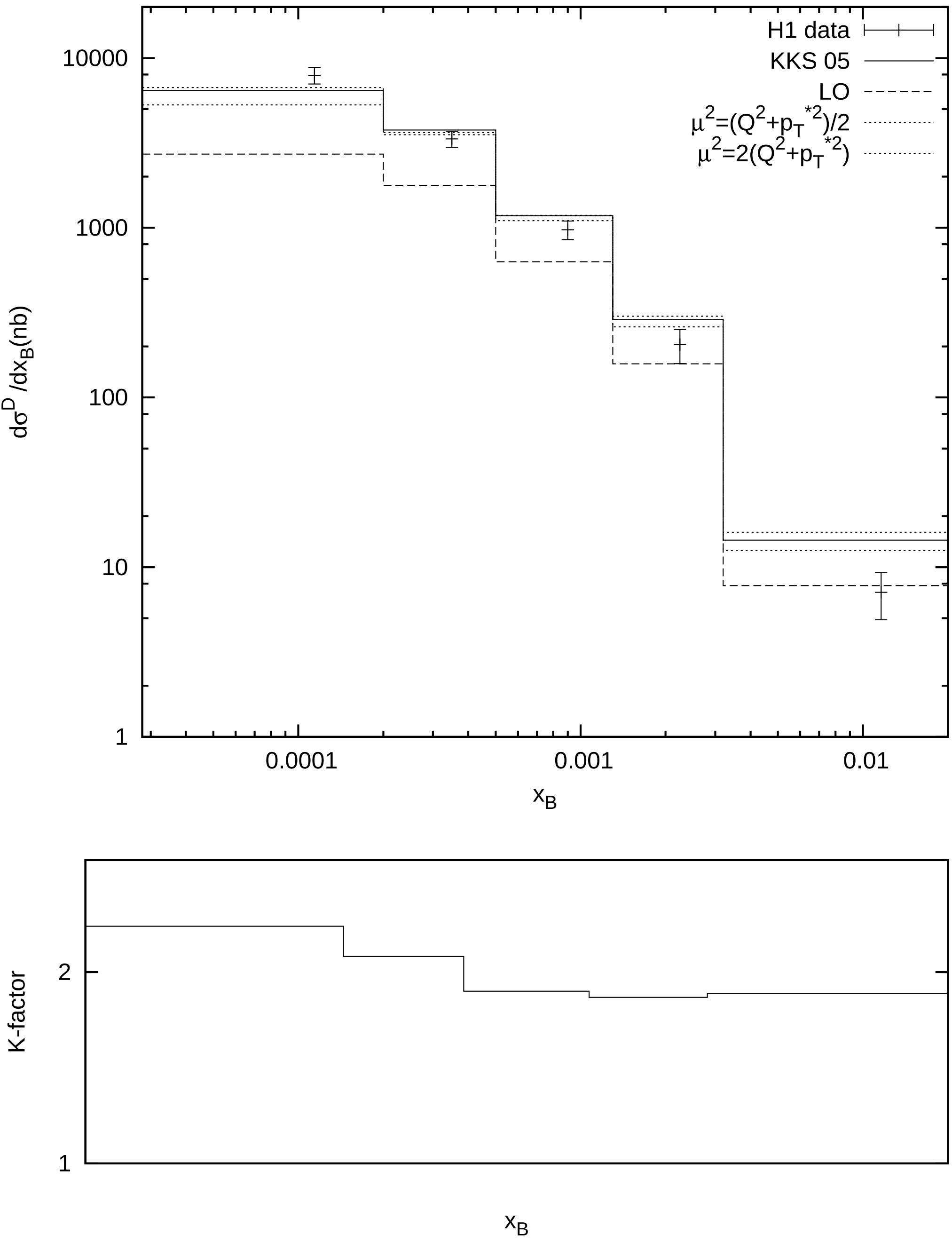

Figure 6.25: $\frac{d\sigma^{D^{*\pm}}}{dx_B}$ with the KKS05 set of FFs compared to the experimental data from H1 [71].

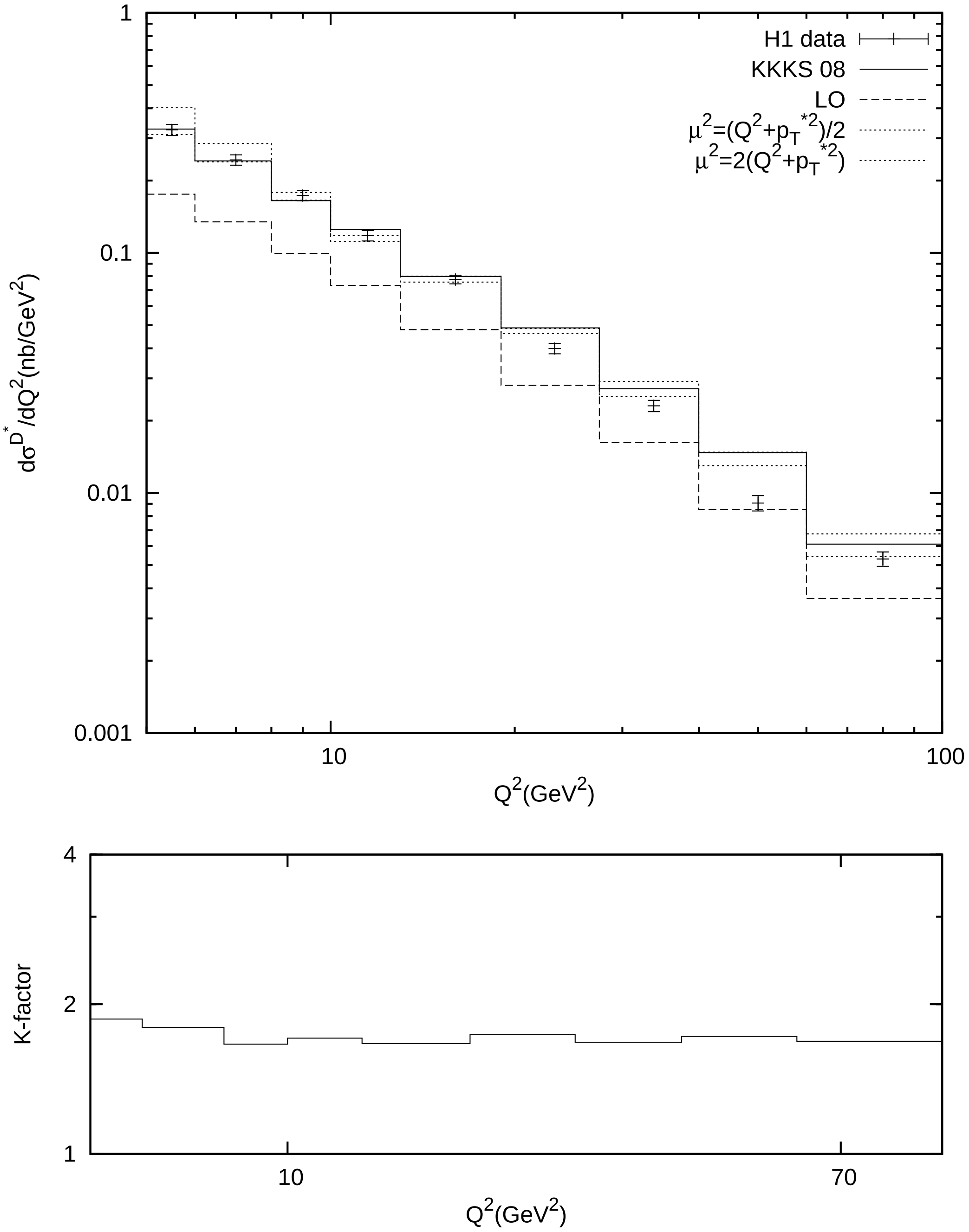

Figure 6.26: $\frac{d\sigma^{D^{*\pm}}}{dQ^2}$ with the KKKS08 set of FFs compared to the experimental data from H1 [72].

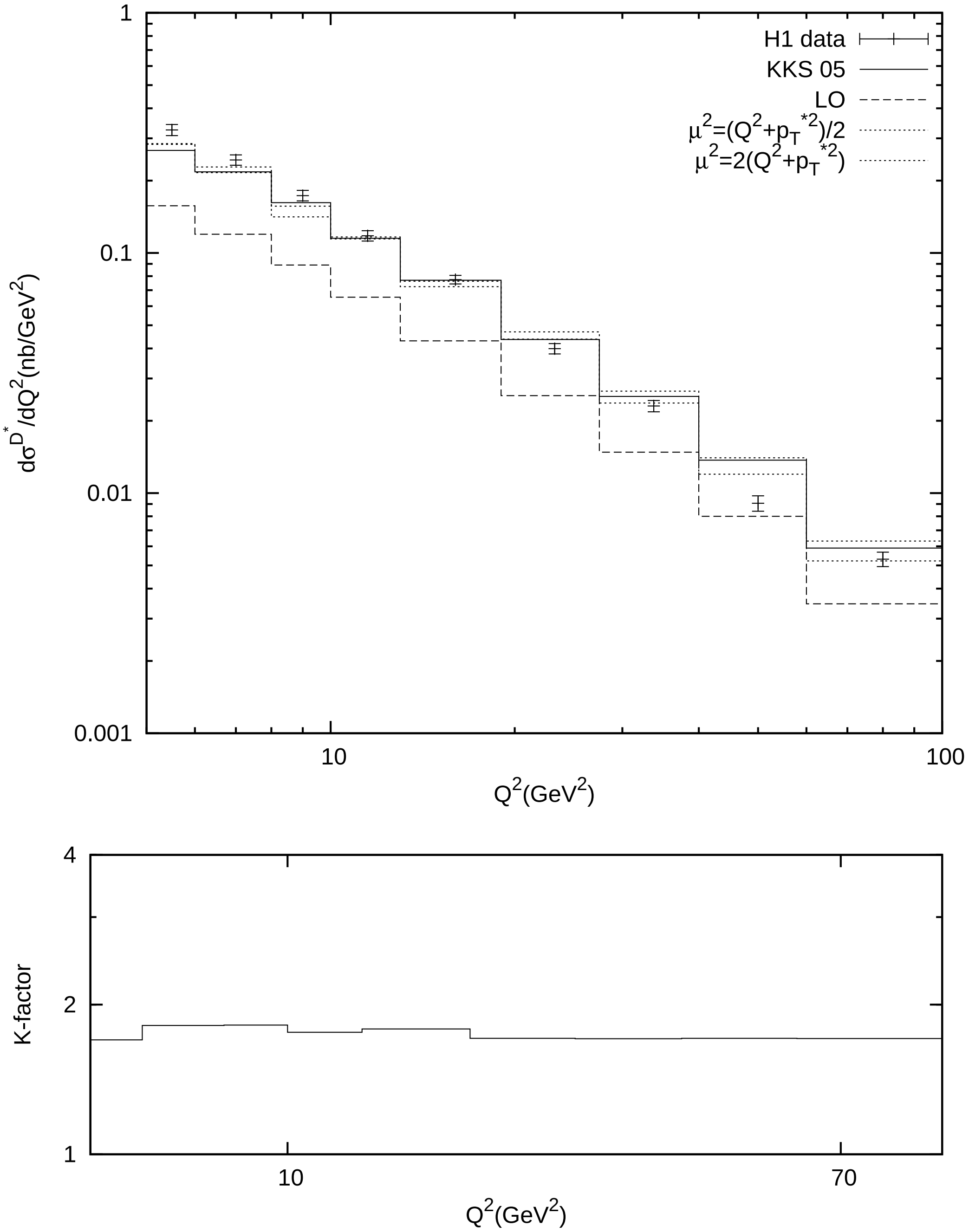

Figure 6.27: $\frac{d\sigma^{D^{*\pm}}}{dQ^2}$ with the KKS05 set of FFs compared to the experimental data from H1 [72].

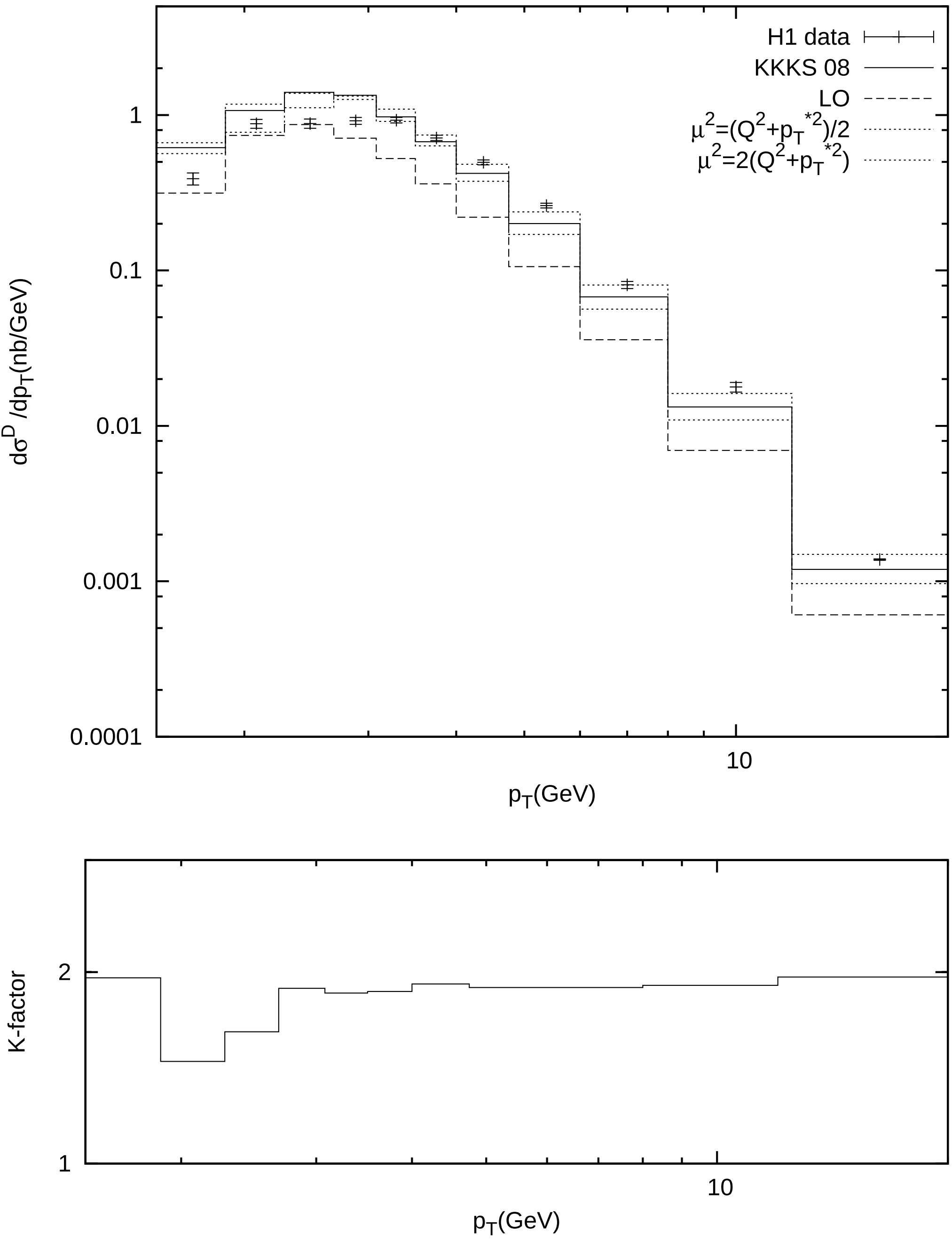

Figure 6.28: $\frac{d\sigma^{D^{*\pm}}}{dp_T}$ with the KKKS08 set of FFs compared to the experimental data from H1 [72].

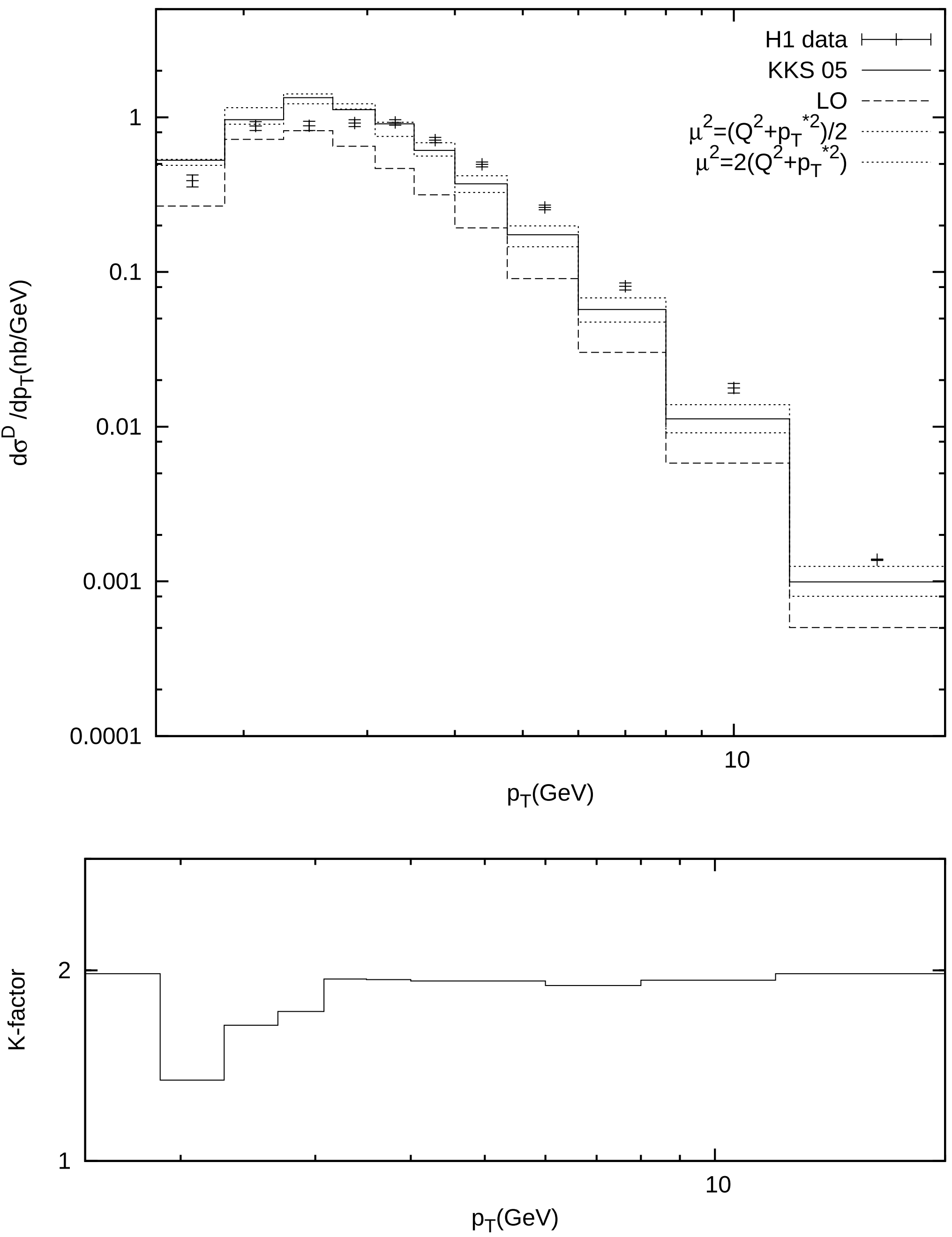

Figure 6.29: $\frac{d\sigma^{D^{*\pm}}}{dp_T}$ with the KKS05 set of FFs compared to the experimental data from H1 [72].

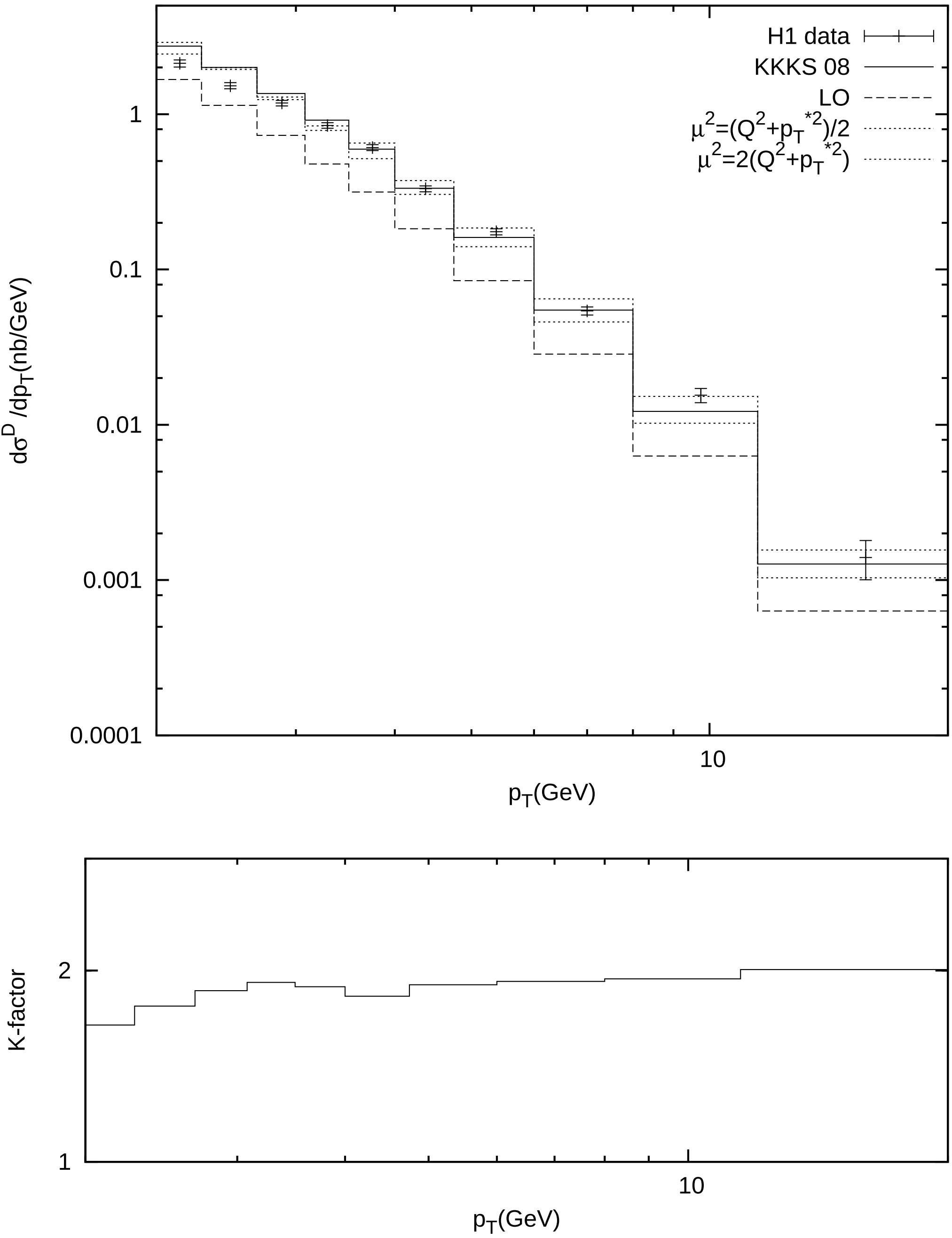

Figure 6.30: $\frac{d\sigma^{D^{*\pm}}}{dp_T^*}$ with the KKKS08 set of FFs compared to the experimental data from H1 [72].

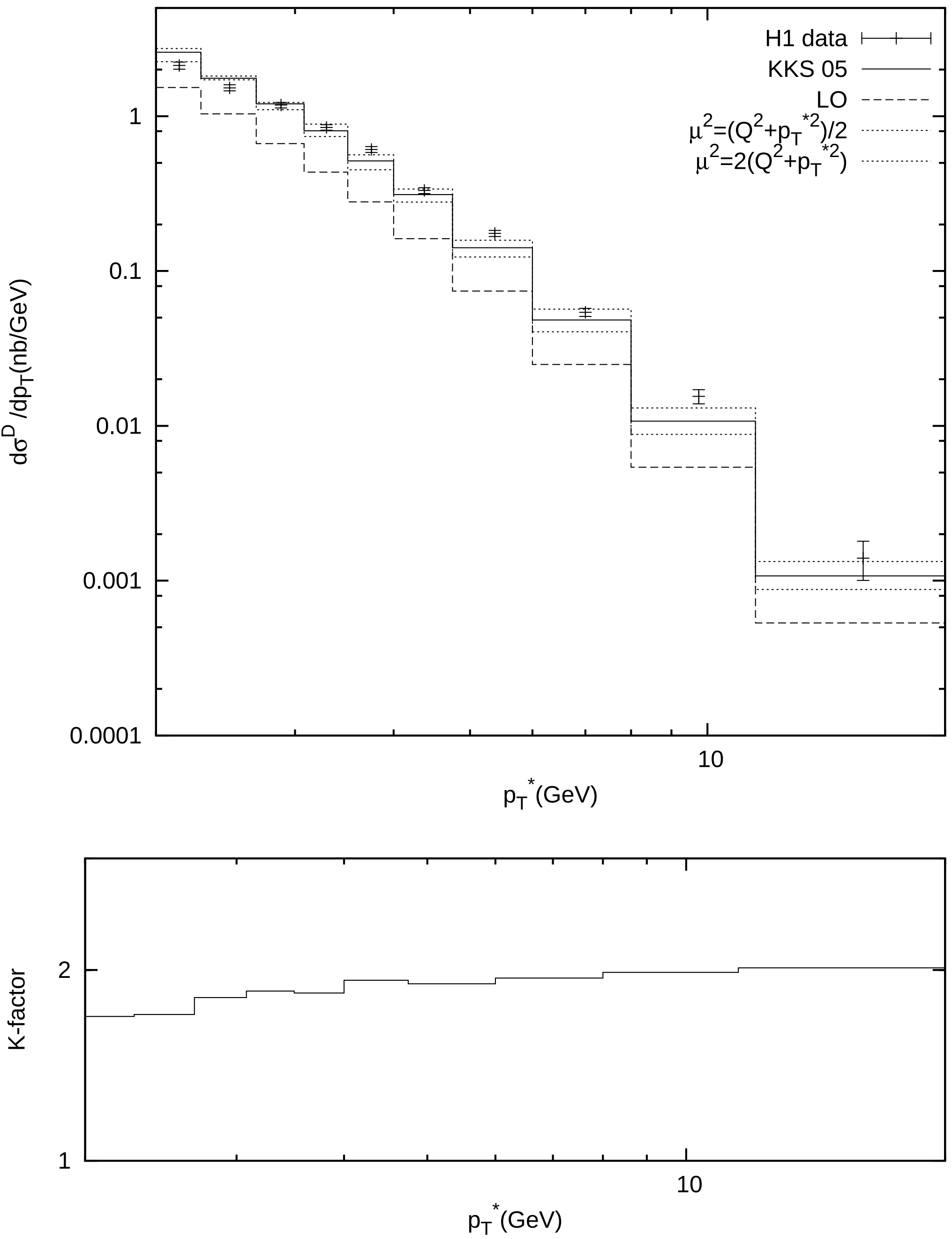

Figure 6.31: $\frac{d\sigma^{D^{*\pm}}}{dp_T^*}$ with the KKS05 set of FFs compared to the experimental data from H1 [72].

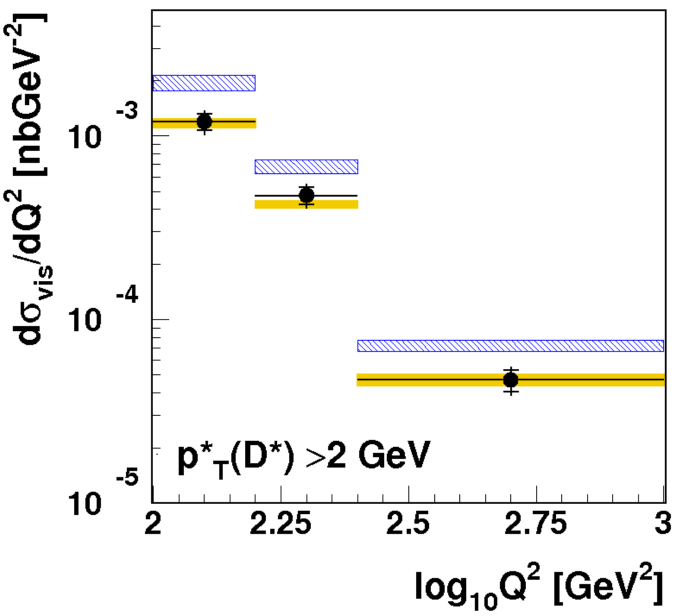

Figure 6.32: $\frac{d\sigma^{D^{*\pm}}}{dQ^2}$ with the KKKS08 set of FFs compared to the experimental data from H1 [73] for high Q^2. The dashed band represents our predictions and the solid band is the prediction obtained with the program HVQDIS. The plot was provided by the H1 collaboration.

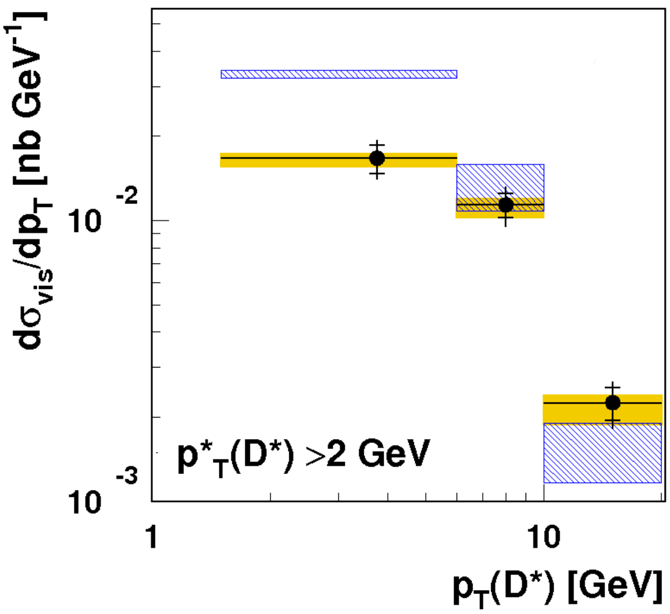

Figure 6.33: $\frac{d\sigma^{D^{*\pm}}}{dp_T}$ with the KKKS08 set of FFs compared to the experimental data from H1 [73] for high Q^2. The dashed band represents our predictions and the solid band is the prediction obtained with the program HVQDIS. The plot was provided by the H1 collaboration.

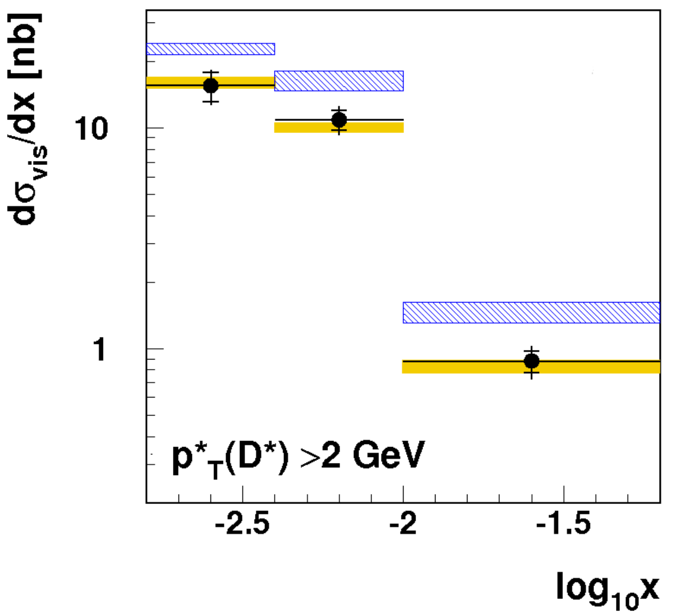

Figure 6.34: $\frac{d\sigma^{D^{*\pm}}}{dx_B}$ with the KKKS08 set of FFs compared to the experimental data from H1 [73] for high Q^2. The dashed band represents our predictions and the solid band is the prediction obtained with the program HVQDIS. The plot was provided by the H1 collaboration.

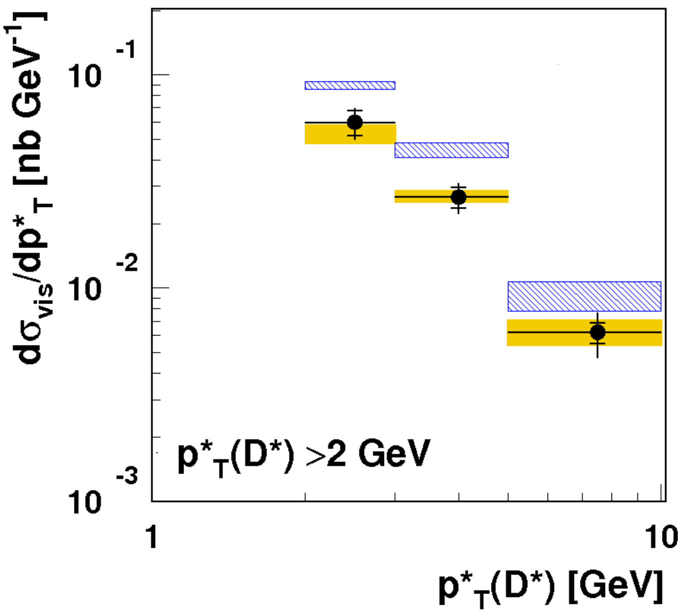

Figure 6.35: $\frac{d\sigma^{D^{*\pm}}}{dp_T^*}$ with the KKKS08 set of FFs compared to the experimental data from H1 [73] for high Q^2. The dashed band represents our predictions and the solid band is the prediction obtained with the program HVQDIS. The plot was provided by the H1 collaboration.

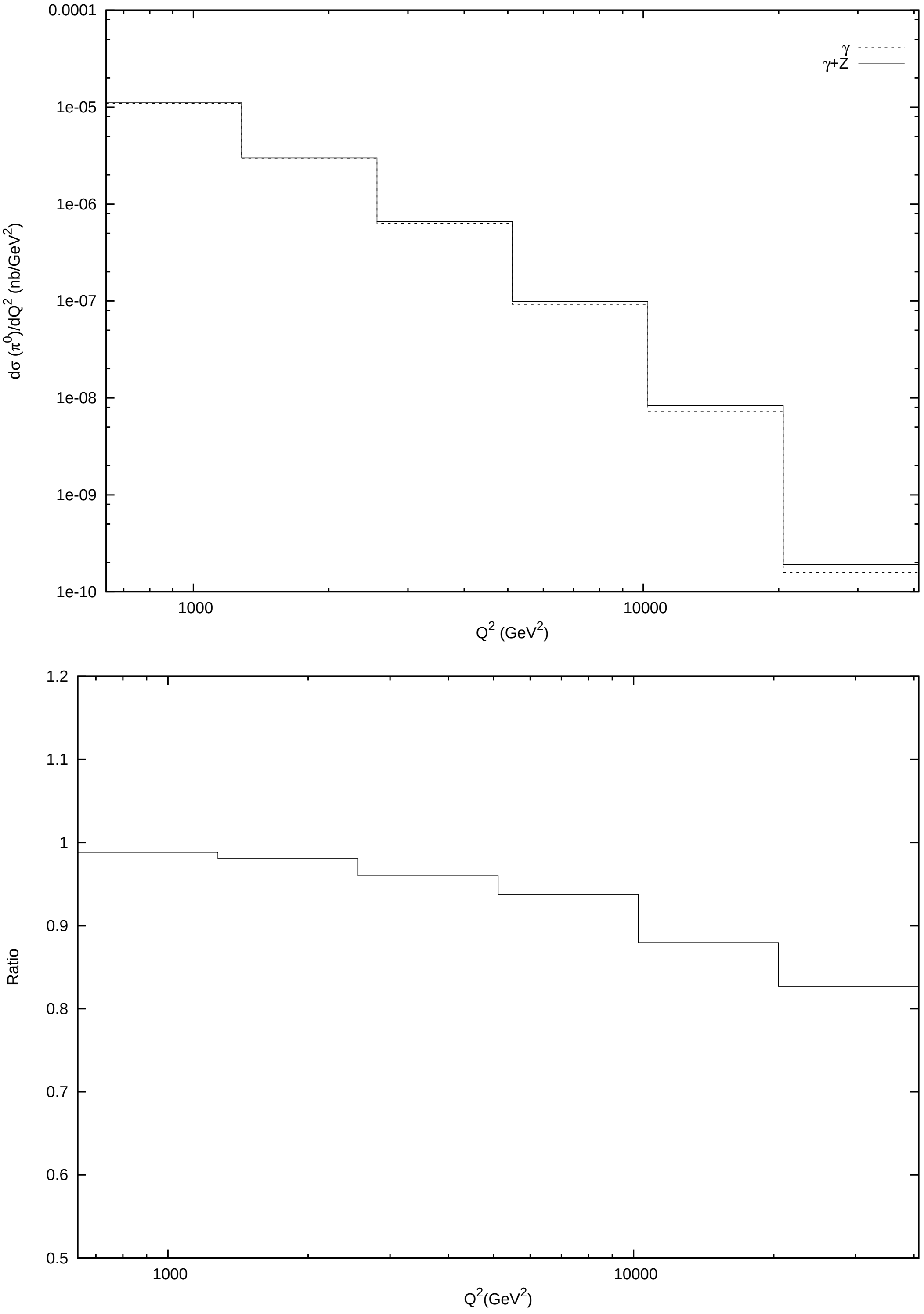

Figure 6.36: $\frac{d\sigma^{\pi^0}}{dQ^2}$ with the AKK set of FFs including the Z boson contribution, compared to the result without the Z boson.

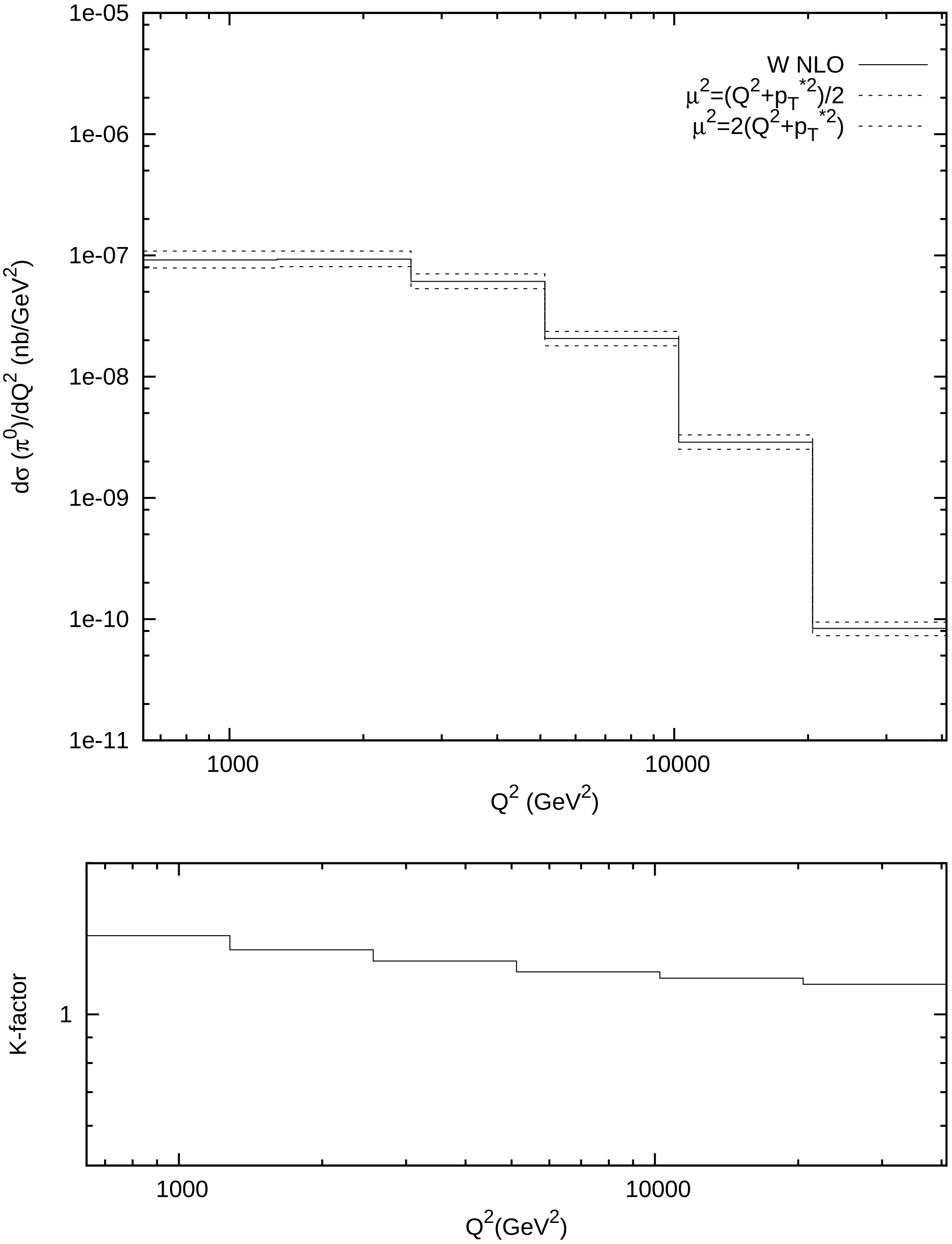

Figure 6.37: $\frac{d\sigma^{\pi^0}}{dQ^2}$ with the AKK set of FFs for the case of W exchange.

Chapter 7

Conclusions

We have calculated the inclusive single production of hadrons in neutral and charged current deep-inelastic scattering at next-to-leading order using perturbative QCD to first and second order in α_s.

To first order in α_s, virtual and real corrections were calculated and checked against the results in Refs. [44, 47–49]. A Monte Carlo program was implemented to obtain cross sections at NLO in the $\overline{\text{MS}}$ scheme and compared to charged hadron production data from the H1 and ZEUS collaborations [56, 57, 61, 64, 65]. Cross sections were normalized to the total cross section and our results were presented in distributions of Q^2 and the scaled momentum of the detected hadron x_p. We set the number of active quark flavours $n_f = 5$, and used the CTEQ6.6M PDF set of Ref. [32] and the AKK set of fragmentation functions [34] as our default to describe the initial proton and the final hadron respectively. We used the CTEQ6.6M value $\Lambda^{(5)}_{\text{QCD}} = 226$ MeV, and the factorization / renormalization scale was chosen to be $\mu = Q$.
Our predictions describe the data nicely in the scaled momentum distributions, where we have also obtained agreement using the KKP [35] and Kretzer [36] sets of fragmentation functions. The uncertainty due to the choice of FF set is largest at large x_p, since the data from e^+e^- interactions is most inaccurate and most scarce at large x_p. We have also estimated the uncertainty introduced by the choice of PDF set and scale by calculating our predictions using the MSTW set of PDFs [33] and by varying the scale by a factor of two. The error due to the choice of PDF set is rather small for all values of x_p while the uncertainty from the choice of the scale is largest at the large values of the scaled momentum. In general, increasing the scale steepens the drop in the cross section with increasing x_p.
The distributions in Q^2 agree well with the ZEUS data in Ref. [61], except for at low Q^2 they overshoot at small x_p and they undershoot at large x_p. Except at the lower Q^2 and smaller x_p

region, the AKK predictions tend to be closer to the Kretzer predictions than to the KKP ones. The uncertainty due to the choice of PDF set for the proton is negligible. At smaller x_p values, the uncertainty with respect to the arbitrary scale choice become less relevant with increasing Q^2, and are unimportant for all Q^2 at the other x_p values. However, when comparing our predictions with new data from both H1 [64] and ZEUS [65], our predictions fail to describe the data accurately, especially in the lowest and highest bins in x_p. The results for AKK and Kretzer remain quite close, while the KKP set shows the largest deviation from these two. The uncertainty in the choice of PDF is again negligible here and the uncertainty in the scale variation remains more or less constant.

We also compared to these data our predictions including the Z boson contribution, expecting to see some effect at high Q^2, however, since all the cross sections are normalized to the total cross section, where the effect is also present, it was impossible to distinguish between curves with and without the Z boson contribution. Instead, we compared our cross sections without normalization to see the effect of considering the complete neutral current cross section. The effect is found to be as large as 30% for the highest Q^2 bin and rather similar for all the bins in x_p considered. We also obtained cross sections for charged current DIS but unfortunately, there are no data available to compare with.

To second order in α_s, we have used the subtraction method described in [18] to calculate NLO cross sections in the $\overline{\text{MS}}$ scheme and compare our predictions to data available from HERA. We have calculated virtual corrections to neutral and charged current DIS processes and checked them against published results in Refs. [43, 53, 54]. We also calculated the relevant real corrections and in the case of virtual photon exchange, we were able to make an analytical comparison with the amplitudes used in Ref. [54]. In the framework of the subtraction method, we calculated the insertion operator $\mathbf{I}$ and the functions $\mathbf{P}, \mathbf{K}, \mathbf{H}$ for our particular case and implemented a Monte Carlo program to obtain the NLO cross sections.

We compared our predictions with H1 data for π^0 [66, 67] and $D^{*\pm}$ production [71–73] , always with the requirement of a lower cut in p_T^*, essential in our calculation. As in the case of first order in α_s, we have chosen CTEQ6.6M and AKK as our default sets of PDFs and FFs respectively, and $n_f = 5$, $\Lambda_{\text{QCD}}^{(5)} = 226$ MeV, and the factorization / renormalization scale was chosen here as $\mu^2 = [Q^2 + (p_T^*)^2]/2$. In addition, in the case of $D^{*\pm}$ production, we have used the KKKS08 set of fragmentation functions [69], to describe the final state meson.

In the case of pion production, our NLO predictions agree with the data within errors, while they significantly overshoot our default LO predictions. Indeed, the K factors always exceed unity and even reach one order of magnitude at low values of p_T^*, Q^2, or x_B. The theoretical uncertainties in our NLO predictions due to scale variation are quite large, especially at low values of p_T^*, Q^2, or x_B, where the K factors themselves are large, which is partly related to the opening of new partonic production channels at NLO, which are absent at LO. The uncertainty in the choice of PDF set was always negligible and predictions using the KKP set of FFs returned lower values but always within the experimental errors. We were also able to compare with the calculation of Ref. [68], where we found agreement for the main channel $g \rightarrow g$, but we found disagreement in the $q \rightarrow q$ and $q \rightarrow g$ channels, that seem to have a problem in the code used in Ref. [68] since they yield negative cross sections for large values of p_T^*.

Our predictions seem to describe the data well for low Q^2 in $D^{*\pm}$ production, where we also studied the effect of different sets of PDFs and FFs that, as before, do not contribute to the theoretical uncertainty. We also showed the effect of a scale variation, to have an idea of the theoretical error in our predictions. At high Q^2, the predictions seem to describe the shapes of the data distributions but not their values. Our predictions seem to overshoot the data in most cases. Finally, we presented our cross sections for neutral current (including the Z boson contribution) and charged current DIS in the hypothetical case of pion production. However, there are no data available at the appropriate ranges in Q^2 to be able to see any effect due to these contributions.

Bibliography

[1] Glashow, S. L., Nucl. Phys. **22**, 579 (1961).

[2] Weinberg, Steven, Phys. Rev. Lett. **19**, 1264 (1967).

[3] Gross, D. J. and Wilczek, Frank, Phys. Rev. Lett. **30**, 1343 (1973).

[4] Politzer, H. David, Phys. Rev. Lett. **30**, 1346 (1973).

[5] Brock, Raymond et al. [CTEQ Collaboration], Rev. Mod. Phys. **67**, 157 (1995).

[6] Feynman, Richard P., Phys. Rev. Lett. **23**, 1415 (1969).

[7] Bjorken, J. D. and Paschos, Emmanuel A., Phys. Rev. **185**, 1975 (1969).

[8] T. Muta, *Foundations of Perturbative QuantumChromodynamics.* Worl Scientific, 1987.

[9] A.H. Mueller, *Perturbative QuantumChromodynamics.* Worl Scientific, 1989.

[10] Yang, Chen-Ning and Mills, Robert L., Phys. Rev. **96**, 191 (1954).

[11] Fritzsch, H. and Gell-Mann, Murray and Leutwyler, H., Phys. Lett. **B47**, 365 (1973).

[12] Gross, D. J. and Wilczek, Frank, Phys. Rev. **D8**, 3633 (1973).

[13] Feynman, R. P., Acta Phys. Polon. **24**, 697 (1963).

[14] DeWitt, Bryce S., Phys. Rev. **162**, 1195 (1967).

[15] Faddeev, L. D. and Popov, V. N., Phys. Lett. **B25**, 29 (1967).

[16] 't Hooft, Gerard and Veltman, M. J. G., Nucl. Phys. **B50**, 318 (1972).

[17] Lewis H. Ryder, Cambridge University Press 1985, 1996.

[18] S. Catani, M. H. Seymour, Nucl.Phys.B. **485**, 291 (1997).

[19] Amsler, C. et al. [Particle Data Group], Phys. Lett. **B667**, 1 (2008).

[20] Klein, M. and Riemann, T., Z. Phys. **C24**, 151 (1984).

[21] Bjorken, J. D., Phys. Rev. **179**, 1547 (1969).

[22] G. Miller et al., Phys. Rev. **D 5**, 528 (1972).

[23] Eichten, T. et al., Phys. Lett. **B46**, 274 (1973).

[24] Brandelik, R. et al. [TASSO Collaboration], Phys. Lett. **B86**, 243 (1979).

[25] M. Derrick et al. [ZEUS Collaboration], Phys. Lett. **B 316**, 412 (1993).

[26] I. Abt et al. [H1 Collaboration], Nucl. Phys. **B 407**, 515 (1993).

[27] V.N. Gribov and L.N. Lipatov, Sov. J. Nucl. Phys. **15**, 438 (1972).

[28] L.N. Lipatov, Sov. J. Nucl. Phys. **20**, 94 (1975).

[29] Y.L. Dokshitzer, Sov. Phys. JETP **46**, 641 (1977).

[30] G. Altarelli and G. Parisi, Nucl. Phys. **B 126**, 298 (1977).

[31] Collins, John C. and Soper, Davison E. and Sterman, George, Adv. Ser. Direct. High Energy Phys. **5**, 1 (1988).

[32] Nadolsky, Pavel M. et al. [CTEQ Collaboration], Phys. Rev. **D78**, 013004 (2008).

[33] Martin, A. D. and Stirling, W. J. and Thorne, R. S. and Watt, G. (2009).

[34] Albino, S. and Kniehl, B. A. and Kramer, G., Nucl. Phys. **B803**, 42 (2008).

[35] Kniehl, Bernd A. and Kramer, G. and Potter, B., Nucl. Phys. **B582**, 514 (2000).

[36] Kretzer, S., Phys. Rev. **D62**, 054001 (2000).

[37] G. Ingelman, A. De Roeck, R. Klanner, *Future Physics at HERA*. Workshop proceedings, 1995-1996.

[38] Kniehl, Bernd A. and Zwirner, Lennart, Nucl. Phys. **B621**, 337 (2002).

[39] Breitenlohner, P. and Maison, D., Commun. Math. Phys. **52**, 11 (1977).

[40] Siegel, Warren, Phys. Lett. **B84**, 193 (1979).

[41] Chanowitz, Michael S. and Furman, M. A. and Hinchliffe, I., Phys. Lett. **B78**, 285 (1978).

[42] ’t Hooft, Gerard and Veltman, M. J. G., Nucl. Phys. **B44**, 189 (1972).

[43] Korner, J. G. and Schuler, G. and Kramer, G. and Lampe, B., Phys. Lett. **B164**, 136 (1985).

[44] Korner, J. G. and Schuler, G. and Kramer, G. and Lampe, B., Z. Phys. **C32**, 181 (1986).

[45] Larin, S. A. Given at International Seminar on Quarks (Quarks 92), Zvenigorod, Russia, 11-17 May 1992.

[46] Larin, S. A. and Vermaseren, J. A. M., Phys. Lett. **B259**, 345 (1991).

[47] Altarelli, Guido and Ellis, R. Keith and Martinelli, G., Nucl. Phys. **B157**, 461 (1979).

[48] Furmanski, W. and Petronzio, R., Zeit. Phys. **C11**, 293 (1982).

[49] Altarelli, Guido and Ellis, R. Keith and Martinelli, G. and Pi, So-Young, Nucl. Phys. **B160**, 301 (1979).

[50] Denner, Ansgar, Fortschr. Phys. **41**, 307 (1993).

[51] Passarino, G. and Veltman, M. J. G., Nucl. Phys. **B160**, 151 (1979).

[52] Lampe, B. and Kramer, G., Phys. Scripta **28**, 585 (1983).

[53] Graudenz, Dirk, Phys. Rev. **D49**, 3291 (1994).

[54] Kniehl, B. A. and Kramer, G. and Maniatis, M., Nucl. Phys. **B711**, 345 (2005).

[55] Vermaseren, J. A. M. (2000).

[56] Adloff, C. et al. [H1 Collaboration], Nucl. Phys. **B504**, 3 (1997).

[57] Derrick, M. et al. [ZEUS Collaboration], Z. Phys. **C70**, 1 (1996).

[58] Nadolsky, Pavel M. and Stump, D. R. and Yuan, C. P., Phys. Rev. **D64**, 114011 (2001).

[59] Graudenz, Dirk, Phys. Lett. **B406**, 178 (1997).

[60] Binnewies, J. and Kniehl, Bernd A. and Kramer, G., Z. Phys. **C65**, 471 (1995).

[61] Breitweg, J. et al. [ZEUS Collaboration], Phys. Lett. **B414**, 428 (1997).

[62] Nadolsky, Pavel M. and Kidonakis, Nikolaos and Olness, F. I. and Yuan, C. P., Phys. Rev. **D67**, 074015 (2003).

[63] Cacciari, Matteo and Nason, Paolo and Oleari, Carlo, JHEP **10**, 034 (2005).

[64] Aaron, F. D. et al. [H1 Collaboration], Phys. Lett. **B654**, 148 (2007).

[65] ZEUS Collaboration. To be published (2009).

[66] Adloff, C. et al. [H1 Collaboration], Phys. Lett. **B462**, 440 (1999).

[67] Aktas, A. et al. [H1 Collaboration], Eur. Phys. J. **C36**, 441 (2004).

[68] Daleo, A. and de Florian, D. and Sassot, R., Phys. Rev. **D71**, 034013 (2005).

[69] Kneesch, T. and Kniehl, B. A. and Kramer, G. and Schienbein, I., Nucl. Phys. **B799**, 34 (2008).

[70] Kniehl, B. A. and Kramer, G. and Schienbein, I. and Spiesberger, H., Phys. Rev. **D71**, 014018 (2005).

[71] Aktas, A. et al. [H1 Collaboration], Eur. Phys. J. **C51**, 271 (2007).

[72] Jung, Andreas Werner. DESY-THESIS-2009-001.

[73] Brinkmann, Martin. PhD Thesis (in preparation).

Acknowledgements

I would like to thank Prof. Bernd Kniehl for his supervision and advice. I am very grateful to Prof. Gustav Kramer for all his help and guidance during my PhD, his input was always of great assistance in moving things forward and crucial in finishing this thesis. I would also like to thank Dr. Simon Albino, with whom I had many fruitful discussions and who always helped me clarify doubts.

I want to thank my family and friends for always supporting me during this time, and my friends in Hamburg for making my stay there a lot of fun.